INVESTIGATING THE PERFORMANCE AND DEGRADATION OF LOW PLATINUM LOADED PROTON EXCHANGE MEMBRANE FUEL CELLS

by
ASAL SAEIDFAR

Submitted to the Graduate School of Engineering and Natural Sciences in partial fulfillment of the requirements for the degree of
Doctor of Philosophy

Sabanci University
December 2023

ABSTRACT

INVESTIGATING THE PERFORMANCE AND DEGRADATION OF LOW PLATINUM LOADED PROTON EXCHANGE FUEL CELLS

ASAL SAEIDFAR

Ph.D. Thesis, December 2023

Thesis Advisor: Prof. Dr. Serhat Yeşilyurt

Keywords: Proton Exchange Membrane Fuel Cell, Low Platinum Loaded Catalyst, Morphology of Catalyst Layer, Accelerated Stress Tests, Electrode Degradation, Carbon Corrosion.

Reduction of Platinum (Pt) loading in proton exchange membrane fuel cells (PEMFCs) without sacrificing performance and durability is essential for the commercial viability of these devices. Comprehending the impact of the catalyst layer (CL) design variables including Pt-loading, Pt/C weight ratio, ionomer loading, and dilution as well as the interaction of these variables, provides insights for increasing the performance and durability of low Pt-loaded PEMFCs. In this thesis, the impact of CL characteristics and operating conditions on the cell performance, oxygen transport resistances, ionic potential loss, and cathodic overpotential is first evaluated using a detailed pseudo-three-dimensional (P3D) model. The model employs a multiphase non-isothermal P3D approach coupled with a detailed electrochemical kinetic sub-model concerning the CL microstructural features as well as the mixed wettability pore size distribution mathematical sub-model accounting for microstructural characteristics of different porous layers. By further developing the P3D model into a transient one, the impact of the CL characteristics on the voltage under and overshoot is discussed. Based on the modeling results, systematic experiments are developed and executed to isolate the specific effects of CL thickness, Pt-loading, Pt/C ratio, and carbon support material. A range of comprehensive in-situ electrochemical characterization methods is employed to gain insights into the beginning-of-life (BOL) performance of the samples. Moreover, the durability of PEMFCs of different CL features is evaluated under two accelerated stress tests (ASTs) simulating the Pt-dissolution and carbon corrosion degradation mechanisms.

ÖZET

DÜŞÜK PLATİN YÜKLÜ PROTON DEĞİŞİM YAKIT HÜCRELERİNİN PERFORMANSININ VE BOZULMASININ İNCELENMESİ

ASAL SAEIDFAR

Doktora Tezi, Aralık 2023

Tez Danışmanı: Prof. Dr. Serhat Yeşilyurt

Anahtar Kelimeler: Proton değişim membranlı yakıt pili, Düşük Platin Katalizör, Katalizör Katmanının Morfolojisi, Hızlandırılmış Stres Testleri, Elektrot Bozulması, karbon korozyonu.

Performans ve dayanıklılıktan ödün vermeden proton değişim membranlı yakıt hücrelerindeki (PEMFC'ler) Platin (Pt) yükünün azaltılması, bu cihazların ticari olarak uygulanabilirliği için esastır. Pt yüklemesi, Pt/C ağırlık oranı, iyonomer yüklemesi ve seyreltme dahil olmak üzere katalizör katmanı (CL) tasarım değişkenlerinin etkisinin yanı sıra bu değişkenlerin etkileşiminin anlaşılması, düşük Pt yüklü katalizörlerin performansını ve dayanıklılığını artırmaya yönelik bilgiler sağlar. PEMFC'ler. CL özelliklerinin ve çalışma koşullarının hücre performansı, oksijen taşıma dirençleri, iyonik potansiyel kaybı ve katodik aşırı potansiyel üzerindeki etkisi ilk olarak ayrıntılı bir sözde üç boyutlu (P3D) model kullanılarak değerlendirilir. Model, farklı gözenekli katmanların mikroyapısal özelliklerini hesaba katan karışık ıslanabilirlik gözenek boyutu dağılımı matematiksel alt modelinin yanı sıra, CL mikroyapısal özelliklerine ilişkin ayrıntılı bir elektrokimyasal kinetik alt modelle birleştirilmiş çok fazlı izotermal olmayan bir P3D yaklaşımını kullanır. P3D modelinin geçici bir modele dönüştürülmesiyle, CL özelliklerinin düşük ve aşırı gerilim üzerindeki etkisi tartışılmıştır. Modelleme sonuçlarına dayanarak ayrıca CL kalınlığı, Pt yüklemesi, Pt/C oranı ve karbon destek malzemesinin spesifik etkilerini izole etmek için sistematik deneyler geliştirilmekte ve yürütülmektedir. Numunelerin yaşam başlangıcı (BOL) performansı hakkında bilgi edinmek için bir dizi kapsamlı yerinde elektrokimyasal karakterizasyon yöntemi kullanılır. Ayrıca, farklı CL özelliklerine sahip PEMFC'lerin dayanıklılığı, Pt çözünmesi ve karbon korozyonu bozunma mekanizmalarını simüle eden iki farklı hızlandırılmış stres testi (AST) altında değerlendirilir.

To Women, Life, Freedom ...

ACKNOWLEDGEMENT

I would like to express my sincere gratitude to my Ph.D. advisor, Prof. Serhat Yeşilyurt, for his continuous support throughout this journey. His guidance, mentorship, patience, and encouragement have been invaluable to me at every step.

I wish to extend my appreciation to the esteemed members of the dissertation committee, Prof. Selmiye Alkan Gürsel, Prof. Tuğçe Yüksel, Prof. Uğur Ünal, and Prof. Sibel Özenler for their participation in my Ph.D. dissertation committee.

I would like to further extend my gratitude to Prof. Selmiye Alkan Gürsel for providing me with the laboratory and equipment for MEA fabrication. Special thanks to Ahmet Can Kırlıoğlu for his contributions to the physical characterization (SEM) of the experimental section, and to Navid Haghmoradi for synthesizing the hybrid support materials.

My sincere appreciation also goes to lab specialists Bilge Esenkal, Ilker Sevgen, and Bülent Köroğlu for their technical assistance.

I want to express my heartfelt thanks to my husband, Ali, for his unwavering love and support. None of this would have been possible without you.

TABLE OF CONTENTS

LIST OF FIGURES

LIST OF TABLES

NOMENCLATURE

Abbreviations

BOL	Beginning of life
CCL	Cathode catalyst layer
CH	Channel
CL	Catalyst layer
DOF	Number of degrees of freedom
$ECSA$	Electrochemical active area
EOL	End of life
Eq	Equation
FT	Flow through
GDL	Gas diffusion layer
HOR	Hydrogen oxidation reaction
IP	In plane
MEA	Membrane electrode assembly
MPL	Microporous layer
ORR	Oxygen reduction reaction
$P3D$	Pseudo-three-dimensional

$PEMFC$	Proton exchange membrane fuel cell
Pt	Platinum
RH	Relative humidity
Sim	Simulation
St	Stoichiometric ratio
TP	Through-plane
wt	Weight percentage

Subscripts and Superscripts

ads	Adsorption
an	Anode
C	Carbon
c	Capillary
ca	Cathode
CH	Channel
des	Desorption
eff	Effective
eq	Equilibrium
g	Gas
in	In-plane
l	Liquid
MEM	Membrane
Naf	Nafion
ref	Reference

rev	Reversible
th	Through-plane

Greek Letters

α	Charge transfer coefficient
δ	Thickness
η	Activation overpotential
λ	Membrane water content
μ	Dynamic viscosity
ϕ	Potential
ρ	Density
σ	Electrical conductivity
θ	Contact angle
θ_{PtO}	Pt-oxide coverage
ε	Porosity-Volume fraction

Symbols

a	Water activity
C	Concentration (mol m^{-3})
C_{P}	Specific heat capacity (J mol^{-1} K^{-1})
D	Diffusion coefficient (m^2 s^{-1})
F	Faraday's constant (96485 C mol^{-1})
h	Height (m)
i	Volumetric reaction rate (A m^{-3})
j	Current density (A m^{-2})

k	Thermal conductivity (W m^{-1} K^{-1})
L	Length (m)
n_{d}	Electro-osmotic drag coefficient
p	Pressure (Pa)
R	Oxygen transports resistances (s m^{-1})

Chapter 1

INTRODUCTION

1.1 Background and Motivation

Proton exchange membrane fuel cell (PEMFC) is an energy conversion device with several outstanding merits including high efficiency and power density, rapid operation, low operating temperature, and zero emissions [1]. These superior features offer an advantageous device for portable, stationary, and transportation applications [2]. Yet, large-scale commercialization of PEMFCs is hindered by critical issues related to the high cost of production and durability, despite significant improvements that have been achieved through theoretical and experimental efforts [3]. Of particular interest is the thorough understanding of the effects of the CL micro-structure on the cell performance and durability under various design and operating conditions as well as engineering of the pore structure, wettability, and ionomer network.

Reduction of platinum (Pt)-loading in the catalyst layer (CL) can significantly reduce the cost of the cell; however, it severely sacrifices cell performance while making it more vulnerable to degradation. As a result, vast R&D efforts have focused on the reduction of Pt-loading and the development of alternative electrocatalysts matching high oxygen reduction reaction (ORR) activity and increasing Pt utilization through novel material design [4]. Many researchers reported increased oxygen transport resistances with the reduction of Pt-loading which leads to significant performance losses [5][4]. Multiple hypotheses are proposed for the increased resistances including the decrement of the electrochemically active surface area [6] as well as higher oxygen flux near the ionomer thin

film and reaction active sites [7]. Moreover, various ionomer properties including surface wettability, water uptake, swelling, and mechanical properties vary significantly from the bulk properties as the film thickness approaches 20 nm due to the phase separation [8].

Another significant challenge hindering the widespread adoption of PEMFCs is the requirement to ensure durability under the operating and ambient conditions encountered by automotive vehicles. Automotive PEMFCs must withstand a range of conditions, including frequent start-ups and shut-downs, dynamic load cycles, extended periods of idling, and exposure to extreme weather conditions. Under rapid load changes, for example, appropriate fuel-supplying strategies are required to overcome the rapid performance decrease caused by fuel starvation [9]. In addition, the massive flooding and voltage perturbation resulting from load cycling is more severe in low Pt-loaded thinner CLs due to the higher rates of heat generation [10]. Moreover, the critical aspect of PEMFC durability concerns the degradation of the cathode CL, which plays a significant role in shortening the lifespan of these devices. Therefore, further investigation is necessary to unravel the impact of cathode CL compositions on the underlying degradation mechanisms occurring within the CL.

The CL of PEM fuel cells is a multi-component media and its microstructural parameters dramatically affect the cell performance and durability. The CL design characteristics include the specifications controlled during the CL synthesis such as carbon-supported electrocatalyst nanoparticles enhancing the electronic conductivity, ionomer content used for creating a proton conducting pathway, porosity for the transport of reactants, and most importantly Pt used as the catalyst of the electrochemical reaction. Moreover, the dilution ratio in CLs is used to modify the CL thickness for the same Pt-loaded samples and affects the Pt utilization [5]. Understanding the interplay between these CL characteristics and the deliberate selection of these features is required to optimize the performance and durability of low Pt-loaded PEM fuel cells.

The primary goal of this thesis is to provide a thorough understanding of the effects of CL compositions, and the interplay within CL properties in low Pt-loaded PEMFCs. The CL characteristics studied in this research include Pt-loading, weight percentage of Pt/C particles, ionomer content, mass fraction of bare carbon particles, and carbon support material. The approach of this research focuses on improving both performance and durability while simultaneously reducing overall system costs and is underpinned by the recog-

nition that innovative system design solutions can play a pivotal role in addressing the challenges faced by automotive PEM fuel cells. To this end, a pseudo-three-dimensional (P3D) non-isothermal model is coupled with a detailed electrochemical kinetic model as well as a mixed wettability pore size distribution (PSD) model for evaluating the water transport and local saturation. The interplay within CL compositions on the cell steady-state and transient performance is investigated. Further examination is achieved by experimentally evaluating the impact of catalyst structure on the performance and durability of low Pt-loaded PEM Fuel cells.

1.2 Literature Review

To enable a comprehensive examination of the aforementioned issues and the suggested framework, the following section provides a detailed description of the components of a PEM fuel cell and the operational principles of PEM fuel cells. This continues with a brief assessment of the key aspects of fuel cell development and the significance of modeling in enhancing the comprehension of underlying phenomena and facilitating advancements in performance and durability. This is followed by a review of the relevant literature on the modeling and durability of low Pt-loaded PEM fuel cells.

1.2.1 PEM Fuel Cell Principles

Proton Exchange Membrane Fuel Cells (PEMFCs), also referred to as Polymer Electrolyte Membrane Fuel Cells, are advanced electrochemical devices designed for energy conversion. As demonstrated in Figure 1.1, a single cell is composed of several essential components including a polymer electrolyte membrane (PEM), anode and cathode catalyst layers (CLs), diffusion media (DM), and two bipolar plates to securely encase the cell. The DM itself consists of a gas diffusion layer (GDL) and an optional thin microporous layer (MPL) attached to the top surface of the GDL for enhanced water management. In addition, the bipolar plates are equipped with machined channels for the effective transportation of reactants. The collective assembly of PEM, CLs, and DM is

commonly referred to as the membrane electrode assembly (MEA). In state-of-the-art fuel cells, the CLs are usually applied to the PEM using various coating processes, resulting in catalyst-coated membranes (CCMs).

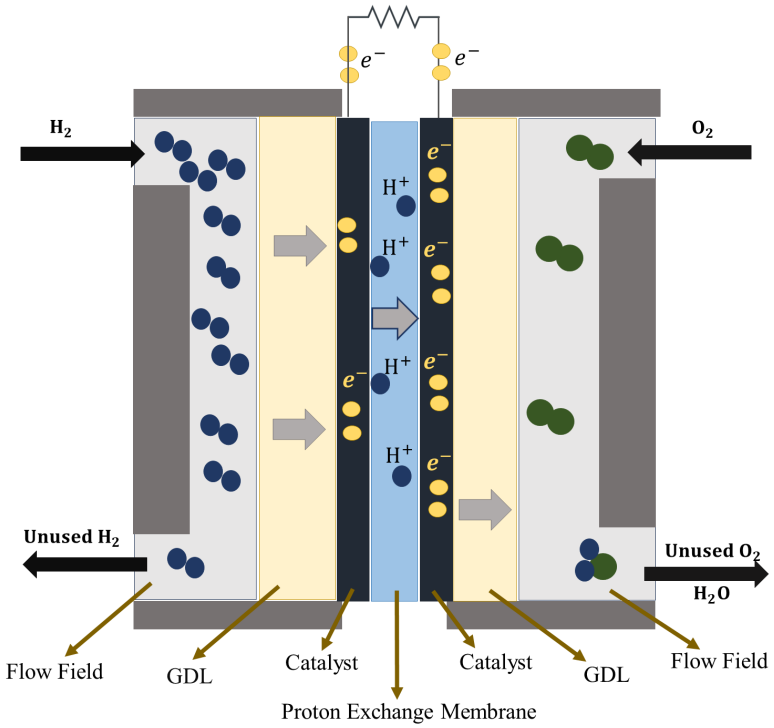

Figure 1.1: PEM Fuel cell working principle

In a PEM fuel cell, electricity is generated by the reaction of hydrogen with oxygen, typically drawn from the ambient air, which produces water and heat. In the anode compartment, hydrogen participates in a hydrogen oxidation reaction (HOR), releasing protons and electrons. The protons are conducted through the PEM to reach the cathode compartment, while the electrons are transported through an external circuit. The recombination occurs during the oxygen reduction reaction (ORR) to produce water and heat. The reactions happening within the cell are as follows,

$$HOR : 2H_2 \rightarrow 4H^+ + 4e^-$$
$$ORR : O_2 + 4H^+ + 4e^- \rightarrow 2H_2O$$

The various components of PEMFCs are meticulously designed to enable the aforementioned electrochemical reactions, with the primary goal of producing electrical power at the highest achievable efficiency. The various layers of the cell and their specific func-

tions will be elucidated in greater detail in section 1.2.3.

1.2.2 Electrochemical Thermodynamics

1.2.2.1 Theoretical Background

The theoretical potential associated for H_2/O_2 reaction is obtained as,

$$E^0 = -\frac{\Delta G^0}{nF} \tag{1.1}$$

where E^0 is the reversible potential (V), n is the number of electrons, F is the Faraday constant (C/mol), and ΔG_0 is the Gibbs free energy defined as the maximum work done on the system (J), which is dependent on the operating temperature. Assuming no entropy change and thus no heat transfer, the Gibbs free energy is equal to enthalpy change. The theoretical potential obtained at 25°C for H_2/O_2 reaction is calculated as 1.23 V. For a specific operating condition ΔG is evaluated from,

$$\Delta G = \Delta G_0 + R\,T \ln \frac{(p_{H_2})^2\ (p_{O_2})}{(p_{H_2O})^2} \tag{1.2}$$

where R is the ideal gas constant, T is the operating temperature, and p_X is the partial pressure of either reactants or product X. Considering equation 1.1, the electrode potential for a specific operating condition is,

$$E = E_0 - \frac{R\,T}{nF} \ln \frac{(p_{H_2})^2\ (p_{O_2})}{(p_{H_2O})^2} \tag{1.3}$$

1.2.2.2 Electrode Performance

Due to different voltage losses including the kinetic, ohmic, and mass transport limitations within the PEM fuel cell operation, the cell voltage deviates from its theoretical potential causing irreversible voltage losses. This causes the cell performance evaluated with the potential-current density (I-V) relationship to deviate from the ideal case

as demonstrated in Figure 1.2.

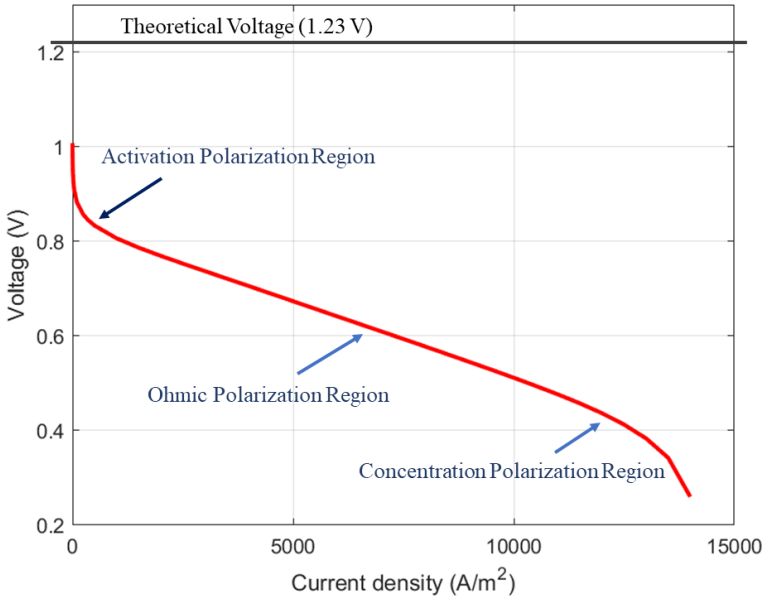

Figure 1.2: Polarization curve for a PEM fuel cell

Based on the operating conditions, the starting point of the polarization curve deviates from the theoretical potential calculated at room temperature. In addition, different factors such as fuel crossover, and internal losses caused by the electronic conduction contribute to this deviation. The activation polarization region relates to the voltage loss associated with overcoming the energy barrier in the electrodes, especially the cathode with sluggish kinetics. The ohmic polarization region is associated with the voltage loss of the ohmic limitation including the ionic and electronic resistances as well as the contact resistances. The ohmic resistance is usually obtained from the EIS data by collecting the high-frequency intercept in the Nyquist plot [11].

The mass transport polarization is attributed to mass transport limitations arising from the concentration gradient between the supply of the reactants and the reaction rate. The electrochemical reaction is constrained by the transport mechanism of reactants in both the GDLs and PEM in this region. The transport mechanism encompasses convection, diffusion, and migration of hydrogen, oxygen, protons, and water, moving into and out of the catalyst active sites.

1.2.3 PEM Fuel Cell Components

1.2.3.1 Polymer Electrolyte Membrane

At the core of the fuel cell, the Polymer Electrolyte Membrane (PEM) plays a pivotal role by facilitating the selective transport of protons, while hindering the transport of electrons and keeping the reactants separated. Moreover, the PEM is characterized by an operating temperature below 100°C, which renders PEMFCs well-suited for applications in the automotive and portable power sectors.

The level of hydration in the PEM is a critical factor influencing its proton conductivity. While a well-hydrated PEM exhibits high proton conductivity and low ohmic resistance, a dry one results in significant ohmic loss due to reduced proton conductivity. The PEM requires adequate hydration to minimize ohmic resistance, however, excessive water causes flooding in the DM and increases mass transport losses. The water transport within the PEM significantly affects its hydration state, which is characterized by four major mechanisms. The electro-osmotic-drag mechanism in which water molecules are carried with ions passing through the PEM, diffusion resulting from the concentration gradient, the permeation resulting from the hydraulic pressure difference, and lastly thermo-osmosis initiated from temperature gradient across the PEM to provide more thermodynamically stable state [7].

Another crucial aspect of PEM lies in its selective transport properties, which are paramount for designing durable fuel cells. The formation of pinholes, for example, creates a shortcut for gas transport causing exothermic reaction [12]. In addition, different operational modes, such as hydration, dehydration, and temperature cycling, cause repeated compressive and tensile stress cycles, initiating cracks and pinholes or propagating the existing ones through the PEM thickness. Consequently, the PEM degradation occurring in its various forms including chemical [13][14], mechanical [15][14], and thermal [16] prohibits the participation of reactants in the reaction and causes catastrophic performance losses. Examples of the commercial PEMs include Nafion® and Gore.

1.2.3.2 Diffusion Media

The porous diffusion media (DM) consists of a gas diffusion layer (GDL) and, in most cases, a microporous layer (MPL). The DM provides electronic connectivity to the backing plates and mechanical support for the PEM and CLs. The primary role of DM is creating pathways for the transport of reactant gases from the channels to the active sites in CLs as well as removing the product water. Inadequate water removal results in liquid water accumulation in pores, blocking gas transport pathways which leads to performance losses. For better water removal, the diffusion layers are partially coated with a hydrophobic material, typically PTFE. The choice of materials, including binders and hydrophobic coatings, as well as microstructure, significantly affects the effectiveness of the DM, and mathematical modeling provides insights into the transport properties of DM.

The DM consists of two layers including a GDL with pore sizes on the order of 1-100 μm, composed of either woven carbon cloth or carbon paper, and an MPL with smaller pore sizes in the range of 10-1000 nm. Although the use of an MPL has shown performance improvements, the exact reasons are still debated and could be attributed to improved layer contact, enhanced water removal due to reduced cathode flooding, and thermal conductivity [17]. Moreover, the heat transfer properties of the DM significantly modify the water transport phenomena and promote the phase-change-induced flow resulting from the temperature gradient within the thickness of the DM. The lower thermal conductivity of the DM causes elevated temperatures near the CL resulting in higher evaporation rates. The vapor travels across the DM due to the vapor gradient and discards in the channels [6].

The DM suffers from mechanical, electrochemical, and thermal degradation under PEM fuel cell operating conditions. The DM degradation causes performance losses mainly due to modifications in thermal and transport properties, as well as structural changes, all of which affect the transport of reactants in CLs [18]. However, the degradation of DM plays a secondary role in PEM durability despite membrane and CL degradation.

1.2.3.3 Bipolar Plates and Gas Flow Channels

Bipolar plates play a vital role in PEMFC operation, facilitating reactant transport through the channels, current conduction, heat and water management, and cell separation. These plates are usually made of highly conductive materials providing sufficient mechanical strength to withstand clamping pressures ranging up to 5 MPa. In addition, chemical stability and durability against corrosion are other necessary features of the bipolar plate material. The choice of the material for bipolar plates presents significant challenges due to their contribution to a substantial portion of the weight, volume, and cost of PEM fuel cells [19].

The flow field design in bipolar plates including size, shape, and patterns of channels has a strong effect on the cell performance. Moreover, the extra diffusion length for the species transport through the GDL under the ribs needs to be considered. A specific flow field design includes many geometric considerations including the ratio of channels to ribs, the cross-sectional shape, and the channel aspect ratio [20][21]. The improper design of flow fields results in a poor distribution of reactants [20][22], the high-pressure drop across the active area [21], and decreased water removal capacity, all of which directly reduce the performance. In addition, various flow channel patterns have been proposed and explored primarily to optimize gas transport, including parallel, serpentine, and interdigitated flow channels. Each of the flow field designs provides advantages and disadvantages. While parallel flow fields inhibit water accumulation in bends, the serpentine channels express even reactant distribution within the active area and sufficient pressure drop for the removal of water droplets compared to parallel and interdigitated channels [23]. Therefore, the serpentine channels are utilized for the experimental part of this research.

1.2.3.4 Catalyst Layers

The CLs provide the active reaction sites, creating triple-phase boundaries (TPBs) to enable electrons, protons, and reactant gases to engage in the reaction. The Pt content of CL defines the catalytic activity, number of active sites, and the oxygen transport resis-

tances [5]. Various requirements must be considered for the CL including the existence of highly-dispersed Pt sites with high catalytic activity, continuous passage for the efficient proton transport and electron conduction, and through-connected pore network to facilitate gas transport and water removal. These circumstances create a heterogeneous and complex structure that needs to be optimized in terms of mass transport and reaction rate while considering the economical and technical requirements.

Conventional CLs are composed of a homogeneous suspension of high surface area carbon to support Pt nanoparticles, perfluorosulfonic acid (PFSA) ionomer as a binder, and a solvent, all of which affect the morphology of the CL which in turn determines the Pt utilization, cell performance, and its durability. High surface area carbon is used to increase the mass activity minimizing poisoning of active sites, caused by the sulfonic acid groups of ionomer, by limiting the direct contact between metal and ionomer [24]. In addition, carbon support characteristics govern the pore size distribution and ionomer dispersion within the CL [25] while solvent properties define the ink rheology and its dispersion [26]. The ionomer acts as the proton conductor expanding the electrochemically active region into the bulk material, providing mechanical stability, and moisturizing the cell to avoid membrane dehydration [27]. Moreover, the Pt loading and Pt-to-carbon (Pt/C) ratio determines the thickness of the CL and catalytic activity [5].

The CL performance relies on the effective transport of electrons, ions, and reactant gases in reaching the reaction sites. This is mainly determined by the interplay between proton and gas transport resistances. In the anode CL, the minimal protonic transport resistances result from the high diffusivity of hydrogen and high HOR kinetics. However, the slow ORR kinetics and production of water, which exists in both liquid and vapor phases simultaneously depending on the thermodynamic state, cause increased mass transport losses in the cathode CL. Under dry conditions, the ionomer provides low proton conductivity and increased proton transport resistance, while the mass transport resistance is suppressed due to the low water content. The excessive ionomer drying results in decreased oxygen permeability and causes mass transport limitations. Under wet operating conditions, however, the ionomer exhibits high conductivity and minimal protonic resistances, while the water accumulation blocks the reactant pathways. From another perspective, an inadequate amount of ionomer content, serving as a medium for proton conduction, impedes the effective distribution of protons across the entire CL, while the

addition of ionomer to the CL extends the electrochemically active sites. Moreover, the ionomer serves as a binding material, enhancing mechanical stability, and its hydrophilic properties help maintain the membrane's hydration. However, excessive ionomer loading can lead to a reduction in the available pore volume for gas transport, which is exacerbated under water flooding of CL hydrophilic pores [27]. Therefore, a proper understanding of these trade-offs helps to achieve the highest catalyst utilization and optimal performance, and consideration of these microstructural characteristic impacts is a necessity.

Extensive research has been directed towards reducing Pt loading and creating alternative electrocatalysts with superior ORR activity, to enhance Pt utilization by employing innovative material designs [24]. Such research studies are motivated by the high cost and limited availability of Pt. At low Pt-loadings, researchers detailed the increase of the transport resistance within the CL, which is attributed to the reduction of active sites, as well as the heightened flux of reactants near each active site [4]. As a result of such endeavors, the Pt-loading of the anode electrode is reduced to 0.1-0.05 mg/cm^2, while Pt-loading of the cathode electrode with sluggish kinetics is decreased to 0.2 mg/cm^2. The need for further reduction of Pt-loading necessitates understanding, numerical modeling, and experimental developments to clarify the underlying causes and enhance the performance of low Pt-loaded PEM fuel cells, which is the subject of the current work.

Apart from the dominant effects of the CL on cell performance, its degradation is of great importance in determining cell durability, which primarily manifests as a loss of the electrochemically active surface area (ECSA). Catalyst degradation includes two major mechanisms Pt-dissolution and carbon corrosion. The former concerns the migration of Pt nanoparticles either to precipitate onto larger Pt nanoparticles, or to create Pt band within the membrane, and is usually caused by high potential loadings. The carbon support materials including Ketjen Black and Vulcan XC-72 are widely used in the CL due to the high electrical and thermal conductivity [28] and are susceptible to corrosion. Thus, the corrosion of the carbon black under high voltage conditions results in oxidation of the carbon black support in the cathode, detachment of Pt particles, and eventually performance degradation. This performance degradation manifests itself through several mechanisms including the ECSA loss, reduced electrical connectivity of the catalyst support structure, and morphological alterations [28], causing both kinetic losses in ORR and oxygen mass transport losses. Systematic investigations are necessary for revealing

the effect of CL characteristics on enhancing the cell durability, which helps to further decrease the Pt-loading in the cathode without sacrificing the cell durability. Moreover, comprehending the underlying mechanisms responsible for the performance degradation over time provides insights for addressing these issues.

1.2.4 Literature Survey on Modeling of PEM Fuel Cells

Modeling the transport phenomena within the fuel cell and its consequent performance is of significant interest. It enables the examination of variables within a cell that might otherwise be inaccessible. This information is also pivotal in comprehending the behavior of a fuel cell stack, assessing its performance, and estimating its operational lifetime. Specifically, evaluating transport resistances and optimizing the structure of CLs is achievable using mathematical modeling and numerical simulation, which helps to encompass both micro and macro-scale transport processes.

The intricate interplay between the distribution of gas species, liquid water, current density, and temperature in different layers of a PEMFC introduces significant computational complexity. The interest in modeling transport phenomena within fuel cells is initiated by the groundbreaking work of Springer et al. [29], concerning the PEM water content. This interest continues with numerous developed models to explore the intricate transport phenomena within different layers of PEM fuel cells. Many researchers focused on the membrane water content to understand the contribution of different involved mechanisms [30][31]. Moreover, modeling water management in DM has received extensive attention due to the complexity of formulating the two-phase flow and the impact of liquid water accumulation on fuel cell performance [32]. This complexity stems from liquid water generation either from the humidified gas stream or electrochemical reaction, the pressure drops [33], and flow pattern properties in DM [32]. Through these studies, DM transport properties and microstructure are detailed to significantly affect the two-phase flow, A pioneering model in this context is the bundle of capillaries model developed by Weber [34], which later is improved by including a Gaussian contact angle distribution [35].

Recently, various studies have focused on scrutinizing the pore morphology, transport

properties, and reaction kinetics in CLs [36][37][38], with the primary aim of reducing the amount of precious metal loading. In an operational PEMFC, the CL primarily serves as a gateway for the transport of charged species including protons and electrons as well as non-charged gas species including air, hydrogen, and water vapor. While the transport of charged species occurs within the solid phases, including protons in the ionomer and electrons in the Pt-Carbon interface, the transport of non-charged species and water phase changes take place within the gas pores and the ionomer phase. The electrochemical reaction happens at the CL, and the reaction kinetics are contingent on the concentration of gas species and the potential difference between the ionomer and the carbon phases [24]. Heat is generated both in electrochemical reactions and charge transfer, and water is the by-product of the cathodic ORR, which exists in multiple phases simultaneously, including gas, liquid, and absorbed water in the ionomer [24]. The detailed kinetic models help relate the spatial distribution of water, reactants, potential, and reaction rates to the CL efficiency, water retention capability, and Pt utilization. The HOR reaction is known for its facile reaction rates and the Butler-Volmer (BV) equation is usually used for modeling its kinetics. However, in exploring the effect of Pt-loading on the anode reaction kinetics, Gasteiger et al. [39] decreased the anodic Pt-loading from 0.4 to 0.05 mg/cm^2 without discernible voltage loss, while a voltage loss in the order of 30 mv is expected from BV equation. This discrepancy initiates the development of a dual-pathway kinetic equation for HOR [40]. While the dual-pathway model and its improved versions provide a sufficient understanding of HOR kinetics, the impact of HOR reaction kinetics on overall cell performance is negligible. On the other hand, the sluggishness of ORR kinetics requires more complicated models. Numerous models considered the BV, Tafel, or modified Tafel equations for ORR kinetics. More recently, the double-trap (DT) models have become popular for studying the ORR kinetics [41], however, more developments are necessary for DT models.

The impact of cell design variables on ORR kinetics modifies under different operating conditions. For instance, the ionomer properties significantly vary with the operating condition including the temperature and relative humidity. Moreover, the formation of a water film surrounding the active reaction sites and the ionomer film is another issue that is undoubtedly affected by the operating conditions, specifically the input relative humidity [38]. Since the interpretation of in-situ experiments is intrinsically affected by various

aspects including operating conditions, transport limitation at high current densities, and the modification in ionomer transport properties, a comprehensive understanding of ORR kinetics remains a work to progress both numerically and experimentally.

The cell-level models include a wide range of spatial dimensions, including 0D, 1D, pseudo-2D, 2D, pseudo-3D, and 3D. While there is no spatial distribution consideration in 0D, 1D models include spatial distribution of variables in through-the-membrane or flow directions [42]. Using a 1D model, Pasaogullari et al. [43] investigated the effect of GDL wettability and cathode flooding on cell performance. The computational modeling of fuel cells was expanded to a 2D model by Fuller et al. [44], by developing a 2D membrane electrode assembly for the analysis of water and thermal management as well as hydrogen consumption. 2D models usually focus on through-the-membrane directions while incorporating either along-the-channel or in-plane dimensions. On the other hand, the P2D models consider through-the-membrane directions while the along-the-channel direction is evaluated based on the boundary conditions. Furthermore, 3D models encompass the transport phenomena in all physical directions, offering the highest fidelity and computational cost. For engineering and design purposes, the computational efficiency of the model and its ability to reproduce experimental findings are equally noteworthy. To reduce the computational cost and complexity, 3D models often are utilized for a fuel cell section [45][46][47] or simplifications are applied for different processes [48]. A balance between the model's computational efficiency and fidelity is provided using P3D models. In these models usually, the species transport is considered in two directions while considering the through-the-membrane direction through either boundary conditions or fluxes. In this regard, the effect of species distribution, water transport, and flow field design has recently been investigated using various P3D models [49][50]. A good example of such models is the P3D model developed by Rizvandi et al. [50], in which the through-plane direction is considered using the resistive relationships while the fuel cell plane has been assumed as a thin 2D layer.

The literature proposes the prevalence of steady-state models for PEM fuel cells [50][51][52]. However, the growing interest in the investigation of the dynamic response of PEMFCs witnessed the emergence of numerous transient models [10][23][53]. The transient transport phenomena, therefore, is investigated using dynamic models to investigate the effect of operating conditions, membrane properties [54], and flow field design

characteristics [55][56][23]. Notably, Grotsch et al. [57] developed a 1D through-the-membrane model incorporating the two-phase flow for studying the transient response of PEMFCs, while neglecting the temperature distribution and species distribution along the channel. Moreover, Promislow et al. [58] developed a dynamic model incorporating temperature distribution, along-the-channel transport, and two-phase flow characteristics. The authors considered the CL as an interface, neglecting the complicated transport within the active reaction sites [58]. Capturing the most salient feature of cell dynamics, however, requires a comprehensive transient model to delineate the critical transient phenomena [59]. Indeed, a notable research gap still exists in the fuel cell modeling literature for effectively balancing the level of fidelity in representing real-world physical processes with computational cost. Achieving this balance is crucial for providing accurate and practical insights into fuel cell behavior.

1.2.5 Literature Survey on Durability of PEM Fuel Cells

The primary bottleneck regarding the commercialization of FCEVs lies in the cost-intensive production of essential components, particularly the reliance on noble metals such as Pt to achieve a high catalytic activity in the CL, as well as their shortened lifetime. To ensure a sustainable mass production for FCEVs, according to the Department of Energy (DOE) targets, the amount of Pt-loading needs to be decreased below 0.1 mg/cm^2, while the durability target of 8000-hour operation with less than 10% loss is required [60].

Durability improvements are required for the commercial viability of PEMFCs as well as the Pt-loading decrement, and the cathode CL degradation is a deterministic factor in the shortened lifetime of the devices. Three main mechanisms describe the degradation of PEMFCs including mechanical, chemical, and electrochemical processes, with the latter being the main contributor to the performance loss. Under voltage cycling conditions between the open-circuit voltage and the optimum operating point, meaning voltages ranging from 0.5 to 0.7 V, Pt becomes electrochemically unstable and dissolved Pt^{2+} ions migrate through the CL or even longer to the membrane, modifying the Pt distribution and causing severe performance losses [11]. Under these cycling conditions, three possible mechanisms contribute to CL degradation including Pt dissolution, Pt redeposition,

and Pt migration to the membrane [25][11][61]. Another major contributor to fuel cell degradation is the oxidation of carbon black used as the support material during start-up and shut-down conditions. The air is available in both electrodes during shut-down while immediately after introducing the hydrogen to the front part of the anode channel, the hydrogen oxidizes and the cell voltage increases to around 0.85 V [62]. The remaining oxygen in the anode channel lowers the electrolyte potential to maintain the interfacial potential difference, which results in carbon corrosion, loss of ECSA, and reduced CL electrical conductivity [62]. Since the degradation happens over a long period, accelerated stress tests (ASTs) are often used to investigate the material's durability over a shorter period. Using different AST protocols, various studies evaluated CL electrochemical degradation concerning influential aspects including upper and lower potential limits [28][63], CL properties [25][64][65][66], the shape of potential sweep [67][68], utilized reactants [67][69], and operating conditions [70].

Different AST protocols help isolate the influential parameters and provide more insights for improved understanding. Harzer et al. [64] studied the effect of AST potential sweep shape using CLs with 0.1 and 0.4 mg/cm^2 Pt-loadings using different Pt-to-Carbon (Pt/C) ratios to realize the same CL thickness. Authors observed stronger ECSA loss for low catalyst loading and attributed this observation to the different aging behavior for Pt nanoparticle batches [64]. Moreover, the authors reported a rapid loss of ECSA and mass activity using square waves, mainly due to higher dwell time. During the Pt-dissolution mechanism and high potential, the Pt particles oxidize and reduce [64]. Since the dissolution occurs during oxide layer reduction, triangular waves with an upper potential limit equal to or greater than 0.95 V are found to cause higher dissolution rates [71], for which the amount of dissolved Pt is inversely proportional to the scan rate [72]. Furthermore, Uchimura et al. [67] reported the independence of Pt-dissolution from the cycle duration and its severe dependency on the number of cycles in the H_2/N_2 environment. In addition, Zihrul et al. [63] detailed slightly higher ECSA loss rates for longer hold time at high potential in the H_2/N_2 environment. In the H_2/air environment, however, the ECSA loss doubled for extending high potential hold from 3 to 60 s [63]. The effect of voltage cycling parameters including voltage sweep shape, lower potential, and cycling temperature are further studied by Kneer et al. [73]. The authors investigated significant Pt redistribution caused by Pt particle growth, Pt band formation in the membrane, and a Pt-depleted

layer at the interface of the electrode-membrane, while the CL pore size distribution and thickness were barely affected by the voltage cycling [73]. Among all, Pt particle growth was introduced as the main contributor to the performance loss resulting in ECSA fade and consequently, the performance fade [73]. Based on understanding such fundamentals of degradation mechanism, efforts have been tailored to evaluate the effect of CL microstructural characteristics. Schneider et al. [25] studied the impact of CL morphology including the CL thickness and Pt-loading on the degradation of PEMFCs. They reported a higher loss trend for low Pt-loaded cells due to a higher depletion zone at the membrane-electrode interface, which results in higher Pt and ECSA loss [25]. Considering different mass fractions of bare carbon particles, they attributed higher ECSA loss rates to diluted CLs with lower Pt/C ratios which originates from an increased Pt dissolution per Pt particle [25]. However, contrary results are observed by doping the CL with commercial carbon powders by Wang et al. [66]. The authors represented a higher utilization rate of Pt upon increasing the CL thickness twofold using Pt-loading of 0.1 mg/cm^2 [66].

As another degradation mechanism, corrosion of carbon support material is a primary degradation mechanism leading to secondary processes such as detachment and agglomeration of Pt nanoparticles, and the modification of the CL morphology. During the operation of PEMFCs including local fuel starvation, startup, and shutdown processes, the reverse-current mechanism explains the carbon corrosion process. To gain insight on the performance loss during a carbon corrosion AST, Hegge et al. [74] cycled the MEAs in an H_2/N_2 environment between potential ranges of 1 to 1.5 V. Authors attributed the majority of performance loss to the increased mass transport resistances (MTR) resulting from the CL structural modifications including the pore space change, water uptake, and interfacial resistances, respectively [74]. Moreover, the majority of the MTR increase is attributed to the local MTR hike caused by the loss of active area [74]. Considering the local potential distribution in porous electrodes as well as the transport rates, the degradation of thick electrodes may differ from that of thin ones. With this hypothesis, Darab et al. [75] investigated the effect of CL thickness on the degradation of PEMFCs using a triangular AST within a voltage range of 0.6 to 1.5 V encompassing both Pt-dissolution and carbon corrosion mechanisms. The authors represented similar ECSA relative loss for three different utilized Pt/C ratios concluding the independence of ECSA Loss from the CCL thickness [75]. Nonetheless, the authors detailed performance reduction depen-

dency on the Pt/C ratio with 10 wt.% ratios representing the highest voltage reduction [75]. In addition, Macauley et al. [28] examined the carbon corrosion mechanism using three different carbon support materials. The authors observed a severe reduction of CL thickness and porosity which is attributed to the compaction of the CL material rather than carbon oxidation [28]. Moreover, the authors reported dependency of degradation rates on the degree of graphitization within the initial carbon black material [28]. Furthermore, Li et al. [76] investigated higher performance reduction for limiting current densities due to the enhanced ohmic resistances using a startup and shutdown simulator AST. The authors also found that carbon corrosion induced a significant influence on the CL mechanical properties [76].

The aforementioned literature review and the contrary results provided regarding the impact of CL features on electrode degradation require deep fundamental experimental work to elucidate the impact of CL characteristics separately and provide insights on the CL feature interplay.

1.3 Contributions

The literature review provided above offers insights into the extensive research conducted on various aspects of PEMFC development. However, it also highlights the presence of opportunities for further advancements. Notably, there appears to be a disconnect between the electrochemical research aimed at enhancing the scientific understanding and design of PEM fuel cells, and their degradation. Consequently, this dissertation seeks to bridge this gap by establishing a deep understanding of the CL microstructural characteristics, and their effect on the performance and degradation of PEM fuel cells. The primary research objectives of this dissertation are listed below.

- Developing a computationally efficient, physics-based model for evaluating the performance of PEM fuel cells, with an emphasis on low Pt-loaded cells. To capture all the involved transport properties and the distribution of critical variables within all layers, the model encompasses the detailed transport processes in different involved layers including channels, GDLs, CLs, and PEM.

- Investigation of the impact of CL design variables including the Pt-loading, Pt/C ratio, dilution ratio, and I/C ratio, controlled in the fabrication process, on the performance of low Pt-loaded PEM fuel cell. The transport resistances of oxygen and protons as well as the performance of a cell portion with straight cathode and anode channels are evaluated using a non-isothermal multiphase pseudo-three-dimensional PEMFC model. The model is validated against systematic experimental data available in the literature and used to investigate the effects of microstructural parameters of the cathode CL.

- Developing and validating a transient model, with an emphasis on low Pt-loaded cells and investigation of CL microstructural characteristics as well as operating conditions on the transient response of PEMFCs. Specifically, the development of a multiphase non-isothermal P3D dynamic model coupled with a detailed electrochemical kinetic model to evaluate the cell transient response under the Galvanodynamic condition.

- Fabrication of catalyst-coated-membranes (CCMs) with different Pt-loadings and CL characteristics, using ultrasonic spray coating method for ensuring the repeatability, good porosity, homogeneity, and perfect distribution of Pt nanoparticles within the deposited layer. Moreover, investigation of the impact of operating conditions and CL characteristics on the performance and transport resistances within various MEAs using various electrochemical characterization methods including polarization curves, linear sweep voltammetry, cyclic voltammetry, and electrochemical impedance spectroscopy.

- Investigating the electrode degradation including the Pt-dissolution and Carbon Corrosion in PEM fuel cells with different CL characteristics. Of great interest is a systematic experimental approach for isolating the interplay within intricate CL features and evaluating the sole impact of each characteristic on ECSA and performance loss.

1.4 Thesis Outline

The thesis is composed of 6 chapters in total including this chapter, which consists of the corresponding introduction, methodologies, obtained results and discussion, and concluding remarks.

In chapter 2, a pseudo-three-dimensional (P3D) model is developed with detailed electrochemical kinetic and two-phase flow sub-models accounting for the characteristics of different porous layers. After careful validation of the model under various operating conditions for different catalyst design variables against the available experimental data, the CL characteristics and operating conditions are studied to investigate the impact of each parameter on the cell steady-state performance. Moreover, the origins of increased oxygen transport resistance of low Pt-loaded samples are investigated.

In chapter 3, the proposed P3D model is extended to a transient one under Galvanodynamic mode. The model accuracy is evaluated for different step currents, and the impact of CL characteristics and operating conditions on the dynamics of cell behavior is studied.

In chapter 4, the development of low Pt-loaded MEAs with various CL characteristics is explained. The details of the experimental methods including the catalyst coating and optimization of the ultrasonic deposition method are explained. In addition, the details of utilized in-situ characterizations are provided. The results section of this chapter compares the performance of samples with different CL thicknesses, Pt/C ratios, Pt-loadings, and carbon support materials.

Chapter 5 assesses the durability of samples with various CL characteristics against both Pt-dissolution and carbon corrosion degradation mechanisms. Two different accelerated stress tests are utilized to simulate the Pt-dissolution and carbon corrosion degradation mechanisms, and the impact of CL thickness, Radii of Pt nanoparticles, Pt/C ratio, Pt-loading, and carbon support materials are investigated. Moreover, a P3D model with serpentine channels is utilized to reproduce the experimental data.

Finally, chapter 6 presents the concluding remarks and the future works of this thesis research.

Chapter 2

A DETAILED EFFICIENT PEMFC MODEL ACCOUNTING FOR MICROSTRUCTURAL CHARACTERISTICS OF DIFFERENT LAYERS

2.1 Introduction

Fuel cell development and commercialization rely on the critical decisions affecting the fuel cell performance and durability, and mathematical modeling and numerical simulation provide a framework for evaluating the transport processes, which consequently affect these decisions. This motivates the necessity of a PEMFC model, capturing the involved processes and their effect, with a reasonable computation cost, while incorporating the essential microstructural features of the multiple involved layers.

As discussed in chapter 1, a research gap exists in the literature, concerning the fuel cell models which effectively balance the computational cost and fidelity, and simultaneously provide insights regarding the characteristics of multiple involved processes. To address this gap, the chapter aims to develop a P3D fuel cell model tailored for catalyst morphology, operating conditions, and geometrical evaluations. The model takes advantage of distinct microscale models including the detailed electrochemical kinetics model, capturing the transport resistance within the CL, as well as a mixed wettability pore size distribution (PSD) mathematical model to account for the transport properties of the porous layer and effectively modeling the two-phase flow. The model capability in predicting the performance and oxygen transport resistances is evaluated by validating the polarization curves in a small fuel cell portion, comprising straight channels, GDLs, CLs, and the PEM, with experimental data in the literature for various operating conditions and

catalyst morphological characteristics.

The rest of this chapter is organized as follows. Section 2.2 presents the model formulation outlining the steps taken to develop this model including the modeling domain, governing equations, the microscale sub-models, numerical implementation, and model validation with available experimental data. Section 2.3 provides the simulation case studies including the operating conditions, CL features, and flow field design considerations. The last section includes the summary and remarking conclusions of this chapter.

2.2 Model Development

2.2.1 Modeling Domain

A two-dimensional computational domain including the straight channels, GDLs, CLs, and ribs is considered. The modeling domain of interest is assumed to be projected on a single surface as shown in Figure 2.1. Due to the symmetry, the channels and ribs of the cathode and anode sides overlap. Since the channel length effect is minimal for straight channel designs, a cell portion with a length of 1 cm is considered in this work for computational efficiency. An introduction to the physical model is provided in this section while the saturation and electrochemical sub-models are covered in sections 2.2.3 and 2.2.4, respectively.

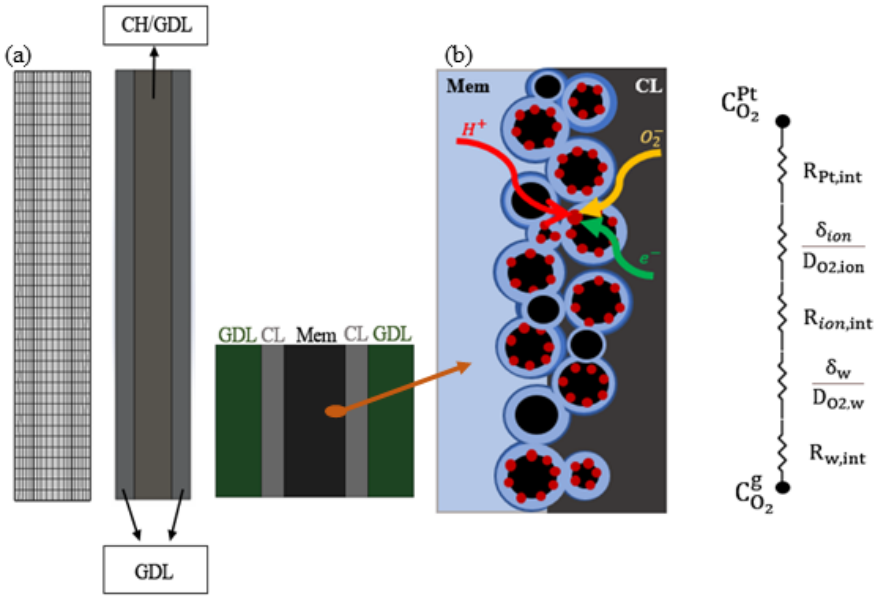

Figure 2.1: (a) Computational domain together with involved layers and mesh distribution, (b) The CL structure and the included oxygen transport resistances representing catalyzed particles (black carbon with red Pt particles) and the additional bare carbon particles [77]

The height-averaged equations including conservation of mass, momentum, energy, species, and liquid pressure are coupled and simultaneously solved in the GDLs and channels explicitly. However, these equations are evaluated in the CL by considering the transport resistances from GDL to CL as well as source terms in the CL. In addition, the membrane is treated as a thin layer resisting the transport of ions while facilitating the transport of dissolved water through adsorption and desorption processes.

2.2.2 Governing Equations

The present model solves mass, momentum conservations, species, ionomer dissolved water, energy, and liquid pressure equations. All the governing equations are provided in Table 2.1 while the utilized parameter values are provided in Table 2.3.

Table 2.1: Governing equations

Description	**Equation**	
Mass Conservation	$\nabla \cdot (\rho \mathbf{u}) = S_{mass}$	(2.1)
Momentum Conservation	$\rho \mathbf{u} \cdot \nabla \mathbf{u} = -\nabla p + \mu \nabla^2 \mathbf{u} - \frac{\mu}{\kappa} \mathbf{u}$	(2.2)
Species Distribution	$\nabla \cdot \left(-\rho \, w_i \sum_j D_{ij} \, \nabla X_j \right) + \rho \, (\mathbf{u} \cdot \nabla) \, w_i = S_i$	(2.3)
Electronic Potential	$\nabla \cdot (-\sigma_s \nabla \phi_s) = S_{\phi_s}$	(2.4)
Ionic Potential	$\nabla \cdot (-\sigma_m \nabla \phi_m) = S_{\phi_m}$	(2.5)
Dissolved Water	$\nabla \cdot \left(\frac{-\rho_{mem}}{EW} \, D_{H2O}^{Naf} \nabla \lambda \right) + \nabla \cdot \left(\frac{-n_d}{F} \, \sigma_l \nabla \phi_l \right) = S_\lambda$	(2.6)
Energy Conservation	$(\rho \, C_p)_{eff} \, \mathbf{u} \cdot \nabla T + \nabla \cdot (-k_{eff} \nabla T) = S_T$	(2.7)
Liquid Water	$\nabla \left(\frac{\rho_l k_l}{\mu_l} \nabla p_l \right) = S_l$	(2.8)

Equations 2.1 and 2.2 describe Navier-Stokes equations used to obtain pressure p and velocity $\mathbf{u}$ fields while inertial terms are neglected for flow through porous GDLs. In equation 2.2, ρ, κ, and μ are the density, porous medium permeability, and the dynamic viscosity, respectively. The distribution of species is obtained from the Maxwell-Stefan equation described in equation 2.3 in which D_{ij} is the binary diffusion coefficient of species, and w_i is the mass fraction of species. The flow distribution is evaluated by solv-

ing the conservation of mass, momentum, and species simultaneously by considering the convective and diffusive fluxes between channels and GDLs. In addition, mass sources resulting from the electrochemical reaction, water phase change process, and dissolved water in the electrolyte phase are considered as the through-plane (TP) fluxes. Conservation of charge, equations 2.4 and 2.5, are solved for electric and ionic potentials. Equation 2.6 governs the transport of liquid phase water through ionomer considering adsorption, desorption, water generation caused by the electrochemical reaction, and electro-osmotic drag processes where $D_{H_2O}^{Naf}$ is the water diffusion coefficient in the ionomer phase, λ is the dimensionless number representing the number of water molecules per sulfonic acid groups, and n_d is the electro-osmotic drag coefficient. In addition, based on a 3-degree-of-freedom (DOF) finite difference equation, an approximation of equation 2.6 solution in through-plane direction is obtained to ensure the continuity of the flux of dissolved water with the flux from the source terms at anode and cathode GDLs [50].

$$-\frac{\rho_{mem}}{EW} D_{H_2O}^{Naf,an} \frac{-3\lambda_{an} + 4\lambda_{mem} - \lambda_{ca}}{\delta_m} + \frac{2.5}{22}\lambda_{an}\frac{j_{cell}}{F} = S_\lambda^{an}\, h_{GDL} \tag{2.9}$$

$$-\frac{\rho_{mem}}{EW} D_{H_2O}^{Naf,ca} \frac{3\lambda_{ca} - 4\lambda_{mem} + \lambda_{an}}{\delta_m} + \frac{2.5}{22}\lambda_{ca}\frac{j_{cell}}{F} = S_\lambda^{ca}\, h_{GDL} \tag{2.10}$$

$$\begin{aligned} -\frac{\rho_{mem}}{EW} D_{H_2O}^{Naf,an} \frac{-3\lambda_{an} + 4\lambda_{mem} - \lambda_{ca}}{\delta_m} + \frac{2.5}{22}\lambda_{an}\frac{j_{cell}}{F} = \\ -\frac{\rho_{mem}}{EW} D_{H_2O}^{Naf,ca} \frac{3\lambda_{ca} - 4\lambda_{mem} + \lambda_{an}}{\delta_m} + \frac{2.5}{22}\lambda_{ca}\frac{j_{cell}}{F} \end{aligned} \tag{2.11}$$

Equation 2.7 is the energy conservation equation governing the temperature of the computational domain in which k_{eff} is the effective thermal conductivity and C_p is the specific heat capacity defined for both reactants and solid phases. Temperature difference over GDLs evaluated considering the heat generation of the electrochemical reaction and the heat losses due to the overpotential and phase change process. Moreover, the source terms include the heat transfer through the CL due to the temperature difference between the cathode and anode GDLs, and the heat fluxes from GDL to channels and ribs. The transport of liquid water through GDLs is governed by equation 2.8 where the pressure drop of the liquid phase is calculated based on Darcy's law approximations. The mixed wettability model is used for relating saturation and liquid pressure, and it is further explained in section 2.2.3. The source terms for all the equations are provided in Table 2.2.

Table 2.2: Source terms for governing equations

Source terms

$$S_{mass}\left(\frac{kg}{m^3\,s}\right) = \begin{cases} \dfrac{-M_{H_2O}\,i_{an}}{2F} - M_{H_2O}\,S_\lambda & \text{Anode CL} \\ \dfrac{-M_{O2}\,i_{ca}}{4F} - S_{phase} & \text{Cathode CL} \\ -S_{phase} & \text{Cathode CH and GDL} \end{cases} \tag{2.12}$$

$$S_i\left(\frac{kg}{m^3\,s}\right) = \begin{cases} \dfrac{-M_{H_2}\,i_{an}}{2F} & \text{Anode CL} \\ -M_{H_2O}\,S_\lambda & \text{Anode CL} \\ \dfrac{-M_{O_2}\,i_{ca}}{4F} & \text{Cathode CL} \\ -S_{phase} & \text{Cathode CH, GDL, and CL} \end{cases} \tag{2.13}$$

$$S_{\phi_s}\left(\frac{A}{m^3}\right) = \begin{cases} -i_{an} & \text{Anode CL} \\ +i_{ca} & \text{Cathode CL} \end{cases} \tag{2.14}$$

$$S_{\phi_m}\left(\frac{A}{m^3}\right) = \begin{cases} +i_{an} & \text{Anode CL} \\ -i_{ca} & \text{Cathode CL} \end{cases} \tag{2.15}$$

$$S_\lambda\left(\frac{mol}{m^3\,s}\right) = \begin{cases} \dfrac{k_{ads}}{\delta_{CL}}\dfrac{\rho_{mem}}{EW}(\lambda^{eq}-\lambda) & \text{Anode CL} \\ \dfrac{k_{des}}{\delta_{CL}}\dfrac{\rho_{mem}}{EW}(\lambda^{eq}-\lambda) + \dfrac{i_{ca}}{4F} & \text{Cathode CL} \end{cases} \tag{2.16}$$

$$S_T\left(\frac{W}{m^3}\right) = \begin{cases} i\,(\eta_{an}) + \sigma_m^{CL}(\nabla\phi_m)^2 + \sigma_s^{CL}(\nabla\phi_s)^2 & \text{Anode CL} \\ i\left(\eta_{ca} + T\dfrac{dE}{dT}\right) + \sigma_m^{CL}(\nabla\phi_m)^2 + \sigma_s^{CL}(\nabla\phi_s)^2 + h_{fg}S_{liq} & \text{Cathode CL} \\ \sigma_{GDL}^{th}(\nabla\phi_s)^2 & \text{Anode GDL} \\ \sigma_{GDL}^{th}(\nabla\phi_s)^2 + h_{fg}S_{liq} & \text{Cathode GDL} \\ \sigma_{GDL}^{mem}(\nabla\phi_m)^2 & \text{PEM} \end{cases} \tag{2.17}$$

$$S_{phase}\left(\frac{kg}{m^3\,s}\right) = \begin{cases} k_{cond}\Delta p\dfrac{\varepsilon_{GDL}(1-s)x_{H_2O}M_{H_2O}}{RT} & \Delta p \geq 0 \\ k_{evap}\Delta p\,\varepsilon_{GDL}\,\rho\,s & \Delta p \geq 0 \end{cases} \tag{2.18}$$

$$S_l\left(\frac{kg}{m^3\,s}\right) = \begin{cases} k_{flux}\left(\dfrac{p_l - p_{l,CH}}{p_0}\right)g(p_l) & \text{CHs} \\ M_{H_2O}S_{phase} + \dfrac{\rho_w\,(p_{l,CH} - p_l)}{\delta_{GDL}R_l} & \text{Cathode CL} \end{cases} \tag{2.19}$$

In these equations, i_{ca}, and i_{an} are the volumetric reaction rates of cathode and anode, respectively and are described in section 2.2.4. In equation 2.16, k_{ads} and k_{des} represents the adsorption and desorption coefficient given by [78],

$$k_{ads} = 1.14 \times 10^{-5} \, f_v \exp 2416 \left(\frac{1}{T_{ref}} - \frac{1}{T} \right) \tag{2.20}$$

$$k_{des} = 4.59 \times 10^{-5} \, f_v \exp 2416 \left(\frac{1}{T_{ref}} - \frac{1}{T} \right) \tag{2.21}$$

where f_v is the volumetric ratio of liquid water in electrolyte phase [50]. Moreover, in equation 2.19, $p_{l,CH}$ is considered as the atmospheric pressure [17], p_0 is a nondimensional factor with the value of 1 Pa [17], k_{flux} is assumed to be 8×10^{-4} g⁄cm^{2}s [10], and $g(p_l)$ is defined as [17],

$$g\left(p_l\right) = \left(\frac{\tanh\left(\frac{p_l - p_{l,CH}}{p_0}\right) + 1}{2} \right) \theta\left(p_l - p_{BT}\right) \tag{2.22}$$

Equation 2.22 assumes a breakthrough pressure p_{BT}, defined as 2000 Pa above which a proportional water flux is applied using the step function $\theta\left(p_l - p_{BT}\right)$. Thus, the water flux is set to be zero for values of p_l smaller than p_{BT} while it is kept constant for higher values, following the experimental findings of Ref. [79]. Although governing equations are not solved for the MPL, the resistive relations are considered to incorporate their effect on liquid pressure and water saturation. In equation 2.19, p_l is the pressure of the liquid phase in GDL, and R_l is the resistive term defined as,

$$R_l = \frac{\mu}{2} \left(\frac{\delta_{CL}}{k_{l,CL}} + \frac{\delta_{GDL}}{k_{l,GDL}} + \frac{\delta_{MPL}}{k_{l,MPL}} \right) \tag{2.23}$$

where $k_{l,X}$ is the effective liquid permeability of the porous layer X. Moreover, $p_{l,CL}$, defined as the liquid pressure in the CL, is obtained by considering the production of water from the electrochemical reaction, the water uptake in the membrane, and water transport to GDL, while transport resistance of GDL, CL, and MPL are included.

$$\frac{j_{cell}}{2F} - \frac{\rho_{mem}}{EW} D_{H_2O}^{Naf} \nabla\lambda - \frac{\rho_w \left(p_{l,CL} - p_l\right)}{R_l} = 0 \tag{2.24}$$

A detailed description of the approach utilized in this model and validation against a full

three-dimensional model can be found in Ref. [50]. The related geometrical, physical, and operational parameters are reported in Table 2.3.

Table 2.3: Geometrical, physical, and operational parameters and their base values

Description	**Parameter**	**Value**	**Unit**
Channel length, width, height	L_{CH}, w_{CH}, h_{CH}	10, 1, 1	mm
Land width	w_{rib}	1	mm
Thickness of PEM [5]	δ_{mem}	18	µm
Density of PEM, Pt, carbon, ionomer [38]	$\rho_{mem}, \rho_{Pt}, \rho_C, \rho_{ion}$	1.98, 21.45, 1.95, 1.9	g/cm^3
Equivalent weight of PEM	EW	950	g/mol
Porosity of GDL [80], MPL [17]	$\varepsilon_{GDL}, \varepsilon_{MPL}$	0.78, 0.42	—
Absolute permeability of GDL, MPL, CL [81]	$\kappa_{GDL}, \kappa_{MPL}, \kappa_{CL}$	8×10^{-12}, 1.3×10^{-13}, 2×10^{-17}	m^2
Thermal conductivity of GDL [82]	$k_{GDL,TP}, k_{GDL,IP}$	1.7, 21	W/m K
Thermal conductivity of PEM [83]	k_{mem}	0.27	W/m K
Electrical conductivity of GDL [52]	$\sigma_{GDL,TP}, \sigma_{GDL,IP}$	500, 5000	S/m
Electrical conductivity of CL [52]	σ_{CL}	500	S/m
Condensation coefficient [46]	k_{cond}	1	1/s
Evaporation coefficient [46]	k_{evap}	5×10^{-5}	1/Pa s
Inlet stoichiometry ratios for cathode,anode	st_{ca}, st_{an}	1.5, 2	—
Inlet relative humidity for cathode, anode	RH_{ca}, RH_{an}	1, 1	—
Operating and reference temperature	T, T_0	353, 298	K
Operating and reference pressure	P, P_0	1, 1.5	atm

The values of the rest of the parameters utilized in this work are reported in Ref. [50][77], and the description of the variable within this document is provided in nomenclature.

2.2.3 Mixed Wettability Pore Size Distribution Model

Understanding the interaction between the phase change process and water transport through the cell with operating conditions and material properties is of great interest. Saturation, defined as the volume fraction of liquid water, is related to the capillary pressure through closure equations for which two approaches are commonly used. Through the first approach, Darcy's law written in terms of liquid pressure is modified for liquid saturation while the Leverett-J function is used as the closure equation [84]. The Leverett-J function is an empirical relation acquired from material analysis of sand which is a highly hydrophilic (HI) porous material [46]. Nevertheless, optimization of the porous layer structure is difficult using this relation [17]. For the second approach, the multiphase flow is considered to solve the conservation equations for mass and momentum for liquid and gas phases. These phases are later related by closure equations obtained from the pore size distribution (PSD) in the micro-structure [85][17].

PSD is commonly considered the metric to characterize transport properties [85]. Initially, Weber et al. [34] developed identical PSDs for both hydrophilic (HI) and hydrophobic (HO) pores assuming pores as a bundle of rejoined capillaries. Later, Weber [35] improved the model by including a Gaussian contact angle distribution for better computational convergence and accuracy. In addition, Eikerling [86] developed a similar micro-structural model to study the multiphase flow considering primary and secondary pores in the CL. Villanueva [87] considered two distinct PSDs for HI and HO pores, and Zhou et al. [17] incorporated these PSDs into a mathematical model to investigate the effect of adding an MPL on the cell performance under different temperatures.

In this study, the mixed wettability PSD model is used from Ref. [17][87], where effective properties of porous layers such as water retention curve, effective liquid, and gas permeabilities, interfacial liquid-gas surface area, and Knudsen radius are obtained from the microstructural properties of the layers including pore radius, volume fraction, and contact angle. Model equations and mathematical formulations are provided in this section while the detailed microstructural characteristics of layers are given in Table 2.4. Mathematical calculations of the model are conducted offline, and the interpolated figures are included afterward. Different materials used as GDL including carbon paper and cloth have distinct PSDs which is confirmed by Luo et al. [88], and the wet proofing modifies

the porosity and structure of the porous layers. Herein, the properties of Mitsubishi Ryan Co. (MRC-105) are used for validating simulations with experiments of Ref. [5]. Moreover, microstructural features of Toray090 are used for obtaining the results section. Since Knudsen diffusion is dominant in small pores, the Knudsen radius is only calculated for CL.

PSD models are widely used for estimating the effective transport properties of porous media under wet and dry conditions [89]. The change of cumulative pore volume fraction is related to the pore size using a variety of algebraic functions. The log-normal distribution functions are commonly used due to their capability to represent the experimental findings, which helps in deriving analytical expressions for effective properties of CLs and GDLs. Since the pore distribution of hydrophilic (HI) and hydrophobic (HO) pores differs [90], two distinct wettabilities and PSDs are considered for pores, with an associated contact angle distribution for each. The overall PSD for a porous layer is,

$$\frac{dX(r)_{HI}}{dr} = F_{HI} \sum_k \left[\frac{f_k}{r s_k \sqrt{2\pi}} \exp\left(-\frac{(\ln(r) - \ln(r_k))^2}{2\, s_k^2} \right) \right] \tag{2.25}$$

$$\frac{dX(r)_{HO}}{dr} = F_{HO} \sum_k \left[\frac{f_k}{r s_k \sqrt{2\pi}} \exp\left(-\frac{(\ln(r) - \ln(r_k))^2}{2\, s_k^2} \right) \right] \tag{2.26}$$

where $\frac{dX(r)_i}{dr}$ is the normalized pore volume and F_i represents the total volume fraction occupied with pores with wettability of i with the summation of F_{HI} and F_{HO} being 1, which is either HI for hydrophilic pores or HO for hydrophobic ones. The $f_{i,k}$ is the contribution of distribution k to the overall i distribution, $r_{i,k}$ is the pore size characteristics of distribution k in the i PSD, and $s_{i,k}$ is the spread of distribution k. These functions for hydrophilic and hydrophobic pores have the same definition, while the values utilized for their characteristics differ.

Table 2.4: Pore size distribution characteristics for porous layers

Parameter		**Value**				
		GDL [80] MRC-105	GDL [17] Toray090	CL [81] GKB	MPL [87]	GDL[87] Sigracet 34BA
Pore radii (μm)	r_1	9.55	18	0.002	0.0382	34
	r_2	13.09	23	0.006	0.125	14.2
	r_3	—	—	0.025	0.5	—
	r_4	—	—	0.080	1.2	—
	r_5	—	—	—	2	—
Pore widths	s_1	0.484	1.2	0.6	0.43	0.35
	s_2	0.296	0.2	0.6	0.55	1
	s_3	—	—	0.45	0.65	—
	s_4	—	—	0.8	0.45	—
	s_5	—	—	—	0.75	—
Pore fractions	f_{r1}	0.611	0.6	0.05	0.31	0.72
	f_{r2}	0.389	0.4	0.12	0.18	0.28
	f_{r3}	—	—	0.73	0.1	—
	f_{r4}	—	—	0.10	0.05	—
	f_{r5}	—	—	—	0.36	—
HI volume fraction	F_{HI}	0.08	0.05	0.3	0.1	0.1
HI contact angle	θ_{HI}	70	70	55	84	45
HO contact angle	θ_{HO}	120	130	91	93	110

The summation of equations 2.25 and 2.26 gives the overall PSD distribution of the respective layer, as represented in 2.25, which is the final form of the PSD.

$$\frac{dX(r)}{dr} = \frac{1}{V_T}\frac{dV(r)}{dr} \tag{2.27}$$

The parameters in PSDs are derived using intrusion porosimetry methods with different fluids, used in different areas to study porous materials' structure and wettability

behavior [90][91]. Upon use of mercury, a hydrophobic fluid for most materials, the overall PSD is extracted while water is the working fluid for extraction of hydrophobic (HO) PSD [87]. The Young-Laplace equation is later used for relating the capillary pressure to an effective pore size,

$$r_C = \frac{-2\gamma \cos\theta}{P_C} \tag{2.28}$$

where r_c is the critical radius for the incipiently filled pore which is the largest value for the hydrophilic (HI) pores ($\theta < \frac{\pi}{2}$) and the smallest one for the hydrophobic (HO) pores ($\theta > \frac{\pi}{2}$). In addition, γ is the surface tension of water in units of N/m, and P_C is the capillary pressure. Capillary pressure is calculated as,

$$P_C = P_l - P_g \tag{2.29}$$

where P_l is the liquid pressure and P_g is the gas pressure. When the capillary pressure reaches zero value, all the hydrophilic (HI) pores are filled while all the hydrophobic (HO) pores are empty. By integrating the cumulative change of the pore volume fraction as a function of pore size for the whole domain, the saturation is obtained based on the capillary pressure measurements as,

$$S = S_{HI} + S_{HO} \tag{2.30}$$

$$S_{HI} = F_{HI} \sum_k \frac{f_{HI,r,k}}{2} \left[1 + \text{erf}\left(\frac{\ln(r_{C,HI}) - \ln(r_{HI,k})}{s_{HI,k}\sqrt{2}}\right)\right] \tag{2.31}$$

$$S_{HO} = F_{HO} \sum_k \frac{f_{HO,k}}{2} \left[1 - \text{erf}\left(\frac{\ln(r_{C,HO}) - \ln(r_{HO,k})}{s_{HO,k}\sqrt{2}}\right)\right] \tag{2.32}$$

As another transport property, the liquid relative permeability represents the readability of liquid phase movement through porous layers at different saturation levels. While absolute permeability of the different layers is the intrinsic property, provided in Table 2.3, the relative permeability is a function of saturation and capillary pressure and is defined as the ratio between liquid phase permeability and saturated permeability of the media. The saturated permeability can be obtained from the Hagen-Poiseuille equation and has a reverse relation with the interconnectivity of pores [17]. Higher values of liquid relative permeability show that liquid can flow through the media readily. Under the assumption

of randomly connected pores [87], the liquid relative permeability is obtained as,

$$k_{r,HI} = \frac{F_{HI}}{16}\left[\frac{\varepsilon_0\, S}{\lambda}\right]^2 \sum_k \exp\left(-2s_{HI,k}^2\right) r_{HI,k}^2\, f_{HI,k} \left[\operatorname{erf}\left(\frac{\ln\left(r_{C,HI}\right) - \ln\left(r_{HI,k}\right)}{s_{HI,k}\sqrt{2}} - s_{HI,k}\sqrt{2}\right) + 1\right] \tag{2.33}$$

$$k_{r,HO} = \frac{F_{HO}}{16}\left[\frac{\varepsilon_0\, S}{\lambda}\right]^2 \sum_k \exp\left(-2s_{HO,k}^2\right) r_{HO,k}^2\, f_{HO,k} \left[-\operatorname{erf}\left(\frac{\ln\left(r_{C,HO}\right) - \ln\left(r_{HO,k}\right)}{s_{HO,k}\sqrt{2}} - s_{HO,k}\sqrt{2}\right) + 1\right] \tag{2.34}$$

where ε_0 is the layer porosity and λ is a parameter defining the interconnectivity of pores which is assumed as 1.26 and 2 for the GDL and MPL, respectively [17]. The total liquid relative permeability of a layer is calculated by adding the contribution from both hydrophobic (HO) and hydrophilic (HI) pores as,

$$k_{r,L} = \frac{k_{L,HI} + k_{L,HO}}{k_{sat}} \tag{2.35}$$

where k_{sat} represents the saturated permeability. The liquid relative permeability is zero when the pores are empty from liquid; however, it is increasingly proportional to the fraction of accumulated water in the pores. The gas relative permeability is the permeability of the non-wetting phase, which is the gas phase, considered for both hydrophilic (HI) and hydrophobic (HO) pore networks. Consequently, the expressions used to calculate gas relative permeability are analogous to the final expressions of liquid relative permeability,

$$k_{G,HI} = \frac{F_{HI}}{16}\left[\frac{\varepsilon_0\,(1-S)}{\lambda}\right]^2 \sum_k \exp\left(-2s_{HI,k}^2\right) r_{HI,k}^2\, f_{HI,k} \left[-\operatorname{erf}\left(\frac{\ln\left(r_{C,HI}\right) - \ln\left(r_{HI,k}\right)}{s_{HI,k}\sqrt{2}} - s_{HI,k}\sqrt{2}\right) + 1\right] \tag{2.36}$$

$$k_{G,HO} = \frac{F_{HO}}{16}\left[\frac{\varepsilon_0\,(1-S)}{\lambda}\right]^2 \sum_k \exp\left(-2s_{HO,k}^2\right) r_{HO,k}^2\, f_{HO,k} \left[\operatorname{erf}\left(\frac{\ln\left(r_{C,HO}\right) - \ln\left(r_{HO,k}\right)}{s_{HO,k}\sqrt{2}} - s_{HO,k}\sqrt{2}\right) + 1\right] \tag{2.37}$$

Both empirical and geometrical considerations are used for proposing mixed wettability PSD for the liquid-gas interfacial area per unit volume, concerning the actual contact area between two phases at which the phase change reaction occurs. This area is zero if the porous medium is either completely saturated or unsaturated, while it reaches a maximum value for partially saturated pores. The liquid-gas interfacial area per unit volume is estimated using [17],

$$\frac{a(r)_{HI}}{V_T} = P_b\, F_{HI} \sum_k \frac{f_{k,HI} \exp\left(\frac{s_{k,HI}^2}{2}\right)}{8 r_{k,HI}} \left[1 + \operatorname{erf}\left(\frac{\ln\left(r_{cr}\right) - \ln\left(r_{k,HI}\right)}{s_{k,HI}\sqrt{2}} + \frac{s_{k,HI}\sqrt{2}}{2}\right)\right] \tag{2.38}$$

$$\frac{a(r)_{HO}}{V_T} = P_b\, F_{HO} \sum_k \frac{f_{k,HO} \exp\left(\frac{s_{k,HO}^2}{2}\right)}{8 r_{k,HO}} \left[1 - \operatorname{erf}\left(\frac{\ln\left(r_{cr}\right) - \ln\left(r_{k,HO}\right)}{s_{k,HO}\sqrt{2}} + \frac{s_{k,HO}\sqrt{2}}{2}\right)\right] \tag{2.39}$$

where P_b is a probability function used to include the effect of pore interconnectivity and is a function of saturation level in pores. The total liquid-vapor interfacial surface area per unit volume is evaluated as,

$$a(r)_T = \frac{a(r)}{V} = \frac{a(r)_{HI}}{V_T} + \frac{a(r)_{HO}}{V_T} \tag{2.40}$$

To obtain the wetted pore wall surface area, the contributions from both hydrophobic (HO) and hydrophilic (HI) pores are summed, considering that the total pores surface area is consistent with the lateral area of straight cylindrical micro and nanopores,

$$a_{wall,HI} = \sum_k \frac{F_{HI} f_{k,HI}}{r_{k,HI}} \exp\left(\frac{s_{k,HI}^2}{2}\right) \left[1 + \operatorname{erf}\left(\frac{\ln\left(r_{C,HI}\right) - \ln\left(r_{k,HI}\right)}{s_{k,HI}\sqrt{2}} + \frac{s_{k,HI}}{2}\right)\right] \tag{2.41}$$

$$a_{wall,HO} = \sum_k \frac{F_{HO} f_{k,HO}}{r_{k,HO}} \exp\left(\frac{s_{k,HO}^2}{2}\right) \left[1 - \text{erf}\left(\frac{\ln\left(r_{C,HO}\right) - \ln\left(r_{k,HO}\right)}{s_{k,HI}\sqrt{2}} + \frac{s_{k,HO}}{2}\right)\right] \tag{2.42}$$

As the last transport property calculated based on the mixed wettability pore size distribution (PSD) model, the Knudsen radius is defined as the effective pore radius,

$$r_{kn} = \frac{C_1 + C_2}{C_3 + C_4} \tag{2.43}$$

$$C_1 = \sum_k \left(\frac{F_{HI}\, f_k}{2}\right) \left[1 - \text{erf}\left(\frac{\ln\left(r_{C,HI} - \ln\left(r_{HI,k}\right)\right)}{s_k\sqrt{2}}\right)\right] \tag{2.44}$$

$$C_2 = \sum_k \left(\frac{F_{HO}\, f_k}{2}\right) \left[1 + \text{erf}\left(\frac{\ln\left(r_{C,HO} - \ln\left(r_{HO,k}\right)\right)}{s_k\sqrt{2}}\right)\right] \tag{2.45}$$

$$C_3 = \sum_k \frac{F_{HI}\, f_{k,HI}}{r_{k,HI}} \exp\left(\frac{s_{k,HI}^2}{2}\right) \left[1 - \text{erf}\left(\frac{\ln\left(r_{C,HI}\right) - \ln\left(r_{k,HI}\right)}{s_{k,HI}\sqrt{2}} + \frac{s_{k,HI}}{\sqrt{2}}\right)\right] \tag{2.46}$$

$$C_4 = \sum_k \frac{F_{HO}\, f_{k,HO}}{r_{k,HO}} \exp\left(\frac{s_{k,HO}^2}{2}\right) \left[1 + \text{erf}\left(\frac{\ln\left(r_{C,HO}\right) - \ln\left(r_{k,HO}\right)}{s_{k,HO}\sqrt{2}} + \frac{s_{k,HO}}{\sqrt{2}}\right)\right] \tag{2.47}$$

In porous layers with the smallest pore size range of 10 to 100 nm, such as CLs and MPLs, the Knudsen number increases from approximately 1 to 10. The Knudsen number is a dimensionless number for characterizing the dominant diffusion phenomena and gas flow in porous layers. Both binary and Knudsen diffusion become significant for the analysis of porous layers with small pore sizes and enhanced Knudsen numbers. Given the characteristics given in Table 2.4, the transport properties are evaluated for a representative GDL as shown in 2.2 using the mixed wettability PSD model described in this section.

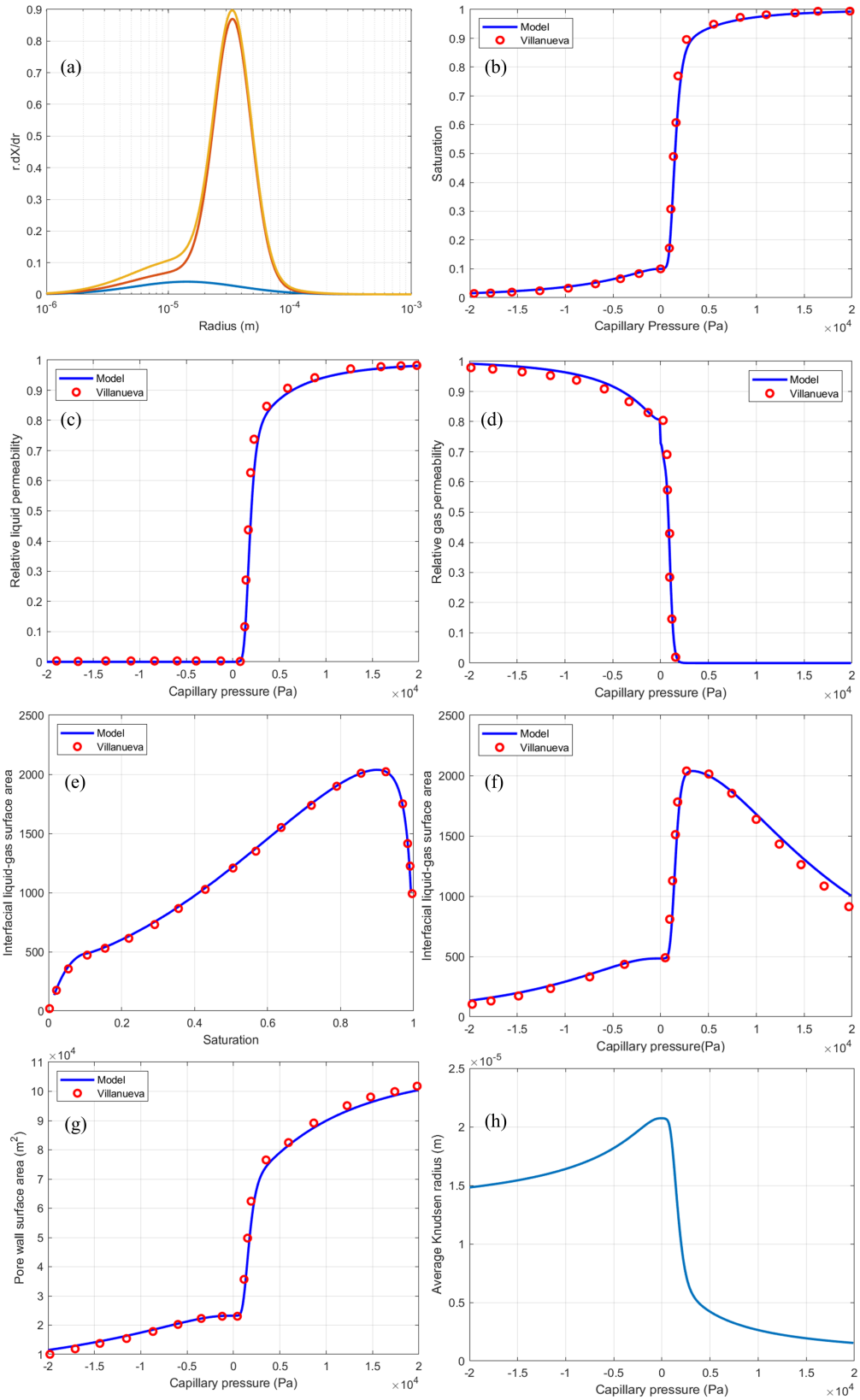

Figure 2.2: PSD characteristics for GDL-Sigracet 34BA compared to results of Ref. [87] (a) Pore volume fractions, (b) Water retention curve, (c) Liquid relative permeability, (d) Gas relative permeability, (e) Interfacial surface area against saturation and (f) capillary pressure, (g) pore wall surface area, and (h) Knudsen radii

2.2.4 Electrochemical Kinetic Model

The complexity of the cathode catalyst layer (CCL) in PEMFCs introduces challenges in modeling mass transfer and electrochemical reactions. Various processes including transport, electrochemical reactions, and fluid flow, occur concurrently, each at different geometric scales, complicating the modeling approaches. Therefore, various physical and mesoscopic models are reported for considering the effects of CL microstructural properties on transport resistances through the ionomer layer, at ionomer-gas and ionomer-Pt interfaces [51][92]. While volume-averaged approaches are popular for microscale models [24], the CL is assumed as a thin layer in the interface approach used in large-scale models [93].

The advanced imaging techniques provide insights regarding the shape of the CLs, causing the development of agglomerate models. These images prove the aggregation of carbon and platinum at the nanoscale within the electrolyte in the CCL, and the agglomerate approach assumes the aggregation of CL particles [94][95]. In addition, modeling of the interior structure of agglomerates is performed with different approaches. For instance, Sun et al. [96] argued that the agglomerates are covered by an ionomer layer and evaluated the transport of electrons, ions, and reactants considering both oxygen diffusion rate and ionomer transport resistances. The factual structure of the agglomerates is thus not obvious, and it is considered to either be electrolyte spheres filled with Pt and carbon particles [97] or void spheres of Pt and carbon particles filled with produced water during the reaction [98]. To validate the agglomerate models with experimental studies, a wide range of 200-2000 nm is applied for agglomerate sizes while the ionomer thickness varies from 10 to 100 nm [38]. From an experimental point of view, such variations have not been verified by microscopy techniques [99], and the agglomerate size is reported not to exceed 300 nm [99][94]. Thus, some researchers continue to utilize an agglomerate approach with small agglomerate sizes. Mashio et al. [81] used the agglomerate size of 40 nm and reported that the agglomerate approach is incapable of reproducing experimental results using such a small agglomerate radius.

Various ongoing studies are conducted to distinguish between the sources of interfacial resistance. Liu et al. [100] explored the existence of ionomer-gas interfacial resistance by depositing Nafion® on top of a porous substrate where pores mimic the Pt

particles. By measuring the thickness-dependent resistance, the authors concluded that there is no interfacial resistance at the ionomer-gas interface [100]. Jinnouchi et al. [101] revealed that transport resistances are dominated by oxygen permeation at the ionomer-Pt interface using a molecular dynamics model. As evidenced by Nonoyama et al. [102], the use of high relative humidity causes flooding and blockage of pores, and it is regarded as an additional resistance. In a recent development by Hao et al. [38], a CL model has been introduced taking into account interfacial resistances associated with Pt particles and the ionomer film, as well as the diffusion resistance of oxygen within the ionomer while assuming the produced water to be in vapor phase only. While the source of increased oxygen transport resistances is commonly attributed to the thin-film properties of the ionomer, such as water uptake [97], ionic conductivity [103], and oxygen permeability [104], some researchers mentioned other sources such as higher flooding levels in CL and GDL, owing to reduced vaporization capability [99]. Moreover, the transport resistances are not only dependent on the Pt loading but also on the cathode structural characteristics [5].

The oxygen transport process from pores to reaction sites comprises dissolution and diffusion through water film, dissolution, and permeation in ionomer thin film, adsorption at the surface of Pt-ionomer, and the chemical reaction at ionomer-Pt-carbon surfaces as represented in Figure 2.1. An additional resistance for the transport of protons through the ionomer thin film, which is on the order of 10s of nanometers, needs to be considered since just a fragment of ionomer-Pt-carbon surfaces serves as reaction active sites. As a result, recent studies focused either on measuring experimentally the protonic conduction resistance proved to cause high voltage losses [105][106] or including it through modeling studies based on experimental estimations [92].

In this study, the reaction kinetic model developed by Ref. [38] capturing the local transport resistances, is further extended to include the proton conduction resistance [77], for which the electrochemical model parameters are provided in Table 2.5. Since the effect of local transport resistances is minimal in the anode, the detailed reaction kinetic equations are only considered in the cathode [77].

Table 2.5: Parameters of electrochemical model [38]

Parameter	**Value**	**Unit**
$i_{0,an}^{ref}$	0.3	A/cm ^{2}
E_{an}	10	kJ/mol
$C_{H_2,ref}$	4 e^{-5}	mol/cm^3
γ_{an}	0.5	—
α_{an}	2	—
$i_{0,ca}^{ref}$	4 e^{-5}	A/cm ^{2}
E_{ca}	67	kJ/mol
$C_{O_2,ref}$	4 e^{-5}	mol/cm^3
γ_{ca}	0.7	—
α_{ca}	0.5	—

Total local transport resistances are calculated as [38],

$$R = R_{w,int} + \frac{\delta_w}{D_{O_2,w}} + R_{ion,int} + \frac{\delta_{ion}}{D_{O_2,ion}} + R_{Pt,int} \tag{2.48}$$

where the first, third, and last terms describe the interfacial resistances at the surface of water film, ionomer thin film, and Pt surfaces while the second and fourth terms represent the diffusion of oxygen through water and ionomer films. In addition, interfacial resistances are proportionally related to diffusional resistances due to the lack of experimentally measured interfacial resistances at different surfaces [38].

$$R_{w,int} = k_3 \frac{\delta_w}{D_{O_2,w}} \tag{2.49}$$

$$R_{ion,int} = k_1 \frac{\delta_{ion}}{D_{O_2,ion}} \tag{2.50}$$

$$R_{Pt,int} = k_2 \frac{\delta_{ion}}{D_{O_2,ion}} \tag{2.51}$$

where, k_1, k_2, and k_3 are proportionality factors with values of 8.5, 5.4, and 0 [38] for the simulation case studies. However, the values of these factors are provided for model validation against different experimental data. The oxygen concentration on the surface of Pt

particles is derived from its level in pores considering the total local transport resistances [38],

$$i_{ca}\left(C_{O_2}^{Pt}\right)^{\gamma_{ca}} + \frac{4F}{R_T}\left(C_{O_2}^{Pt} - C_{O_2}^{g}\right) = 0 \tag{2.52}$$

In equation 2.52, γ_{ca} is the cathodic reaction order, R_T is the oxygen transport resistance defined as $R_T = \dfrac{R}{a_c\, x}$ which accounts for the effective specific surface area of the covered ionomer on active Pt/C particles, and i_{ca} is the kinetic equation defined as [38],

$$i_{ca} = i_{0,ca}\, a_{Pt}\, (1-\theta_{Pt}) \left(\frac{1}{C_{O_2}}\right)^{\gamma_{ca}} \exp\left(\frac{-F\,\alpha_{ca}\,\eta_{ca}}{RT} - \frac{w\,\theta_{PtO}}{RT}\right) \tag{2.53}$$

In equation 2.53, $i_{0,ca}$, a_{Pt}, α_{ca}, η_{ca}, and w are the cathode exchange current density, the active volumetric surface area of Pt particles, cathodic charge transport coefficient, cathodic overpotential, and Temkin energy parameter with the value of 3 kJ/mol [38] respectively. In addition, θ_{PtO} is the Pt-oxide coverage for which a sigmoidal function is used to account for its dependence on the cell potential [107].

The cell potential V_{cell} is calculated from the subtraction of cathode and anode overpotentials, η_{ca}, η_{an}, ionic potential drops through ionomer and electrolyte, ΔV_{CL}, ΔV_{mem}, and ohmic potential drop ΔV_{ohm} from the reversible potential V_{rev} to the ground anode electrode [50].

$$V_{cell} = V_{rev} - \eta_{ca} - \eta_{an} - \Delta V_{mem} - \Delta V_{CL} - \Delta V_{ohm} \tag{2.54}$$

where the ionic potential drop is calculated as follows [77],

$$\Delta V_{CL} = R_{ion,CL}\, j_{cell}\, \delta_{CL} \tag{2.55}$$

where $R_{ion,CL}$ is the resistance associated with the proton conductance through the CL and it is fitted from experiments of Ref. [105]. Moreover, y_{bare} is the mass fraction of bare carbon particles incorporated to dilute the Pt particles in the carbon substrate experimentally [5]. The anode activation overpotential is calculated as [10],

$$i_{an} = i_{0,an}\, a_{Pt} \left(\frac{C_{H_2}}{C_{H_2}^{ref}}\right)^{\gamma_{an}} \exp\left(\frac{F\,\alpha_{an}\eta_{an}}{RT}\right) \tag{2.56}$$

where $i_{0,an}$, α_{an} are the anode exchange current density and anode charge transfer coef-

ficient. The remaining important CL electrochemical variables are provided in Table 2.6. Moreover, a comprehensive sensitivity analysis of the presented electrochemical model is conducted previously emphasizing the importance of each factor's significance [108]. The authors evaluated the dependencies of the parameters and the sensitivity of the output predictions namely voltage, high-frequency resistance, and membrane crossover [108].

Table 2.6: Variables of electrochemical model

Description	Equation	
Water film thickness [10]	$\delta_w = \left[S_{CL}\, \varepsilon_{CL} \left(\frac{r_C^3}{\varepsilon_C} \right) + (r_C + \delta_{ion})^3 \right]^{\frac{1}{3}} - r_C - \delta_{ion}$	(2.57)
Ionomer film thickness [38]	$\delta_{ion} = r_C \left[\left(\frac{\varepsilon_{ion}}{\varepsilon_C} + 1 \right)^{\frac{1}{3}} - 1 \right]$	(2.58)
Oxygen permeability in ionomer [109]	$p_{O_2}^{ion} = p_{dry}\, \exp\left(\frac{-E_{dry}}{RT} \right) + f_v\, p_{wet} \exp\left(\frac{-E_{wet}}{RT} \right)$	(2.59)
Oxygen diffusivity in water [50]	$D_{O_2}^{w} = 1.98 \times 10^{-9} \left(\frac{\mu_l(293)}{\mu_l(T)} \right) \frac{T}{298}$	(2.60)
Volumetric surface area of ionomer [38]	$a_C = \frac{3\varepsilon_C}{r_C^3} (r_C + \delta_{ion})^2$	(2.61)
Active volumetric surface area of Pt particles [38]	$a_{pt} = \frac{a_{ECSA}\, L_{Pt}}{\delta_{CL}}$	(2.62)
Number fraction of total catalyst particles [38]	$x = \frac{(1 - wt\%)\,(1 - y_{bare})}{(1 - wt\%\,(1 - y_{bare}))}$	(2.63)
Volume fraction of Pt [38]	$\varepsilon_{Pt} = \frac{1}{\rho_{Pt}} \frac{L_{Pt}}{\delta_{CL}}$	(2.64)
Volume fraction of carbon [38]	$\varepsilon_C = \frac{(1 - wt\%)\, \varepsilon_{Pt} \rho_{Pt}}{\rho_C\, wt\%\, (1 - y_{bare})}$	(2.65)
Volume fraction of carbon [38]	$\varepsilon_{ion} = (I/C)\, \varepsilon_C\, \frac{\rho_C}{\rho_{ion}} \left(1 + \frac{M_w\, \rho_{ion}}{\rho_w\, EW}\, \lambda \right)$	(2.66)
Exchange current density of cathode/anode [38]	$i_{o,ca} = i_{0,ca/an}^{ref} \exp\left(\frac{-E_{ca/an}}{R} \left(\frac{1}{T} - \frac{1}{353.15} \right) \right)$	(2.67)
Pt-oxide coverage [107]	$\theta_{PtO} = \left[1 + e^{22.4(0.818 - V_{cell})} \right]^{-1}$	(2.68)
Modified ionomer resistance in the CL, based on [77], [105]	$R_{ion,CL} = \frac{\tau\, (1 - y_{bare})^{-0.25}}{\kappa_{(T,RH)}\, \varepsilon_{CL}}$	(2.69)
Proton conductance in ionomer [105]	$\kappa_{(T,RH)} = 22 \exp\left(\frac{-E_k}{R} \left(\frac{1}{T} - \frac{1}{353.15} \right) \right) \left(\frac{a_w^{an} + a_w^{ca}}{2} \right)^{2.24}$	(2.70)

2.2.5 Boundary Conditions

A contact velocity based on the stoichiometric ratio is defined at the channel inlets, considering the reference current density as 10^4 A/cm^2 [50],

$$u_{in}^{an} = st_{an}\frac{RT_0}{P_0}\frac{10^4}{2F}\frac{1}{h_{CH}w_{CH}} \tag{2.71}$$

$$u_{in}^{ca} = st_{ca}\frac{RT_0}{P_0}\frac{10^4}{4F}\frac{1}{h_{CH}w_{CH}}\frac{1}{0.21} \tag{2.72}$$

where the fraction 0.21 is the molar ratio of oxygen in the inlet air. The inlet gases are air containing oxygen, nitrogen, and water vapor from the cathode side as well as hydrogen, nitrogen, and water vapor from the anode side. The mass fraction of species at the inlets is obtained considering the operating relative humidity [50]. Moreover, the outflow boundary condition is used for all the physics at the channel outlets, while the no-slip boundary condition is defined for the walls of the computational domain.

2.2.6 Numerical Implementation

The numerical model is implemented in the commercial finite element software COMSOL Multiphysics 6.0. All the equations described in 2.1 including Brinkamn, Maxwell-Stefan, Butler-Volmer, liquid water, dissolved water, and energy conservation are coupled and solved numerically. The mesh distribution is shown in Figure 2.1, consisting of a mapped mesh with 720 quadrangular linear elements and around 21K degrees of freedom (DOF). The resulting coupled equations are solved using a fully coupled solver with Newton iterations for nonlinear and direct PARDISO (parallel sparse direct solver) for the linear system of equations. The simulations were run on a workstation with a 3.6 GHz quad-core processor and 32 GB RAM.

2.2.7 Model Validation

The present model is validated with novel electrode compositions of Ref. [5]. The authors investigated transport limitations at Pt surfaces with fixed electrode thickness and bulk properties for 6 different loadings and CL compositions [5]. In addition, authors studied the impact of Pt dispersion by varying weight percentages wt.% in Pt/C particles and diluting CLs with bare carbon to increase the distance between Pt particles [5]. Moreover, the same I/C ratio, with the value of 0.95, material, and fabrication process is used for all the CLs ensuring the same porosities and bulk properties for all the compositions [5]. The CL compositions and Pt-loadings adopted from Ref. [5], are reported in Table 2.7, while the values proportionality factors of k_1, k_2, k_3 are chosen to be 8.5, 5.4, and 0.

Table 2.7: The CL parameters and components used for the model validation [5]

Pt loading (mg/cm^2)	**Dilution**	**Catalyst type**	**Dilution ratio (y_{Bare})**
0.1	NO	15% Pt/C;0.71-30% Pt/C;0.29	0
0.05	NO	10% Pt/C;1	0
0.025	NO	5% Pt/C;1	0
0.1	YES	50% Pt/C;0.42	0.58
0.05	YES	50% Pt/C;0.22	0.78
0.025	YES	50% Pt/C;0.11	0.89

A comparison of simulated polarization curves with the experimental results is shown in Figure 2.3. For all simulation case studies, air is used as the inlet gas in the cathode with a high stoichiometric flow ratio. In addition, the geometrical, material, and composition parameters are adopted from the experiments [5]. To investigate the source of increased resistances at low Pt-loadings, Owejan et al. [5] compared the polarization curves for the relative humidity of 1 and 0.65. Consistently with the former, the validated results are obtained for operating conditions of 80°C, 150 kPa, and relative humidity of 1 and 0.65.

Simulation results show remarkable agreement with the reported experimental data for 6 different cathode compositions and two different operating conditions. As depicted in Figure 2.3, reduced Pt-loading results in high transport resistance and a drop in oxygen concentration deteriorating the cell performance. Moreover, the authors analyzed the cell performance by diluting various wt.% of Pt/C particles with bare carbon particles. The dispersed Pt/C particles in diluted catalysts exhibited higher resistances due to higher

tortuosity which increases the reactant fluxes near each Pt/C particle. At low relative humidity, the deviation between the performance of diluted and non-diluted CLs increases, indicating the significance of low proton conductance in the ionomer at the CL for drier operating conditions.

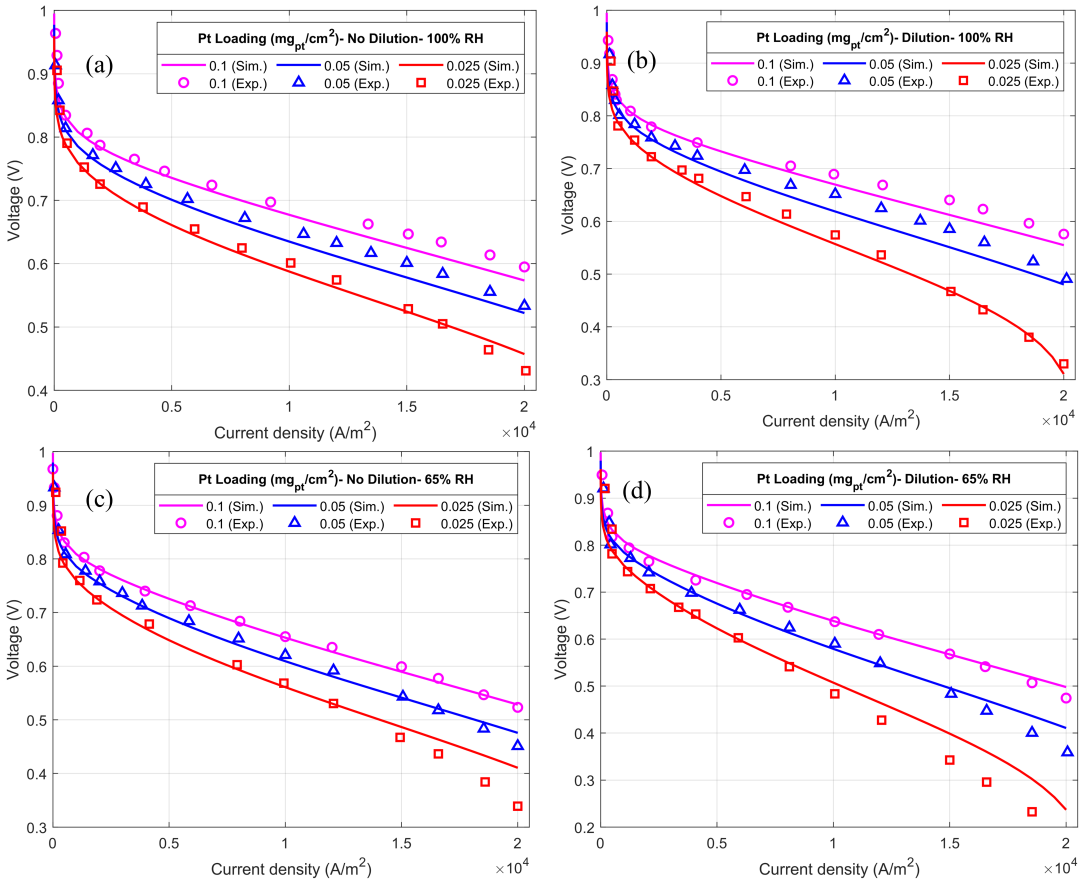

Figure 2.3: The comparison of simulated results and experimental data from Ref. [5], (a) non-diluted and (b) diluted catalysts under 100% relative humidity, (c) non-diluted and (d) diluted catalyst under 65% relative humidity

To ensure the accuracy of the model in capturing the I/C ratio effect, the results of the P3D model are further validated with experiments of Ref. [27], in which authors investigated the effect of different ionomer content in cathode and anode electrodes keeping all the other CL microstructural properties constant. The experimental data is obtained under atmospheric conditions using a temperature of 80°C, and ambient pressure with stoichiometric ratios of 1.5 for the cathode, and 2 for the anode with relative humidity conditions of 0.59 and 0.82 [27], respectively. Moreover, the values of factors k_1, k_2, k_3 in equation 2.46 are selected as 27, 20, 0. Consistent with the properties reported by Kim et al. [27], the radius of carbon particles is adjusted to 55 nm while the ECSA is 45 m^2/g.

The comparison of the model results with experimental data is shown in Figure 2.4.

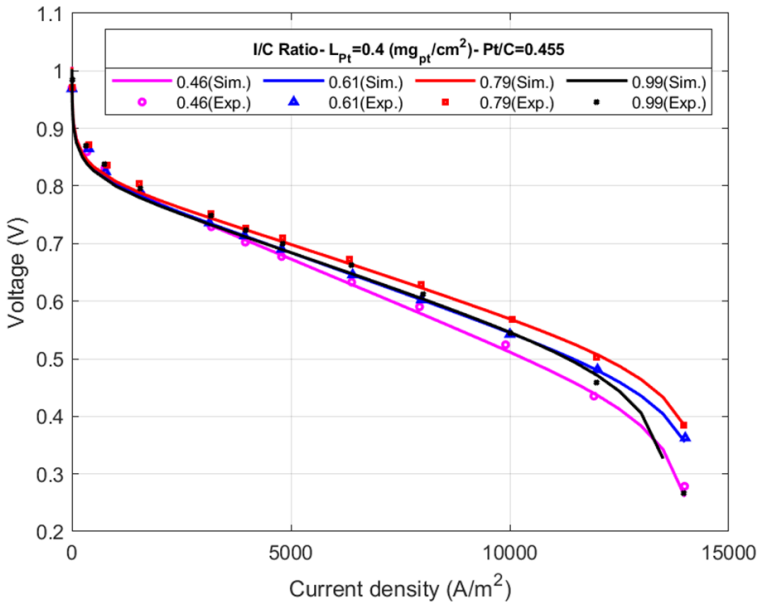

Figure 2.4: The comparison of the model results with the experimental data obtained from Kim et al. [27]

Kim et al. [27] reported severe concentration overpotential and lower electrochemical activity for lower ionomer contents [27]. The model results represent reasonable agreement with the provided experimental data, for which the best performance is related to the 0.79 I/C ratio. It is worth mentioning that cell performance for different I/C ratios is influenced by various microstructural properties including interfacial resistances, ionomer network resistances, and mass transport through pores [27].

2.3 Simulation Case Studies

The present model is applied to comprehensively investigate the combined effects of the Pt-loading, Pt/C ratio, i.e., the weight ratio of platinum on Pt/C particles, bare carbon mass fractions (y_{bare}), and the I/C ratio, i.e., the weight ratio of the ionomer concerning the total carbon in the CL. The oxygen transport resistances and ionomer potential losses are studied for these compositions to investigate the causes of the reduced cell performance for low Pt-loaded CLs. Furthermore, the effects of relative humidity on the ohmic loss associated with CL ionomer proton conduction are investigated. Since the geomet-

rical considerations are extremely important for studying the mass, heat transport, and reactant distribution through the cell, the effects of different channel-to-rib width ratios (CRWRs) are investigated for low Pt-loaded CLs. The base parameters for all the studies are the Pt and carbon particle size of 2 and 25 nm unless otherwise stated. It should be mentioned that CL structural characteristics covered in this work are reported as independent parameters in the sensitivity and collinearity study of Goshtasbi et al. [108] while authors incorporated the electrochemical model developed by Ref. [38].

2.3.1 Catalyst Layer Characteristics

2.3.1.1 Effects of Pt Loading

Varying Pt loading and Pt/C Ratio: Pt-loading is varied between 0.2 to 0.05 mg/cm^2 in the cathode CL. Due to the sluggishness of the oxygen reduction reaction (ORR), the rate of ORR dominates the cell performance. Pore volume in the catalyst layer has a very strong effect on the catalyst performance and masks the effects of the CL composition. Therefore, to compare the cell performance under similar conditions but different compositions, the porosity of the CL is kept constant. Although the volume fraction of Pt varies slightly, the carbon and ionomer volume fractions are the same and the overall CL porosity is around 0.57 for all cases. The polarization and power density curves obtained for this case are depicted in Figure 2.5.

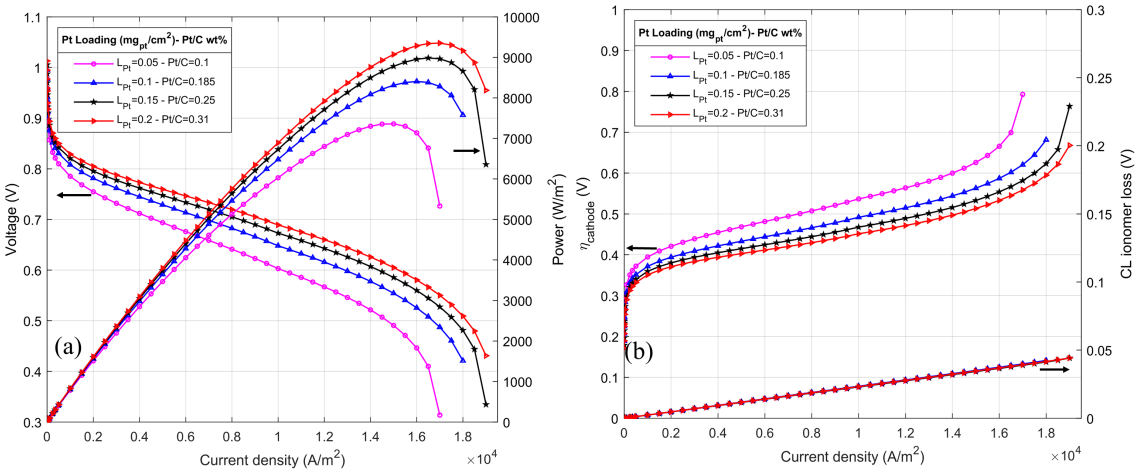

Figure 2.5: (a) Polarization and power density curves, (b) Cathode overpotential and CL ionomer loss for various Pt-loadings and Pt/C ratios

The cell performance is significantly decreased for lower Pt-loadings due to the reduced cathodic reaction rate, caused by higher transport resistances near Pt particles rather than oxygen diffusion resistance through pores. In addition, the increasing rate of the cell performance weakens gradually meaning that the peak power densities are nearly related for Pt-loadings of 0.15 and 0.2 mg/cm^2. Moreover, the cathodic activation and ionomer resistances for the four cases are shown in Figure 2.5b. Considering consistent ionomer volume fraction and coverage for all the compositions, the ionomer resistance in CL is closely fixed for various Pt-loadings. However, the cathodic overpotential is increased for low Pt-loadings showing the dominant effect of oxygen transport resistances for all current densities. At high current densities, 1.4-1.8×10^2 A/m^2, in addition, the electrochemical reaction is severely affected by the oxygen deficiency for low Pt-loaded CLs.

To further elucidate the cause of decreased cell performance, the oxygen transport resistance for different Pt-loadings is shown in Figure 2.6a. This resistance sharply decreases from 22 to 11 s/m between Pt-loadings of 0.05 and 0.1 mg/cm^2 while the rate of decrease is smaller for higher Pt-loadings. The increased resistance is mainly caused by higher interfacial resistance at the surface of Pt particles $R_{Pt,int}$ since this resistance is inversely proportional to the active volumetric surface area of Pt particles, a_{Pt}. Moreover, the direct dependency of oxygen transport resistance and Pt-loading is the reason for the cathodic activation potential variations shown in Figure 2.6. It should be noted that the constant CL thickness is assumed in this study which provides constant ohmic

overpotential for all the cases.

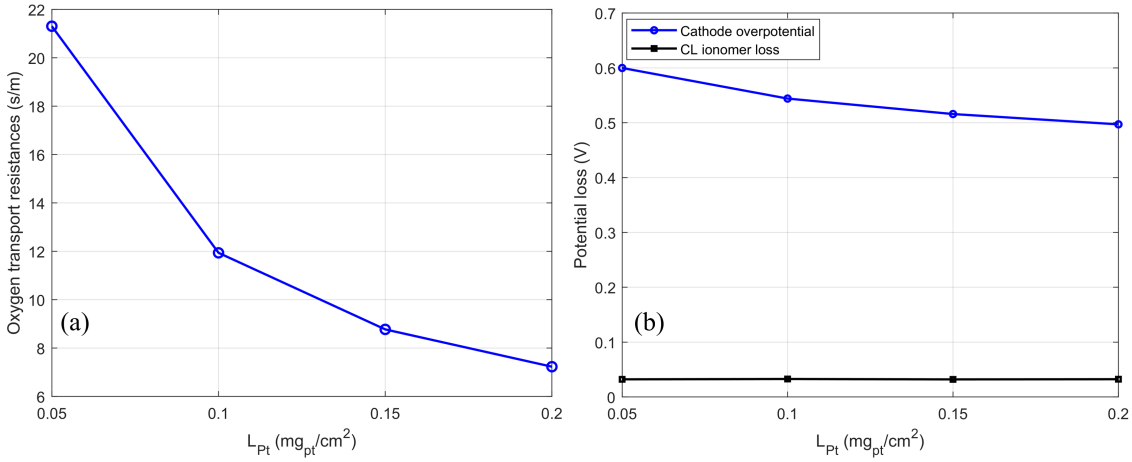

Figure 2.6: (a) The oxygen transport resistance, (b) The cathodic overpotential and CL ionomer resistance at $J_{load} = 1.4 \times 10^4$ A/m^2 against different Pt-loadings and Pt/C ratios

Varying Pt loading and CL Thickness: To provide higher Pt-loadings with a constant Pt/C ratio, however, the CL thickness needs to be increased as demonstrated by He et al. [51]. In this case, there will be a trade-off between oxygen transport resistances, which affect concentration and activation overpotentials, with the ohmic overpotentials for high Pt-loadings [51][110]. Assuming the consistent CL fabrication method, a constant CL porosity is considered for different cases with different Pt-loadings and CL thicknesses. The polarization and power density curves obtained for this case are depicted in Figure 2.7a.

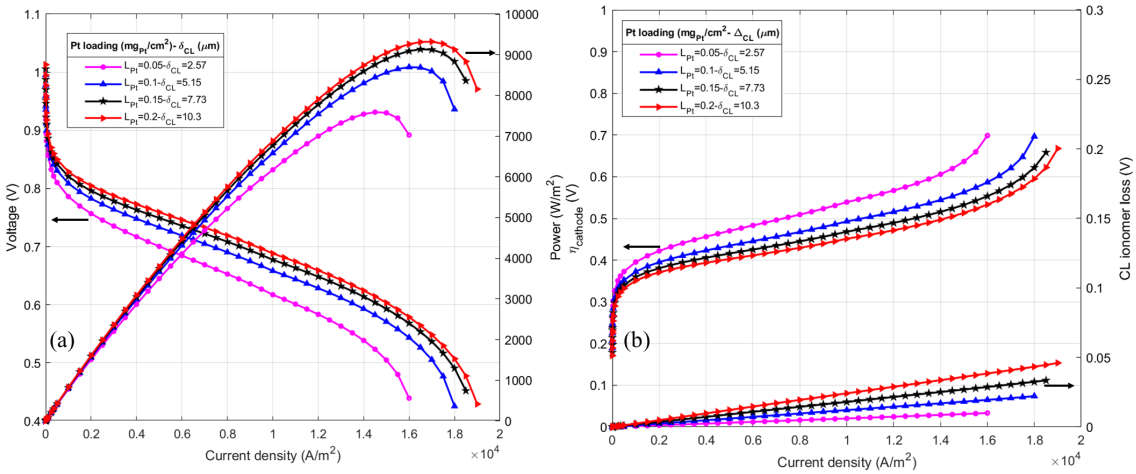

Figure 2.7: (a) Polarization and power density curves, (b) Cathode overpotential and CL ionomer loss for various Pt-loadings and CL thicknesses

The cell performance is significantly decreased for lower Pt-loadings same as in the previous section. Comparing the results obtained for the same Pt-loading of 0.05 mg/cm^2, however, the peak power densities of 7360 and 7590 W/m^2 are obtained varying the Pt/C ratio and CL thickness, respectively. Since in the previous study, the constant CL thickness was assumed for different Pt-loadings, higher CL thickness is considered to cause elevated resistances for the transport of ions and electrons. Moreover, peak power densities of 9322 and 9353 W/m^2 are obtained for the Pt-loading of 0.2 mg/cm^2, comparing the results in Figures 2.5 and 2.7. Considering constant CL thickness reduces the performance of low Pt-loaded cells, however, it increases the cell performance for high Pt-loadings mainly due to suppressing the additional resistances. Notably, the cell performance for Pt-loadings of 0.2 and 0.15 mg/cm^2 are closely related with values of 9322 and 9125 W/m^2, respectively. The cathodic activation and ionomer resistances for the four cases are shown in Figure 2.7b. Although consistent ionomer volume fraction is used for all simulation case studies, the CL ionomer resistance is slightly increased for thicker CLs due to the proportional relationship between the ionomer potential loss and CL thickness through equation 2.53, while the same overpotential values are observed due to the same Pt-loadings varying Pt/C ratio or CL thickness.

The oxygen transport resistance for different Pt-loadings and CL thicknesses is shown in Figure 2.8. The oxygen transport resistance decreases from 26 to 13 s/m between Pt-loadings of 0.05 and 0.1 mg/cm^2, while it changed from 21 to 12 s/m for varying the Pt-loading and Pt/C ratio. Since the cathodic overpotential represents the same values in Figures 2.6 and 2.8, the only difference is the ionomer potential loss which is directly proportional to the CL thickness [38]. The reason behind the enhanced performance for low Pt-loadings is the reduced ionomer potential loss as evidenced in Figure 2.8b.

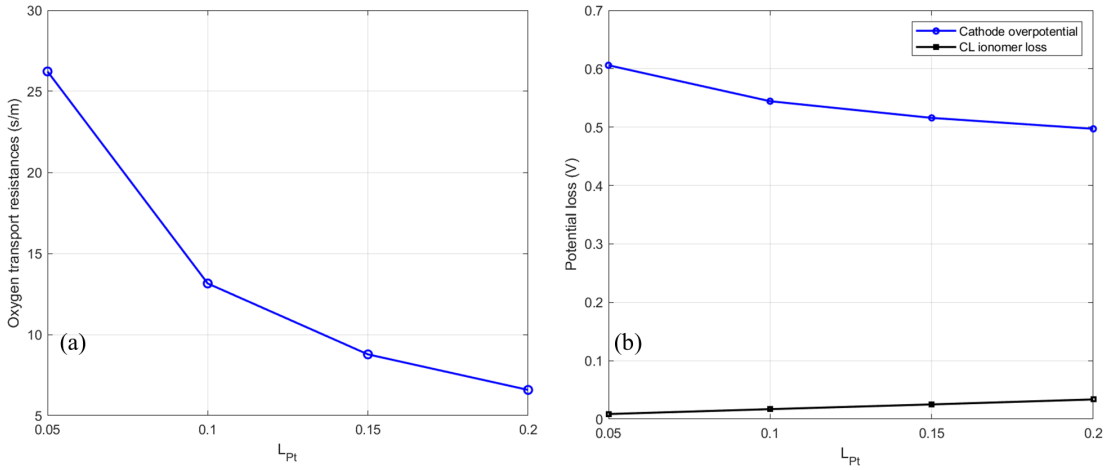

Figure 2.8: (a) The oxygen transport resistance, (b) The cathodic overpotential and CL ionomer resistance at $J_{load} = 1.4 \times 10^4$ A/m^2 against different Pt-loadings and CL thicknesses

2.3.1.2 Effects of Dilution Ratio

The relative contribution of local and interfacial transport resistances highly depends on the Pt dispersion, utilization, and electrochemically active surface area, a_{ECSA}, all of which are directly related to the mass fraction of bare carbon particles. To study the effect of platinum dispersion on the cell performance, overall carbon volume fraction and CL porosity are kept constant by simultaneously varying Pt/C ratios and bare carbon mass fractions. Higher Pt/C weight percentages with constant Pt-loading provide lower carbon loading in the CL while more bare carbon particles are added to fix the carbon volume fraction. The oxygen flux near each active Pt site as well as the microscale CL structure are changing through this analysis mode. The polarization and power density curves for this analysis using Pt-loading and I/C ratio of 0.05 mg$_{Pt}$/cm^2 and 0.75 are shown in Figure 2.9 together with the cathodic overpotential and ionomer potential loss.

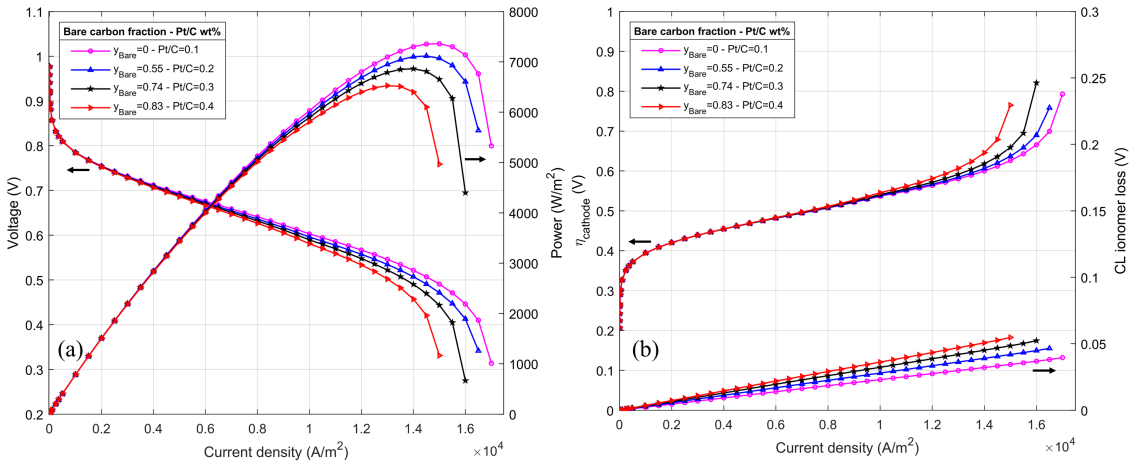

Figure 2.9: (a) Polarization and power density curves, (b) Cathode overpotential and CL ionomer loss using various Pt/C ratios and bare carbon mass fractions

As the dilution rate increases, the portion of the catalyzed carbon particles and Pt dispersity decreases as demonstrated in Figure 2.1. The effect of Pt dispersity was recently investigated through an experimental study where the authors demonstrated that the low dispersed CLs represent higher performance due to the smaller thickness and better water management [111]. However, in this study, we kept the thickness and the porosity of the CL constant.

From Figure 2.9, the best cell performance is related to the non-dilution case in which no bare carbon particles are introduced into the CL, and increasing bare carbon mass fraction deteriorates the cell performance, especially at mass fractions higher than 0.55. At low current densities, the variations in cathodic overpotential are negligible, as shown in Figure 2.9b, providing consistent cell performance in this region for all the studied cases. However, increased cathodic overpotential and ionomer potential loss for high current densities result in deviations in limiting current densities. Since the ionomer thickness and the volume fraction remain constant in the CL, higher ionomer resistance in Figure 2.9 for diluted CLs is related to the increased ionomer effective tortuosity (equation 34) caused by the addition of bare carbon particles. Moreover, the CL ionomer loss and cathodic overpotential against different bare carbon mass fractions for the four cases are shown in Figure 2.10.

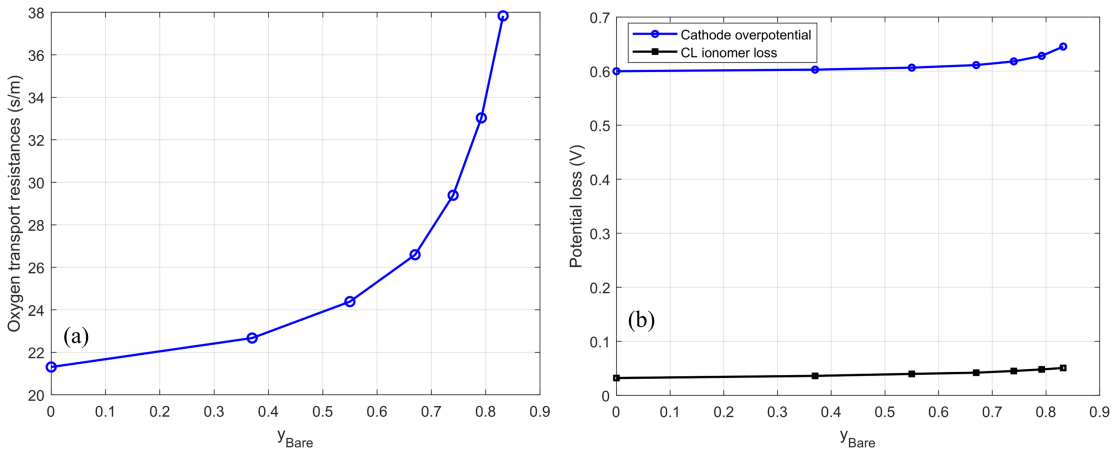

Figure 2.10: The oxygen transport resistance, (b) The cathodic overpotential and CL ionomer potential loss at $J_{load} = 1.4 \times 10^4$ A/m^2 for various bare carbon mass fractions

The addition of bare carbon particles to the CL causes higher oxygen transport resistances adjacent to Pt particles due to the reduction of catalyzed carbon particles in the CL. As a result, the effect of bare carbon addition on the oxygen transport resistance is highly nonlinear, showing a 14% increase between bare carbon ratios of 0 and 0.55, and 72% between 0 and 0.83. Therefore, elevated cathodic activation potentials and decreasing limiting current densities are observed for very high carbon mass fractions $y_{Bare} \geq 0.7$. Moreover, the CL ionomer resistance increases with the bare carbon mass fraction as well, but more linearly than the oxygen transport resistance; the ionomer resistance is increased by 23% between bare carbon mass fractions of 0 and 0.55 and 57% between 0 and 0.83. The higher ionomer potential loss in diluted CLs emanates from the increased ionomer flux and effective tortuosity, suggesting that the ionomer creates a well-percolated proton conduction network with higher transport resistances upon the addition of bare carbon particles.

2.3.1.3 Effects of Ionomer Content

Varying Bare Carbon Mass Fraction (y_{Bare}) and I/C Ratio: The presence and loading of the ionomer in the CL play a critical role in its performance. The ionomer acts as a proton-conducting medium, facilitating the movement of protons throughout the CL. This is essential for ensuring the transport of protons through the CL, thus expanding the num-

ber of electrochemically active sites available for electrochemical reactions. Moreover, the ionomer serves as a binding material, enhancing the mechanical stability of the CL, which helps hold the various components together and provides structural integrity to the CL. Additionally, the hydrophilic agents in the ionomer contribute to keeping the membrane hydrated, which is vital for maintaining the proper functioning of the fuel cell. On the other hand, excessive ionomer loading leads to a reduction in the pore volume available for gas transport within the CL. This reduction can be exacerbated by the flooding of hydrophilic pores, which hinders the movement of reactants and products within the CL [27][112]. Therefore, there is an optimal value for ionomer content within the CL, which is significantly affected by various factors, including the Pt/C ratio, carbon particle size, the thickness of the CL, the choice of solvent for the CL ink, and the operating conditions [27]. Finding the right balance for ionomer content is crucial for achieving optimal fuel cell performance, and it involves careful consideration of these fabrication parameters and operating conditions.

Here, the effects of ionomer content on the cell performance and power density are studied using I/C ratios ranging from 0.22 to 0.75. We keep the CL porosity constant to eliminate the effects of the pore volume variations by adjusting the carbon volume fraction either by increasing the bare carbon mass fraction as studied in this section or by boosting the Pt/C ratio provided in the next section. For the first case, the carbon volume fraction is modified by the addition of bare carbon particles using a constant Pt/C ratio of 0.1. The polarization and power density curves obtained for this analysis mode are depicted in Figure 2.11a.

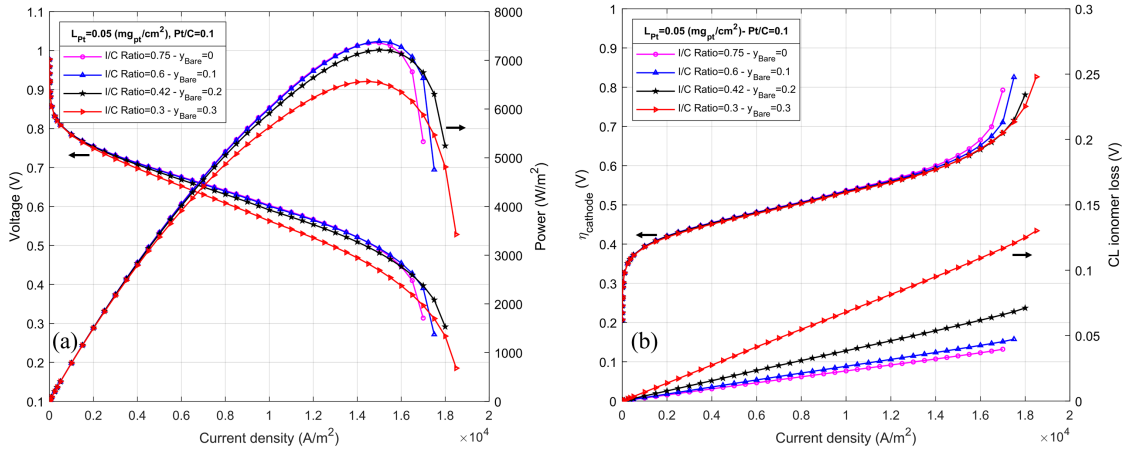

Figure 2.11: (a) Polarization and power density curves, (b) Cathode overpotential and CL ionomer loss for various I/C ratios and bare carbon mass fractions

Decreasing ionomer content in the CL hinders proton conduction by reducing the ion conductive passages, although enhances the oxygen diffusivity. From Figure 2.11a, decreasing the I/C ratio from 0.75 to 0.6 has a slight effect on the cell performance and power density keeping the CL porosity constant, in which the obtained peak power densities are 7360 and 7391 W/m^2, respectively. Further decreasing the ionomer content, however, deteriorates the cell performance for I/C ratios of 0.42 and 0.3. The cathodic overpotential and CL ionomer loss are also shown in Figure 2.11b. Although constant cathodic overpotential is obtained for various I/C ratios at low current densities, the CL ionomer potential loss is dramatically increased for small I/C ratios. It should be noted that the addition of bare carbon particles also modifies the ionomer resistance, but its effect is negligible in comparison to the I/C ratio. At high current densities, in addition, the cathodic overpotential is smaller for small I/C ratios providing higher limiting current densities. In this regard, Kim et al. [27] experimentally discovered lower electrochemical activity for lower ionomer content caused by high ionic resistance and severe concentration overpotentials for higher cathodic ionomer content, which is caused by various factors including the mass transport through pores, catalyst-ionomer interfacial area, and the ionomer resistance.

The oxygen transport resistance together with ionomer thickness, and the cathodic overpotential against various I/C ratios are shown in Figure 2.12. The ionomer thickness is increased using higher I/C ratios causing elevated diffusional transport resistance through the ionomer as well as increased interfacial resistances at the surface of Pt parti-

cles since the interfacial resistance scales up with the ionomer thickness [38]. The oxygen transport resistances increase from 10 to 21 s/m in Figure 2.12a, however, insignificant changes in cathodic overpotentials are observed given the small values of these resistances. The ionomer loss variations are sharper for small I/C ratios while it flattens for higher values causing an I/C ratio of 0.6 with y_{Bare} of 0.1 to represent the best cell performance over studied values. It should be mentioned that the variation of the cathodic activation potential loss is a deterministic parameter for evaluating cell performance using various Pt-loadings and Pt/C ratios, and the key factor affecting cell performance using different I/C ratios is the ionomer potential loss and its proton conductance.

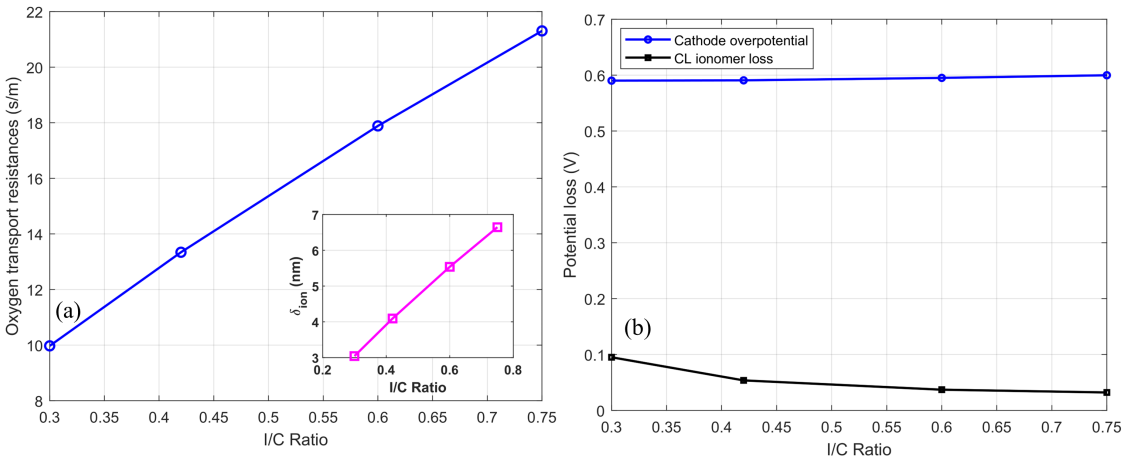

Figure 2.12: (a) The oxygen transport resistance and ionomer thickness, (b) The cathodic overpotential and CL ionomer resistance at $J_{load} = 1.4 \times 10^4$ A/m^2 for varied I/C ratios and bare carbon mass fractions

The main variables affecting the ionomer protonic conductivity are the ionomer film thickness and the relative humidity of the inlet gasses. At dry operating conditions, the ionomer water content is not enough to improve the ionic conductivity which results in higher ohmic resistances. However, the accumulation of excess water in flow fields at high relative humidity results in higher oxygen diffusion resistances through pores, accompanied by reduced cell performance. In this regard, Xing et al. [113] reported the positive impact of high ionomer content together with low relative humidity on cell performance at low current densities while the vice versa reported at high current densities. Thus, the effect of the I/C ratio is further studied using relative humidity of 0.6 with the same CL structural parameters. The polarization and power density curves as well as cathodic overpotential and ionomer potential loss for various I/C ratios are shown in Figure

2.13.

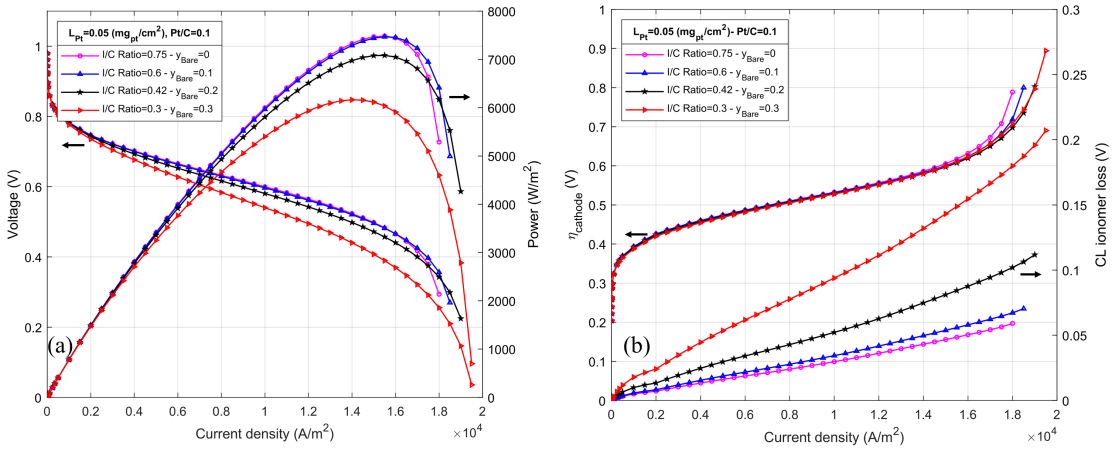

Figure 2.13: (a) Polarization and power density curves, (b) Cathode overpotential and CL ionomer loss for various I/C ratios and bare carbon mass fractions using RH of 0.6

Favorable values of the I/C ratio and bare carbon mass fraction are consistent for both RH conditions. Moreover, the peak power density values of 7469 and 7391 W/m^2 are obtained using an I/C ratio of 0.6 and y_{Bare} of 0.1 for RH of 0.6 and 1 respectively, indicating an improved cell performance for lower RH. Although the oxygen transport resistances are the same for different RH conditions, the oxygen concentration on Pt surfaces differs since the water volume fraction introduced to the cathode channel is higher for fully humidified inlet conditions. The comparison of oxygen concentration for both RH conditions at $J_{load} = 1.7 \times 10^4$ A/m^2 is shown in Figure 2.14. Comparing the results of Figures 2.11 and 2.13, in addition, the performance reduction for small I/C ratios is more severe under lower RH conditions, showing the importance of using an appropriate I/C ratio for low RH. As a result, the peak power densities of 6568 and 6155 W/m^2 are observed for the I/C ratio of 0.3 using wet and dry operating conditions. From Figures 2.11 and 2.13, the CL ionomer resistivity is greatly increased for 0.6 RH in comparison to Figure 2.11, suggesting the dependency of ionomer proton conductivity on its water content.

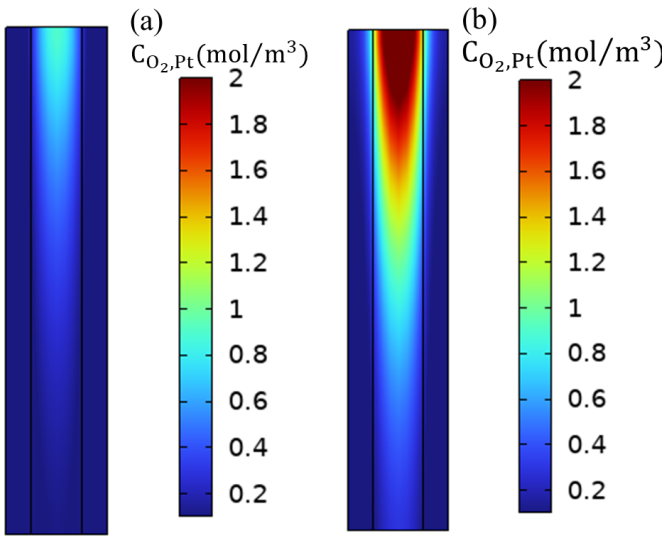

Figure 2.14: The oxygen concentration on the surface of Pt particles using I/C ratio of 0.6 and y_{Bare} of 0.1 for relative humidity of (a) 1, and (b) 0.6 obtained at $J_{load} = 1.7 \times 10^4$ A/m^2

Varying Pt/C and I/C Ratios: In this section, the CL porosity is kept constant by varying the Pt/C ratio, for which the I/C ratio ranges from 0.75 to 2.1. Providing higher Pt/C ratios using a constant Pt-loading of 0.05 mg$_{pt}$/cm^2 decreases the carbon volume fraction, and the addition of more ionomer is required to ensure constant CL porosity. Based on the findings of Ref. [105], the CL thickness is not a function of I/C ratios for values smaller than 3, and the fixed CL thickness assumption is valid for this analysis mode. The polarization and power density curves of this analysis mode as well as the cathodic overpotential and ionomer potential loss are shown in Figure 2.15.

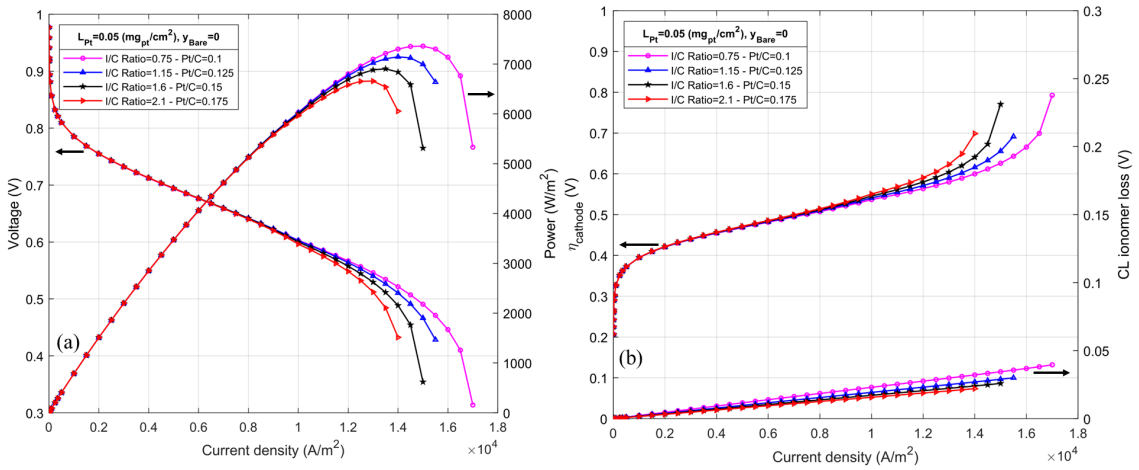

Figure 2.15: (a) Polarization and power density curves, (b) Cathode overpotential and CL ionomer loss for various I/C and Pt/C ratios

The cell performance is constant for current densities smaller than $J_{load} = 1 \times 10^4$ A/m^2, and it deviates for higher operating current densities. The peak power density over all the studied cases is related to the I/C ratio of 0.75 and Pt/C ratio of 0.1. The ionomer potential loss is directly related to the I/C ratio, and the use of small I/C ratios adds to this loss. However, the variations in ionomer potential loss are minimal due to the high considered values of the I/C ratio. Thus, the cell performance is consistent for a wide range of current densities while the effect of cathodic overpotential intensifies at high current densities due to oxygen deficiency. To better understand the cause of the cathodic overpotential and ionomer potential loss variations, these two variables are plotted against different I/C ratios for the current density of $J_{load} = 1.4 \times 10^4$ A/m^2 in Figure 2.16.

Higher I/C ratios create a thicker ionomer layer in the CL, and it increases the resistance associated with the oxygen diffusion through the ionomer layer as well as the oxygen interfacial resistance at the surface of Pt particles defined as proportional to the ionomer diffusional resistance in equation 2.48. As a result, the oxygen transport resistance is increased more than two times between I/C ratios of 0.75 and 2.1 for high current densities. Although the oxygen concentration in the pores is similar due to the constant CL porosity, the oxygen concentration on Pt surfaces is reduced significantly for high I/C ratios mainly due to higher oxygen transport resistances.

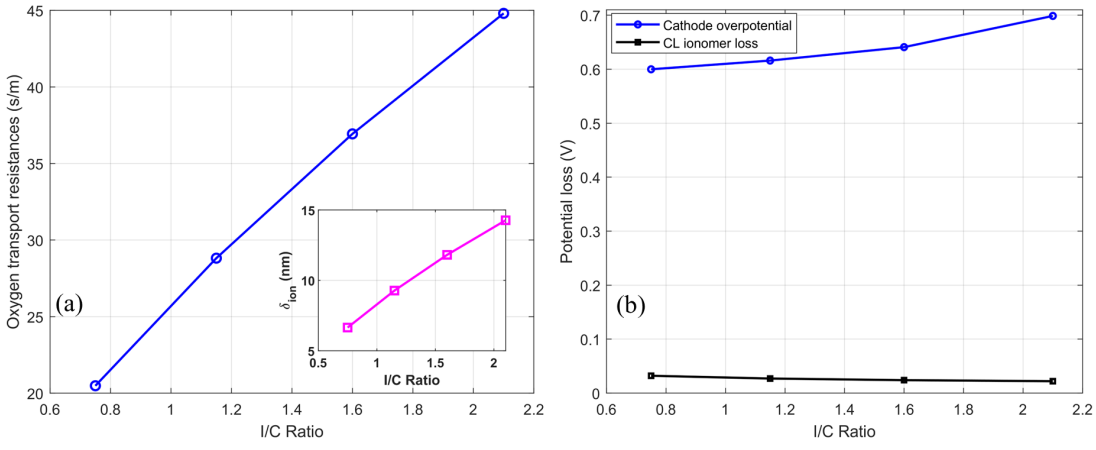

Figure 2.16: (a) The oxygen transport resistance and ionomer thickness, (b) The cathodic overpotential and CL ionomer resistance at $J_{load} = 1.4 \times 10^4$ A/m^2 for varied I/C and Pt/C ratios

2.3.1.4 Effects of CL Particles Radii

The catalyst particles need to be dispersed on conductive support mostly carbon-based materials to promote Pt dispersion, electrode kinetics, and electron transportation [27]. Higher interaction between the catalyst and the support material results in better electrocatalytic activity and stability. The well-known carbon-support material is carbon black which provides excellent electrical conductivity; however, it suffers from corrosion at high voltages [114]. Different carbon-based materials and hybrids are produced to investigate cell performance with various surface areas and radii, which affect the reaction area subsequently. Moreover, the active electrochemical surface area available for ORR reaction greatly affects the cell performance and power density.

The simulated polarization and power density curves for different carbon support radii of 10, 25, 40, and 55 nm are shown in Figure 2.17a. For these simulations, the CL compositions include Pt-loading of 0.05 mg/cm^2, Pt/C ratio of 0.1, y_{Bare} of 0.1, and I/C ratio of 0.6, which represent the best performance in previous sections. A larger carbon support radius intensifies the transport resistance related to the diffusion of oxygen through the ionomer and its dissolution at the ionomer surface heightening the oxygen flux adjacent to reaction sites. As a result, the oxygen transport resistances increase for bigger carbon particles, resulting in higher cathodic overpotentials as shown in Figure 2.17b. Since the constant I/C ratio of 0.6 is utilized for this analysis, the ionomer potential loss is invariant.

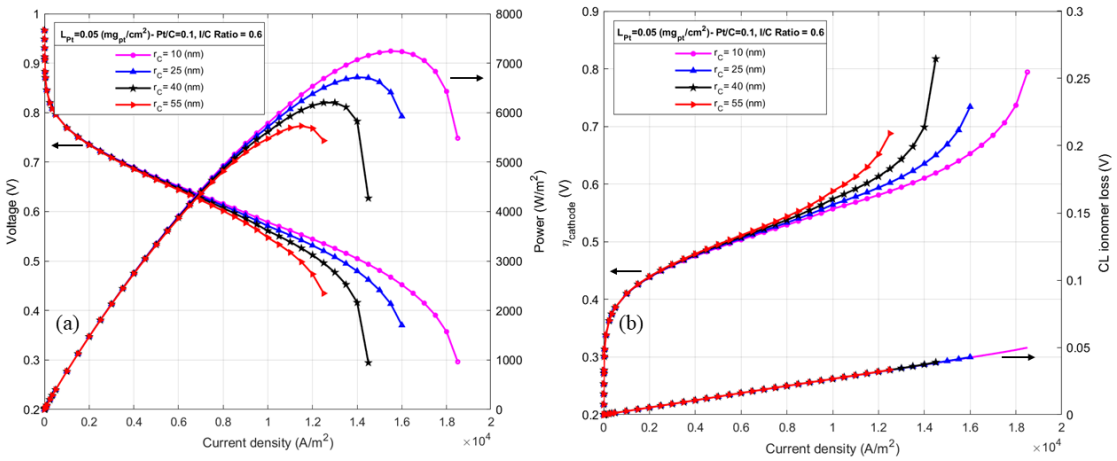

Figure 2.17: (a) Polarization and power density curves, (b) Cathode overpotential and CL ionomer loss for various carbon-support radii

The catalytic active electrochemical area is directly related to the radii of Pt particles and Pt dispersity, and it affects the available reaction area. The effect of Pt particle radii is studied using different values of 2, 4, 3, and 5 nm representing the active electrochemical area of 70, 46, 35, and 28 m^2/g. The obtained polarization and power density curves together with the cathodic overpotential and ionomer loss are shown in Figure 2.18. At the nanoscale, the ratio of surface area to volume decreases with increasing particle radius. Thus, using larger Pt particles reduces the CL reaction area and causes higher oxygen transport resistances while ionomer potential loss is constant. Moreover, the radius of Pt particles causes the deviation of the cell performance over all the current densities but it decreases the cell performance for bigger carbon-support radii only in the limiting current density region.

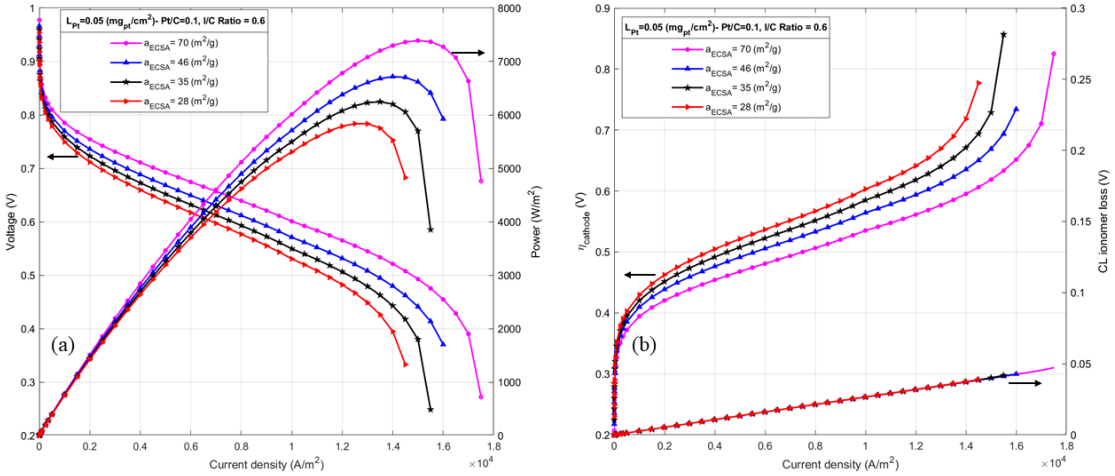

Figure 2.18: (a) Polarization and power density curves, (b) Cathode overpotential and CL ionomer loss for various electrochemical active areas

2.3.2 Channel to Rib Width Ratio (CRWR)

The cell performance largely depends on the proper flow field designs for which the channel geometry and dimensions are the primary dominant factors. The geometrical considerations could be taken into account for mitigating the intense performance losses in low Pt-loaded CLs. In this study, four different CRWRs are analyzed to investigate the effect of channel geometry for the Pt-loading of 0.05 mg/cm^2. The best CL structural parameters studied through section 2.3.1 are chosen for this analysis including Pt/C ratio of 0.1, y_{Bare} of 0.1, and I/C ratio of 0.6. To keep the cell active area constant, the channel

width increases as the land width decreases for a comparative study. The performance and power density curves for different CRWRs are shown in Figure 2.19a.

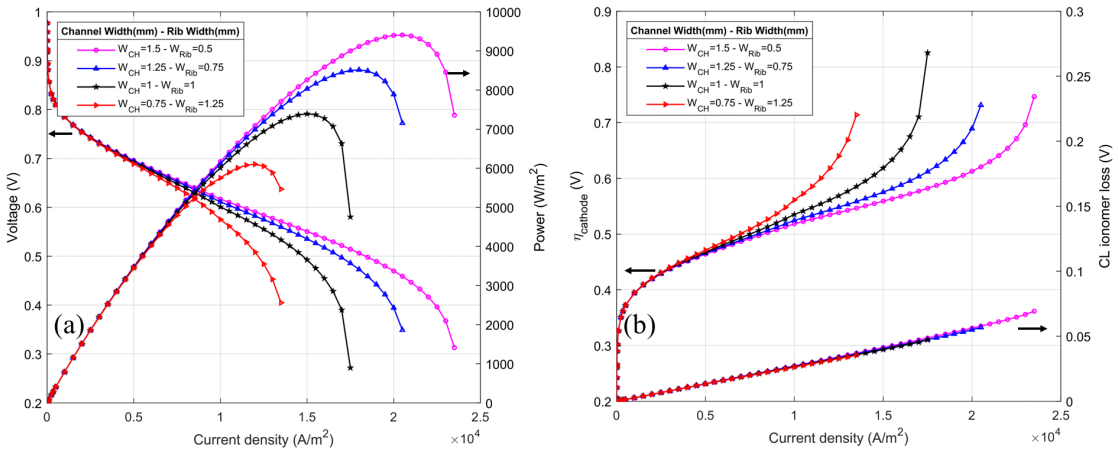

Figure 2.19: (a) Polarization and power density curves, (b) Cathode overpotential and CL ionomer loss for various CRWRs

At low current densities, CRWR does not influence cell performance and local transport resistances. In contrast, the highest peak power density is achieved with a CRWR of 3, representing the great influence of different CRWRs at high current densities. The peak power density is increased by 27 and 15% with the CRWR of 3 and 1.66 compared to the CRWR of 1. At high operating current densities, the most important factor dominating the cell performance loss is the cathodic activation overpotential shown in Figure 2.19b. Higher cathodic overpotential for a given current density using small CRWRs demonstrates the dominance of mass transport losses for high current densities. For small current densities, however, the constant cathodic overpotentials cause the negligible effect of CRWR on the cell performance. Since constant CL structural parameters are considered for this analysis, the ionomer resistance is almost fixed for all CRWRs.

To investigate the cause of the increased cathodic overpotentials for small CRWRs, the oxygen concentration values on Pt surfaces as well as through the GDL are shown for three different CRWRs in Figure 2.20. The same CL structural parameters ensure the same oxygen transport resistance for all the cases; however, the oxygen concentration on Pt surfaces is dramatically reduced for narrow channels, i.e., small CRWRs, indicating a higher mass transport resistance for oxygen in the GDL. Hence, even though the oxygen concentration in the channel does not vary significantly (not shown), under the same current density the oxygen concentration in the GDL drops significantly for narrow channels and lowers the oxygen concentration in the CL. Moreover, for all cases, the oxygen con-

centration is higher under channels than ribs indicating that the in-plane mass transport resistance in the GDL dominates the ORR further at high current densities.

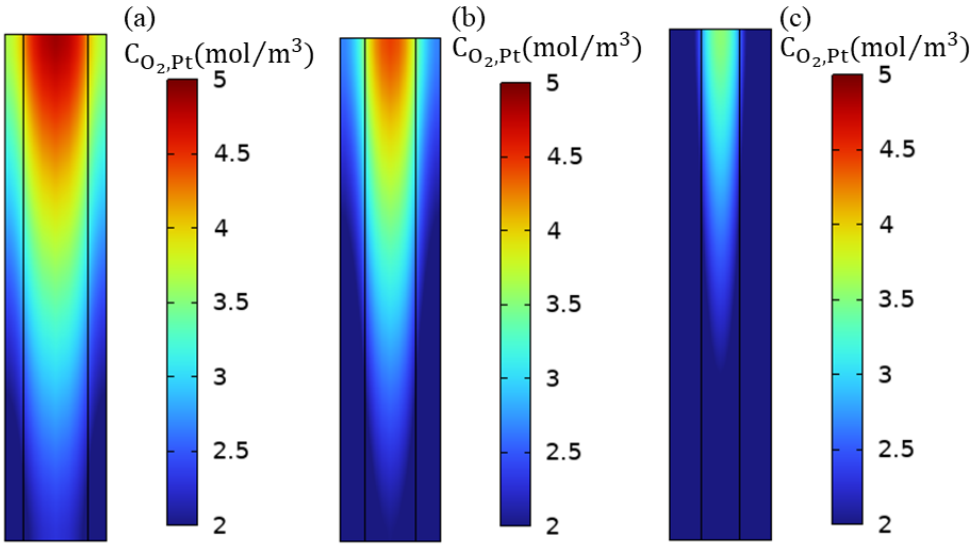

Figure 2.20: The oxygen concentration on the surface of Pt particles and through the GDL for (a),(d) w_{CH} of 1.25 and w_{rib} of 0.75 mm, (b),(e) w_{CH} and w_{rib} of 1 mm, (c),(f) w_{CH} of 0.75 and w_{rib} of 1.25 mm for $J_{load} = 1.4 \times 10^4$ A/m^2

2.3.3 Operating Conditions

The performance of the cell is further evaluated with different relative humidity ratios ranging from 0.6 to 1 as shown in Figure 2.21, with the operating temperature of 80°C and pressure of 1.5 atm. The cathodic Pt-loading is adjusted to 0.1 mg/cm^2 while the Pt/C and I/C ratios are 0.3 and 0.95, respectively.

The level of relative humidity affects the membrane proton conductivity while adjusting the inlet water vapor. The hydration of the membrane is a critical factor, enhancing the ionic conductivity of the membrane and reducing its resistance to proton transport [77]. While the ORR reaction at the CL generates water, it is typically not sufficient to fully hydrate the membrane. Therefore, additional humidification of the reactant gases at the inlets is necessary to maintain proper membrane hydration. As represented in Figure 2.21, minimal performance deviation is observed for different relative humidity ratios. Decreasing the relative humidity positively affects the performance for the limiting current density region, during which the effect of CL flooding is maximized. However, the

cathodic activity and the ionomer potential loss are reduced by enhancing the vapor portion in the inlet resulting in a slight performance increase for activation and ohmic region. For the limiting current density with high relative humidity, the cell has more difficulty removing water, making it more vulnerable to water flooding and leading to higher mass transport resistance.

The impact of operating temperature is investigated by using the relative humidity of 0.8 with the operating pressure of 1.5 atm. Consistent CL characteristics are utilized with the previous operating condition. Higher operating temperatures reduce the ionic conductivity, causing increased potential loss. However, electrochemical reactions occur at a faster rate at higher temperatures, leading to improved fuel cell performance. Therefore, there exists a trade-off between the effect of temperature on ionic conductivity and reaction rate. As demonstrated in Figure 2.21, the operating temperature of 70°C results in increased cell performance while decreasing the temperature reduces the catalytic activity. Further increasing the operating temperature, moreover, deteriorates the performance by hindering the transport of protons through both the ionomer in the CL and membrane [77].

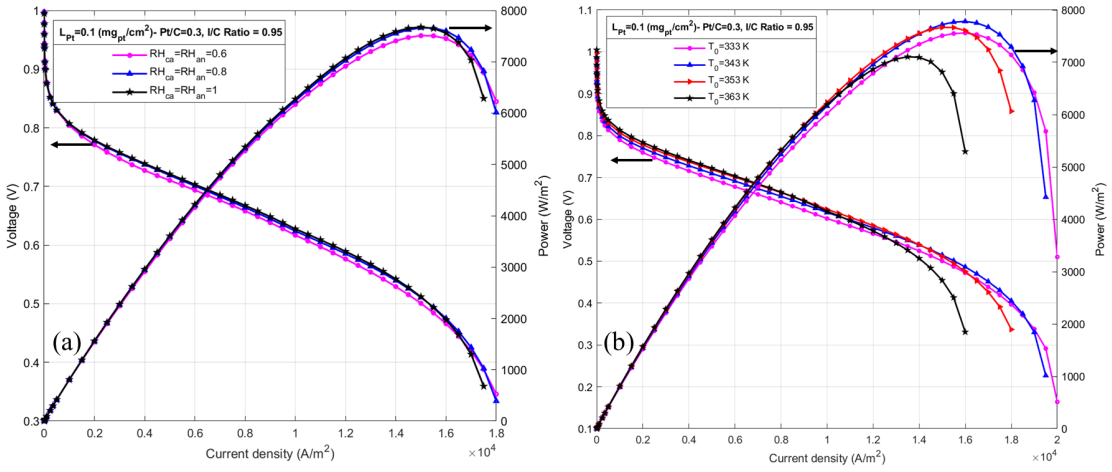

Figure 2.21: Polarization and power density curves for different (a) relative humidity ratios, (b) operating temperatures

Lastly, the effect of operating pressure is investigated considering three different values of 1, 1.5, and 2 atm with a relative humidity of 0.8 and temperature of 70°C and shown in Figure 2.22. The increase of operating pressure leads to better performance, representing an increase of 0.08 and 0.1 V at $j_{load} = 1.5 \times 10^4$ A/m^2 following Ref. [115]. A higher pressure level enhances the availability of oxygen at the CL and subsequently elevates the

rate of reaction. In the absence of technical issues, operating at high pressure benefits the cell performance ensuring minimal pressure fluctuations in experimental setups.

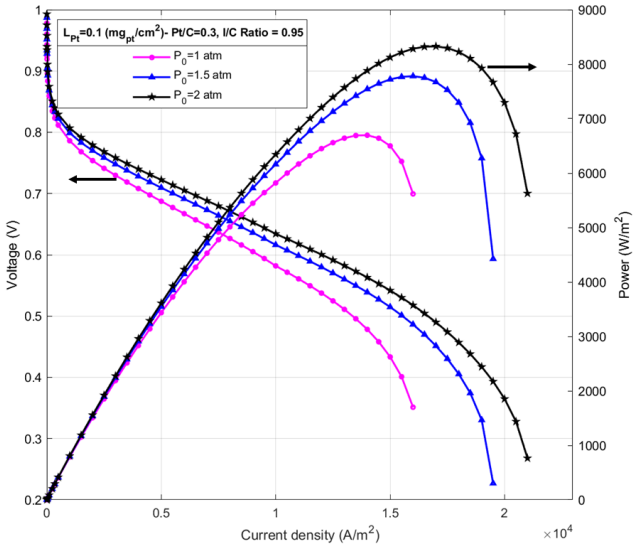

Figure 2.22: Polarization and power density curves for different operating pressures

2.4 Summary and Conclusion

As the most critical component of PEMFCs, the cathode CL has specific physiochemical and functional features that constrain the transport processes at the microscale and the rate of oxygen reduction reaction. Understanding the interplay between the CL parameters is imperative for both reducing the cost and improving the cell performance in PEMFCs. To this aim, the transport resistances of oxygen and protons as well as the performance of a cell portion with straight cathode and anode channels are evaluated using a non-isothermal multi-phase pseudo-three-dimensional PEMFC model. The model is validated against experimental data available in the literature and used to investigate the effects of microstructural parameters of the cathode CL. In addition, the flow filed design parameters are studied for an improved understanding of the effects of the transport processes at the cell level for low Pt-loaded CLs. The following list summarizes the major results and conclusions.

- The Pt-loading influences the peak power density significantly, due to contributions from the cathodic overpotential and ohmic losses in the ionomer phase in the CL.

The former has a major influence on the cell performance at different Pt-loadings. In addition, there exists a threshold value for Pt-loading above which the variations in the cathodic overpotential and cell performance are negligible.

- Addition of bare carbon particles into the CL has a slight negative effect on the performance at moderate dilution ratios, up to about 0.55. The performance drop is more significant at higher ratios and mainly associated with the increased oxygen transport resistances, which increases non-linearly with the bare carbon ratio.

- When the Pt-loading, CL porosity, and Pt/C ratio of the catalyzed carbon particles are fixed, bare carbon particles are used to compensate for varying the ionomer ratio. In this case, high I/C ratios improve cell performance. Potential losses in the ionomer dictate the cell performance with minimal influence of the oxygen transport resistance on the cathodic potential loss.

- High I/C ratios deteriorate cell performance if the Pt/C ratio is adjusted to keep the CL porosity constant without using bare carbon particles. The main reason for this deterioration is the increase of cathodic overpotential due to higher diffusional and interfacial oxygen transport resistances at high current densities. At high ratios of I/C, there is some reduction in the ionomer potential loss, but the effect of oxygen transport resistances is dominant.

- Lowering the RH from 100 to 60% increases the oxygen fraction by reducing the water vapor fraction and improves maximum power density for higher I/C ratios. For small I/C ratios, on the other hand, the cell performance is decreased under dryer operating conditions, showing the dependency of ionomer potential losses on the operating conditions.

- A higher channel-to-rib-width ratio improves the oxygen transport in the catalyst pores, especially under the ribs, and consequently the performance of the cell. Thus, reducing the rib width without deteriorating the mechanical and electric contact conditions of the GDL with the bipolar plate has a positive effect on the overall performance, especially at low Pt loadings.

- The radius of carbon support negatively affects the performance owing to the increased transport resistances, especially at high current densities. Moreover, the

radius of Pt particles is an essential CL parameter since the electrochemically active surface area is directly dependent on its value. Therefore, decreasing the radius of Pt particles elevates the performance but it is bounded by the fabrication limitations.

- For the given operating conditions, decreasing relative humidity enhances the cell performance. High relative humidity results in higher liquid water saturation and subsequently higher mass transport resistances. Moreover, the increase in operating pressure causes an elevated oxygen fraction in the cathode inlet leading to enhanced cell performance. Furthermore, higher temperatures enhance the catalytic activity while increasing the ionic potential loss. This interplay is of great importance for choosing the optimized operating condition and is also affected by the relative humidity ratio.

Chapter 3

EVALUATING THE TRANSIENT RESPONSE OF LOW PLATINUM LOADED PEM FUEL CELLS

3.1 Introduction

Transient response and dynamic characteristics of PEMFCs under load cycling, idling, startup, and shutdown processes are important to understand the conditions leading to the degradation of PEMFCs. Under actual automotive operation mode, the voltage response delay and voltage undershoot happen due to fuel starvation and transient variations of cell water content [116]. These variations result in adverse conditions including voltage perturbations, uneven reactant distributions, and flooding issues which cause performance fluctuations and component degradation such as carbon corrosion of the catalytic layer and Pt dissolution [116].

Transient experimental studies mostly focused on slow processes including water accumulation in the GDL and relaxation of membrane water content [116]. Moreover, numerous experimental studies investigated the over and undershooting current and cathodic gas compositions upon voltage or current cycling. In this regard, Kim et al. [9] experimentally investigated the transient response of PEMFCs under various air stoichiometry, humidity, and excess ratios. The authors reported increased voltage undershoots with higher step currents due to Ohm's law [9]. In addition, the authors presented decreased oxygen concentration and ionic conductivity for lower air stoichiometry and humidity ratios respectively, resulting in higher voltage drops [9]. The adverse effect of low cathodic humidity ratios both on steady-state and dynamic characteristics of PEMFCs is further

confirmed by Yan et al. [117] while representing the positive impact of higher operating pressures under large current steps and high operating current densities. Furthermore, Cho et al. [118] reported two time delay periods, the first one caused by through-plane (TP) gas convection and mass transfer limitation, which is in the order of 1 s, while the second one concerns membrane water content recovery taking about 10 s. The authors concluded that voltage undershoot is mainly caused by oxygen supply delay, non-uniform oxygen distribution, and flooding issues. Recently, Huang et al. [116] studied the impact of stoichiometry ratios for low current densities, while a negligible effect is found at high current densities. The authors proposed stable large-scale dynamic cell response upon appropriate initial membrane water content [116].

Several transient models have been proposed to understand the complex transport phenomena investigating the effect of operating conditions, membrane properties [54], and flow field design characteristics [55][56]. Using a three-dimensional (3D) dynamic model, Wang et al. [56] represented the transient response time of 10 s for reaching a new steady-state condition due to the membrane water accumulation. The authors investigated that increased step current under dry operating conditions causes the anode to dry due to electro-osmotic drag [56]. Moreover, Kim et al. [119] reported a significant effect of temperature in modifying the over-undershoot peak, causing the single-phase and isothermal models to overestimate the voltage fluctuations. Furthermore, Goshtasbi et al. [10] proposed a three-dimensional (3D) model for studying the transient response of PEMFCs. The authors suggested the dominance of water redistribution on the transient cell response. Moreover, the authors related the redistribution time delay to the operating conditions, two-phase flow, and membrane water uptake [10].

Most numerical studies consider simplified reaction kinetics neglecting the microstructural characteristics of different layers and anisotropic material properties. Capturing the most salient features of cell dynamics, however, requires a comprehensive transient model to capture the critical transient phenomena [59][13]. The CL microstructural parameters including the Pt loading, Pt/C ratio, I/C ratio, and dilution rate define the performance and durability. Although Pt decrement is a key factor for overcoming cost issues and facilitating the widespread use of PEMFCs, the dynamic behavior of PEMFCs is rarely studied for low Pt-loaded fuel cells.

In this thesis research, the detailed P3D model described in chapter 2 is utilized to

assess the CL microstructural parameters on the dynamic behavior of PEMFCs. The CL characteristics are found to dramatically affect the steady-state performance of low Pt-loaded CLs [120]. To unravel the interplay between CL features and their effect on dynamic cell behavior, the effect of Pt-loading, I/C ratio, and additional bare carbon particles, CL thickness, and Pt/C ratio are studied. Moreover, further investigation is performed by considering different operating conditions including stoichiometry and relative humidity ratios of reactants on dynamic response.

The following chapter starts with the model development section including the modeling domain, governing equation, and model validation. In section 3.3, the results obtained are provided in two separate subsections concerning the CL characteristics and operating conditions. A summary of the chapter highlighting important conclusions is provided in chapter 2.

3.2 Model Development

3.2.1 Modeling Domain

The modeling domain of interest includes channels and GDLs explicitly while thin CLs and the membrane are included implicitly by the addition of through-plane (TP) fluxes. The computational domain is projected on a single surface and the symmetry causes the channels and ribs to overlap. A complete description of the modeling domain and the mesh is provided in chapter 2.

3.2.2 Governing Equations

The flow distribution in the channels and GDLs is obtained by solving the time-dependent two-dimensional Brinkman equations simultaneously with Maxwell equations. Moreover, liquid water transport through ionomer is evaluated by considering adsorption, desorption, and water generation processes. Furthermore, the energy equation, liquid water transport through the GDLs, and charge conservation for obtaining the ionic and

electric potentials are considered. The time-dependent governing equations are provided in Table 3.1 while a detailed description of the P3D model alongside the involved sub-models concerning the electrochemical reaction kinetics and water transport is provided in chapter 2.

Table 3.1: Governing equations

Description	**Equation**	
Mass Conservation	$\frac{\partial(\rho\,\varepsilon)}{\partial t}\nabla\cdot(\rho\mathbf{u}) = S_{mass}$	(3.1)
Momentum Conservation	$\rho\frac{\partial\mathbf{u}}{\partial t} + \rho\mathbf{u}\cdot\nabla\mathbf{u} = -\nabla p + \mu\nabla^2\mathbf{u} - \frac{\mu}{\kappa}\mathbf{u}$	(3.2)
Species Distribution	$\varepsilon\,\rho\frac{\partial w_i}{\partial t} + \nabla\cdot\left(\rho\,w_i\sum_j D_{ij}\,\nabla X_j\right) + \rho\,(\mathbf{u}\cdot\nabla)\,w_i = S_i$	(3.3)
Electronic Potential	$\nabla\cdot(-\sigma_s\nabla\phi_s) = S_{\phi_s}$	(3.4)
Ionic Potential	$\nabla\cdot(-\sigma_m\nabla\phi_m) = S_{\phi_m}$	(3.5)
Dissolved Water	$\frac{\partial\left(\frac{\rho_{mem}\lambda}{EW}\right)}{\partial t} + \nabla\cdot\left(\frac{-\rho_{mem}}{EW}D_{H2O}^{Naf}\nabla\lambda\right) + \nabla\cdot\left(\frac{-n_d}{F}\sigma_l\nabla\phi_l\right) = S_\lambda$	(3.6)
Energy Conservation	$(\rho C_p)_{eff}\frac{\partial T}{\partial t} + (\rho\,C_p)_{eff}\,\mathbf{u}\cdot\nabla T + \nabla\cdot(-k_{eff}\nabla T) = S_T$	(3.7)
Liquid Water	$\frac{\partial\,(\rho\,\varepsilon)}{\partial t} + \nabla\left(\frac{\rho_l k_l}{\mu_l}\nabla p_l\right) = S_l$	(3.8)

The equation 3.6 concerns the transient membrane water content. Since the model solves for membrane water content implicitly, the 3-point finite difference method with the ghost nodes approach at the anode and cathode boundaries, based on equation 3.6, is utilized to evaluate the derivatives of this equation as follows,

$$\dot{\lambda_X} = (K_{1,X} - K_2)\,\lambda_{X+1} - 2K_{1,X}\lambda_X + (K_{1,X} + K_2)\,\lambda_{X-1} \tag{3.9}$$

where X relates to the nodes of the domain including anode, membrane, and cathode, as well as two more ghost nodes (an^-, ca^+). The variables in equation 3.9 including $K_{1,X}$ and

K_2 are described as,

$$K_{1,X} = \frac{4D_{H_2O}^{Naf,X}}{\delta_{mem}^2} \tag{3.10}$$

$$K_2 = \frac{EW}{\delta_{mem}\,\rho_{mem}} \frac{2.5}{22} \frac{j_{cell}}{F} \tag{3.11}$$

The λ at ghost nodes is evaluated based on the boundary condition at these nodes as,

$$\lambda_{an^-} = \lambda_m + \frac{k_{ads}\,\delta_{mem}}{D_{H_2O}^{Naf,an}} (\lambda_{an}^{eq} - \lambda_{an}) \tag{3.12}$$

$$\lambda_{ca^+} = \lambda_m + \frac{k_{des}\,\delta_{mem}}{D_{H_2O}^{Naf,ca}} (\lambda_{ca}^{eq} - \lambda_{ca}) \tag{3.13}$$

The complete definitions for all the variables are provided in chapter 2.

3.2.3 Numerical Implementation

The numerical model is implemented in the commercial finite-element software COMSOL Multiphysics. It employs a mapped mesh comprising 1800 quadrangular linear elements with a double boundary layer at the channel-rib interface. The fully coupled solver is utilized to solve nonlinear equations with Newton iterations. A PARDISO direct solver is employed to solve the linear systems of equations at each time step. The time-stepping method used is the backward differentiation formula (BDF) with a maximum step size of 500 milliseconds. The simulations were conducted on a workstation equipped with a 3.6 GHz quad-core processor and 32 GB of RAM.

3.2.4 Model Validation

The accuracy of the model in capturing the transient behavior of PEM fuel cells is evaluated using the experimental data presented by Pei et al. [121]. The authors investigated the impact of step current on the dynamic response of a cell with 25 cm^2 active area and Pt-loading of 0.3 and 0.1 mg/cm^2 at the cathode and anode, respectively. The model parameters for this validation are presented in Table 3.2 while the comparison of

the results is presented in Figure 3.1.

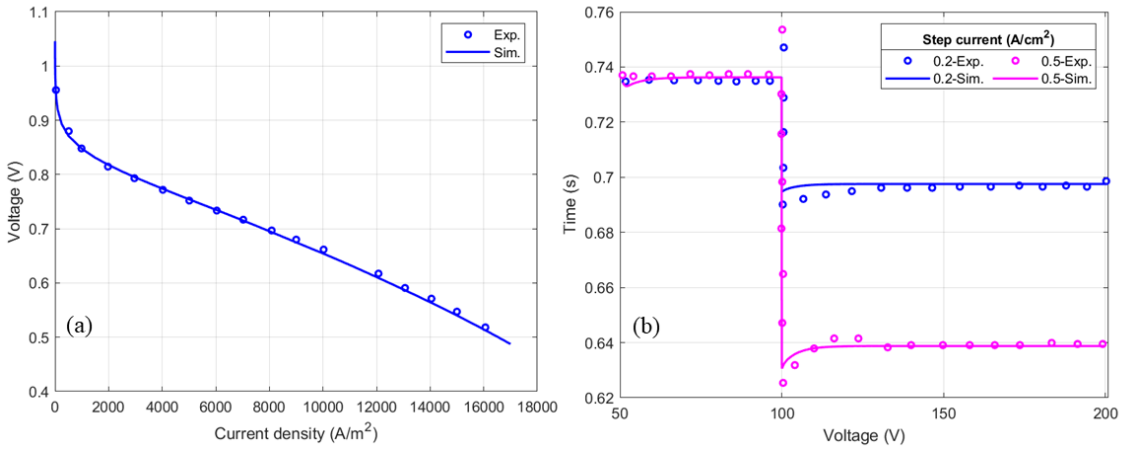

Figure 3.1: The comparison of simulation results and experimental data, (a) for steady-state performance and (b) dynamic response of the model under various step currents compared to experimental data of Ref. [121]

As demonstrated in Figure 3.1, the model accurately captures the steady-state performance of the cell. Moreover, the model shows good agreement in predicting the dynamic cell response under different step currents of 0.2 and 0.5 A/cm^2. The undershoot amplitude increases for higher step currents, and the model successfully captures this response with minor deviations from the experimental data.

Table 3.2: Model parameters used for validation against experimental data sourced from [121]

Parameter	**Value**	**Unit**
δ_{CL}	15	µm
δ_{mem}	50	µm
a_{ECSA}	60	m^2/g
γ_{an}	2	—
α_{ca}	0.43	—

3.3 Simulation Case Studies

The non-isothermal two-phase P3D model is used to reveal the cell dynamic response under various CL compositions namely Pt-loading, Pt/C ratio, I/C ratio, and the bare

carbon mass fraction, y_{Bare}. In addition, the cell dynamic behavior is further studied under different inlet relative humidity and stoichiometry ratios. The base model parameters are provided in Table 3.3 while a full description of the remaining parameters is provided in section 2.2.

Table 3.3: Geometrical and operational parameters and their base values

Description	**Parameter**	**Value**	**Unit**
Channel length, width, height	L_{CH}, w_{CH}, h_{CH}	50, 1, 1	mm
Land width	w_{rib}	1	mm
Inlet stoichiometry ratios for cathode,anode	st_{ca}, st_{an}	2, 1.2	—
Inlet relative humidity for cathode, anode	RH_{ca}, RH_{an}	0.6, 0.6	—
Operating and reference temperature	T, T_0	353, 298	K
Operating and reference pressure	P, P_0	1, 1.5	atm

The result section of this work is separated into two parts including the CL morphology and operating conditions. The former constitutes evaluating the peak under-overshoot using different CL design variables which are controlled during fabrication processes and found to modify the steady-state performance dramatically [77], while the latter concerns comparing low Pt-loaded cells using two different input values for each operating parameter. The Galvano-dynamic approach is utilized for which the current density profile is the model input and is shown in Figure 3.2. The magnitude of the current steps, especially the middle one, is selected high enough to stimulate the system dynamics.

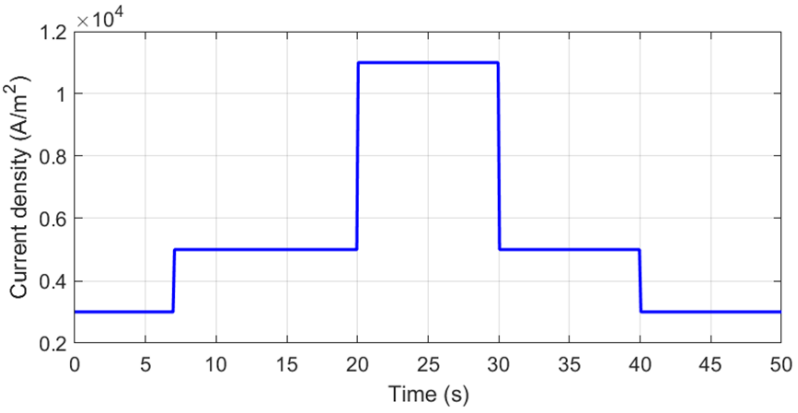

Figure 3.2: The applied current profile

3.3.1 Catalyst Layer Characteristics

The effect of Pt-loading is investigated considering two different Pt-loadings of 0.2 and 0.05 mg/cm^2 for the cathode electrode, the result of which is shown in Figure 3.3. Since the rate of cathodic reduction reaction dominates the cell performance, the detailed electrochemical reaction model is only considered for the cathode, while the facile kinetics of hydrogen oxidation reaction (HOR) ensures negligible anode kinetic losses. A constant CL porosity of 0.57 is assumed for all simulation case studies to eliminate the pore volume effect on the cell dynamics. Additionally, the salient CL features are deliberately modified under the constant CL thickness condition for this simulation case study. For studying the effect of Pt loading, the Pt/C weight ratio is modified to adjust the CL thickness keeping the I/C ratio as 1.

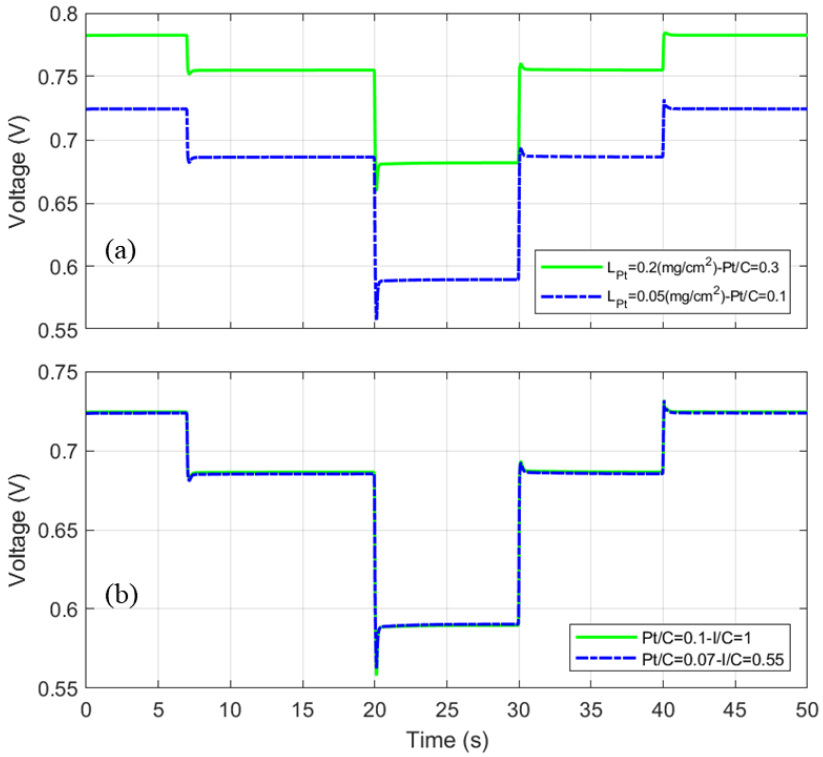

Figure 3.3: The comparison of dynamic response under constant CL thickness assumption for, (a) Different Pt-loaded CLs and (b) Different I/C ratios

As demonstrated in Figure 3.3a and discussed in chapter 2, the cell voltage decreases for the low Pt-loaded cell. Since the Galvano-dynamic profile is provided, the cell water content is not affected by water generation of the electrochemical reaction for differ-

ent Pt-loadings. Furthermore, constant CL thickness assures consistent heat generation through the cell. Consequently, higher Pt-loading results in a better dynamic response represented by lower voltage undershoot. The higher oxygen transport resistances of low Pt-loaded CLs cause lower levels of oxygen concentration at the surface of Pt nanoparticles as demonstrated in Figure 3.4, which results in inferior oxygen distribution in the cell. While the oxygen concentration is lower for all current densities in the 0.05 mg/cm^2 Pt-loaded cell, the difference between the two concentrations is more pronounced right after the load change. This leads to a higher voltage undershoot for the low Pt-loaded cell.

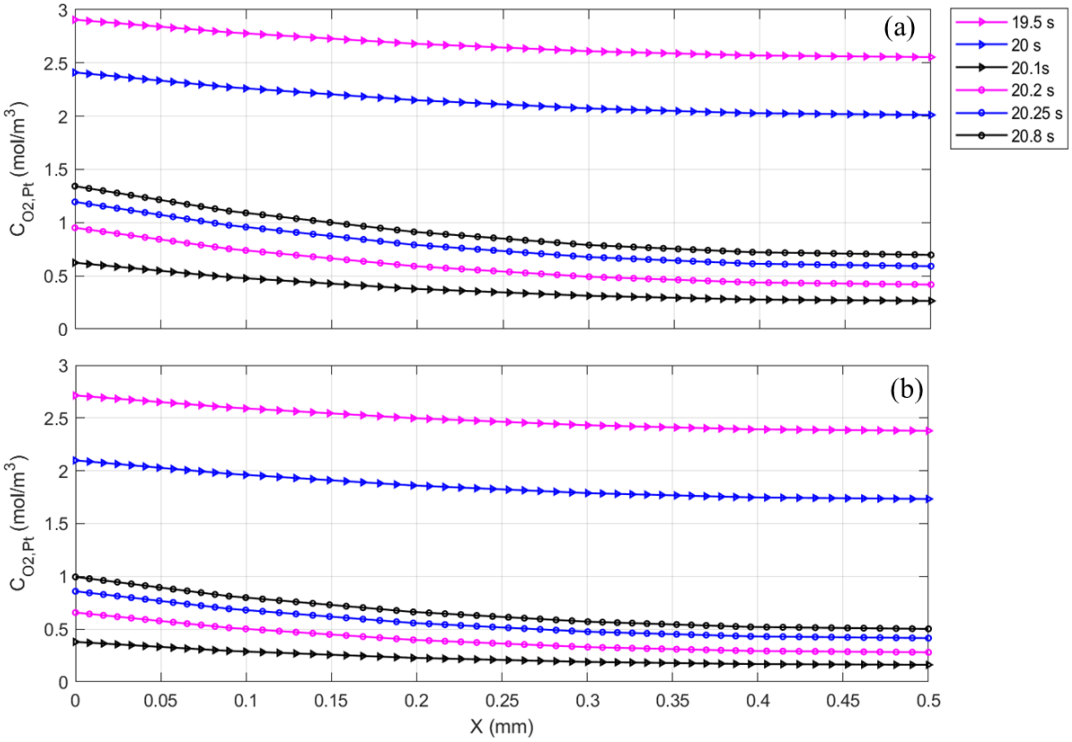

Figure 3.4: The oxygen concentration on the surface of Pt nanoparticles at the cathode outlet under the rib for different Pt-loaded samples, (a) 0.2 (b) 0.05 mg/cm^2

The I/C ratio is one of the CL deterministic variables providing a proton conduction path for ions to reach the electrochemical active region. A higher I/C ratio produces a thicker ionomer layer causing higher diffusional and interfacial transport resistances since the latter resistance is directly proportional to the former. Conversely, lowering the ionomer content increases the CL ionomer potential loss [77]. The impact of the I/C ratio is investigated using constant Pt-loading of 0.05 mg/cm^2 by varying the Pt/C ratio and I/C ratio simultaneously to ensure constant CL thickness and porosity, and the results are shown in Figure 3.3b. The voltage responses are closely related for two I/C ratios of 0.5

and 1 since the effect of the I/C ratio dominates the cell performance for limiting current density region meaning current density values greater than or close to 2 A/cm^2 as well as for values of I/C ratio below 0.3 [77]. Lowering the CL ionomer content positively affects the voltage undershoot under constant Pt-loading and CL thickness conditions due to the small reduction in the voltage undershoot. The lower I/C ratio decreases the oxygen transport resistance due to the thinner ionomer layer resulting in higher oxygen concentration on the surface of Pt particles.

The additional bare carbon particles in diluted CLs provide insight into the Pt dispersion and utilization in different CLs. The bare carbon particles are added to the CL to increase the CL thickness using different Pt/C ratios, and modifying the number of catalyzed Pt/C particles available for the electrochemical reaction. Since the variation of bare carbon mass fraction, y_{Bare}, modifies the CL thickness affecting the heat generation and water distribution, the effect of dilution is investigated for both constant and varied CL thickness by considering different Pt/C ratio and y_{Bare} combinations, and the results are shown in Figure 3.5.

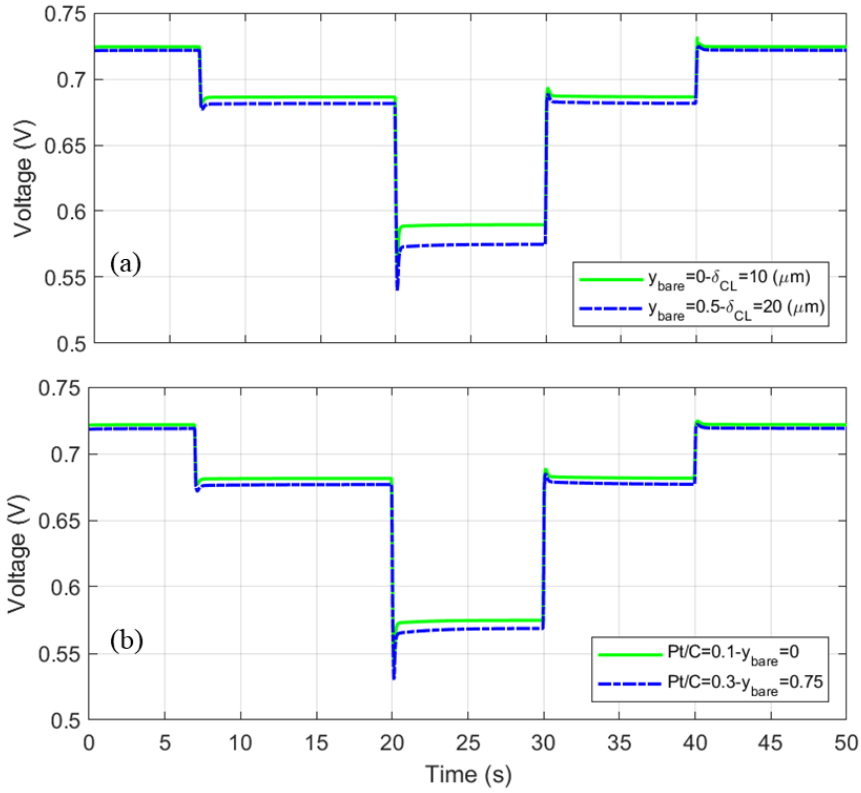

Figure 3.5: The comparison of dynamic response, (a) Different CL thickness and (b) Different bare carbon mass fractions

Higher dilution rates increase both the oxygen transport resistances and the ionomer voltage losses. Under the constant CL thickness condition, including more bare carbon particles adversely affects the oxygen transport resistances and results in larger voltage undershoots. Moreover, the effect of additional bare carbon particles is more intense for high current densities representing more voltage difference between the two cases for the third current density step. It takes 5 s for the thicker cell to reach a new steady state condition due to the enhanced oxygen transport resistances, while the thinner cell is stabilized after 2 s. However, the voltage response barely deviates for the first and last current density steps with a current density value of $3\times\ 10^3$ A/m^2. In addition, the CL thickness barely affects the voltage undershoot as demonstrated in Figure 3.5b, while the voltage response deviates for the thicker CL for all the current density steps, especially the third voltage step.

3.3.2 Operating Conditions

The operating conditions of PEM fuel cells including current, voltage, system pressure, temperature, inlet relative humidity, and inlet stoichiometric ratio define the dynamics of cell response. These parameters serve as the model inputs, which are effectively controlled in an automotive system. The effect of operating conditions is investigated in this section using a cell with Pt-loading of 0.05 mg$\diagup$cm^2, Pt/C ratio of 0.1, and I/C ratio of 1.

The humidity ratio of reactants is studied considering two values of 1 and 0.6 for both cathode and anode electrodes. Although the humidity levels of anode and cathode are not studied separately here, complex phenomena explain the cell performance under different humidity ratios for various current densities. Higher cathodic humidity elevates the rate of back diffusion from the cathode, while the electro-osmotic drag from the anode exceeds the back diffusion at high current densities. Thus, increasing the anodic relative humidity improves the cell performance by counteracting the back diffusion phenomenon and improves the membrane conductivity [117]. In contrast, higher cathodic relative humidity increases the water vapor fraction in the inlet causing water flooding and pore blockage in the GDL as well as higher oxygen transport resistance in the CL. As demonstrated in

Figure 3.6a, the cell voltage response is closely related for two humidity levels except the high current density step, for which the higher mass transport resistances deteriorate the cell performance resulting in a lower voltage response for higher humidity ratios. Moreover, the voltage undershoot is increased for higher relative humidity providing an unstable cell response due to lower oxygen concentration.

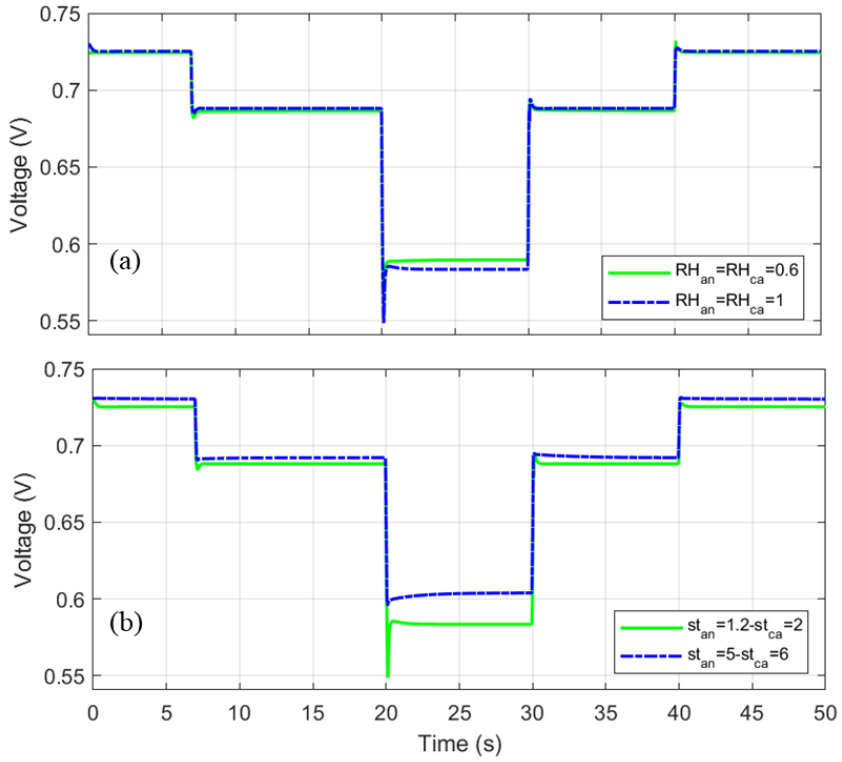

Figure 3.6: The comparison of dynamic response, (a) Different relative humidity and (b) Different stoichiometry ratios

Figure 3.6b represents the comparison of the cell voltage response under two different stoichiometric ratios with values of 1.2 and 2 as low flow rate, and 5 and 6 as high flow rate conditions for anode and cathode, respectively. The inlet stoichiometric flow rate influences the oxygen availability as well as the membrane humidity, which in turn affects the total ionic resistance. Decreased mass transport resistances for higher stoichiometric ratios avoid the generation of voltage over-undershoots while it takes 7 s for the system to reach a new steady state condition. In contrast, the channel is easily depleted from oxygen under low flow rate conditions causing a voltage undershoot of around 0.05 V for the highest current density step. In addition, the generated cell voltage is enhanced providing a higher inlet stoichiometry ratio for reactants, and this dependency is more

intense for high current densities.

3.4 Summary and Conclusion

The dynamic behavior of PEM fuel cells is dependent on different structural, geometrical, and operational parameters. In this chapter, the dynamics of fuel cell response are evaluated under different CL compositions and operating conditions considering the Galvano-dynamics approach for load transients. To this end, the cell voltage response with straight cathode and anode channels is studied with a non-isothermal multiphase pseudo-three-dimensional (P3D) model considering the microstructural characteristics of the CL and wettability features of different porous layers.

- The voltage undershoot increases for low Pt-loading owing to the instability and higher oxygen transport resistances of low Pt-loaded cells. The elevated oxygen transport resistances modify the oxygen concentration on the surface of Pt particles.

- Increasing the I/C ratio, the deviation of dynamic behavior is negligible since the I/C ratio modifies the limiting current density region as demonstrated in chapter 2.

- Larger voltage undershoot is observed when the mass fraction of bare carbon particles is increased under the constant CL thickness. However, the voltage undershoot is almost consistent, varying the CL thickness upon the addition of bare carbon particles. This stems from the increased tortuosity of CL upon the addition of bare carbon particles in a fixed CL thickness which increases the oxygen transport resistances in the CL.

- A higher stoichiometric flow rate enhances the voltage response by elevating the generated voltage, especially at high current densities, as well as smaller voltage undershoots. However, running the cell at elevated stoichiometric ratios is constrained by the limits of the fuel cell device as well as the cost of fuel production.

- The impact of stoichiometric ratios significantly dominates the cell dynamic response compared to all the studied CL features and operating conditions.

Chapter 4

EXPERIMENTAL DEVELOPMENT OF LOW PLATINUM LOADED PEM FUEL CELLS

4.1 Introduction

Lowering the Pt-loading in the cathode catalyst layer (CCL) is necessary while maintaining the performance and durability to overcome the cost issues, requiring the optimized CCL design for high electrocatalytic activity and enhanced cell performance. While extensive research is focused on decreasing the Pt-loading in the CL, most of these studies simply focus on material development for enhancing the ORR activity. The CL morphological features including the Pt-loading, Pt/C ratio, ionomer content, dilution ratio, and carbon support material, controlled during the fabrication process, significantly affect the overall performance, yet the interplay within these variables is not thoroughly understood.

Apart from the CL design variables, the CL fabrication method plays an important role in the CL performance. The fabrication method affects different CL characteristics including the surface area of Pt particles, Pt dispersity, the agglomeration within the CL, and eventually Pt utilization, each of which facilitates a decrease in Pt-loading. For instance, smaller Pt particles and lower levels of agglomeration provide a high catalytic specific surface area suppressing oxygen transport resistances associated with low Pt-loading. Therefore before any electrochemical advancements in catalysts, PEMs, or ionomers, the development of a reliable, reproducible, and lab-scale CL fabrication method is imperative.

To investigate the effect of CL design variables and bridge the research gap discussed in chapter 1, various MEAs are developed with different CL microstructural characteristics in this research, providing the framework for analyzing the impact of each parameter. Moreover, the reliable ultrasonic coating method is utilized for preparing CCMs by directly depositing the CL on the PEM, which reduces the interface resistances. The primary aim of the current research is to characterize cell performance for different Pt-loading, Pt/C ratios, bare carbon mass fractions, and CL thickness through polarization curves, cyclic voltammetry (CV), and electrochemical impedance spectroscopy (EIS). Additionally, the effect of carbon support material is investigated, considering the hybrid catalyst produced previously by Kaplan et al. [114].

The outline of this chapter is as follows. Section 4.2 describes the methods utilized in this research study including the experimental setup, MEA preparation, and catalyst fabrication. The details regarding the electrochemical characterization methods are provided in section 4.3, followed by the results investigated in section 4.4. Finlay, the summary of the main conclusions is provided in section 4.5.

4.2 Experimental Materials and Methods

The following section contains details regarding the materials, and experimental methods used for preparing various cells. This includes the whole steps taken through this research including the catalyst and electrode fabrication as well as membrane electrode assembly.

4.2.1 Experimental Setup and Materials

The test station used is a Model 850e from Scribner Associates with a voltage accuracy of ± 3 mV. The operating pressure is controlled through a high-temperature back-pressure unit. This test unit is accompanied by a computer-controlled instrument providing control over the reactant flows, temperature, humidity, and load. All fuel cell tests are conducted with 8.17 cm^2 MEAs with serpentine channels with ten turns, composed of 1 mm channel

and rib widths as demonstrated in Figure 4.1.

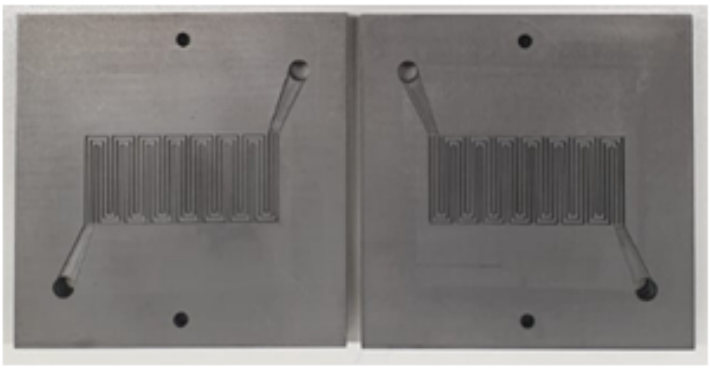

Figure 4.1: Serpentine flow fields with 8.17 cm^2 active area

Nafion® NR-212 membrane as the electrolyte and Sigracet 39BC GDL were purchased from FuelCellStore. Moreover, 40 and 20 wt.% Pt on carbon black was purchased from Alfa Aesar. In addition, Vulcan XC-72 was purchased from Fuel Cell Earth LCC and Nafion® solution with 20 wt.% alcohol content was purchased from Sigma-Aldrich.

4.2.2 Catalyst Fabrication

The CL represents a heterogeneous and intricate structure that necessitates meticulous optimization to enhance mass transport and reaction rate while considering the economical and technical constraints. This necessity arises from the inherent transport limitations of the CCL and the sluggish kinetics of ORR. Therefore, deliberate consideration of the CL microstructure is imperative for addressing the reported increased transport resistances encountered in low Pt-loaded CLs [5][65][63]. The resistances predominantly arise from factors such as the Pt surface area [63], the ionomer layer encompassing the Pt-supported nanoparticles [67], and the surrounding water film [82].

The CL is fabricated by drying the catalyst ink deposited on the membrane or GDL. The microstructure of the CL is influenced by the characteristics of the catalyst ink, the drying process, and the deposition method. Typically, the catalyst ink consists of a solid catalyst, ionomer, and solvent. Therefore, the characteristics of each component and the interactions significantly affect the CL morphology [122]. Pt particles are employed as the

catalyst in PEMFCs due to the enhanced catalytic activity and stability for HOR and ORR. The particle sizes, quantity, and dispersion of Pt are crucial in forming the ionomer-Pt interface for the electrochemical reaction [111][123]. A strong bond between Pt and carbon particles as well as carbon particles and ionomer solution is necessary for the formation of a triple-phase-boundary, however, strong ionomer adsorption on Pt surfaces causes a reduction of the catalytic activity [123]. The oxidation reaction of alcohol, commonly used as the ink solvent, causes catalyst degradation and Pt agglomeration [124]. Notably, the alcohol content in the CL defines the CL microstructure and pore morphology by modifying the drying process [122]. Alcohol-rich ink results in the presence of free ionomers and mitigates ionomer agglomeration, resulting in a more uniform ionomer connection and a denser pore structure, resulting in reduced ionic resistances and higher mass transport resistances. Moreover, the addition of organic solvents determines the evaporation rate during the drying process, modifying the pore structure and the cell performance [125][25]. However, the solvent properties and components are beyond the scope of this work.

To this aim, the catalyst inks are prepared by sonicating the electrocatalysts, deionized water, isopropyl alcohol (IPA), and Nafion® solution for 2 hours, followed by overnight stirring at room temperature. The effect of CL composition is studied by varying the electrocatalyst properties such as Pt/C ratio, Pt-loading, and mass fraction of bare carbon particles, while the ionomer to carbon weight (I/C) ratio is fixed as 1. The details of different produced samples are provided in Table 4.1. The consistent type of anode electrode is used for all the experiments with Pt-loading of 0.1 ± 0.01 mg/cm^2 using a Pt/C ratio of 40 wt.$\%$ and I/C ratio of 1.

Table 4.1: Various compositions of CCL

Samples	**Pt-loading (mg /cm^2)**	**Catalyst type (Pt/Carbon support)**	**Carbon fraction (y_{Bare})**	**CL thickness (µm)**	**Dilution**
S_1	0.2 ± 0.02	40% Pt/C	0	6.95	NO
S_2	0.1 ± 0.01	40% Pt/C	0	4.4	NO
S_3	0.1 ± 0.01	20% Pt/C	0	9.36	NO
S_4	0.1 ± 0.01	40% Pt/C	0.75	11.16	YES
S_5	0.1 ± 0.01	30% Pt/rGO(75)-CB(25)	0	4.41	NO
S_6	0.05 ± 0.005	40% Pt/C	0	2.23	NO

4.2.3 Electrode Fabrication

The appropriate choice of ink support is essential to ensuring optimal performance for low Pt-loaded CLs, as it plays a pivotal role in defining the internal resistance of the fuel cell. Conventionally, two coating methods are employed including the gas diffusion electrode (GDE) and catalyst-coated membrane (CCM). While the former suffers from poor interfacial contact and lower performance, the latter is prone to membrane swelling and CL cracking [126][127]. Various fabrication methods have been proposed such as decal transfer [128][129], blade process, screen [130] and inkjet printing [131], painting, spraying, electrospraying [132], and ultrasonic spray deposition methods [127][133][134], each providing merits and challenges. For example, indirect deposition methods such as blade and decal transfer methods present challenges in ensuring the proper transfer of the deposited layer onto the membrane while striving to maintain comparable performance [131]. Recently, the ultrasonic spray deposition method gained attention as a laboratory-scale device applicable across various support materials. Numerous studies have reported the merits of this method including repeatability, good porosity, homogeneity, and perfect distribution of Pt nanoparticles within the deposited layer [135][132][136].

Previously, the surface microstructure of different CLs prepared using various acting methods including airbrushing, ultrasonic coating, and electrospray is compared by Martin et al. [137]. The uniform surface with small Pt/C agglomerates of size between 50-80 nm is observed for GDEs developed with the ultrasonic coating technique, while the airbrushing method is reported as the least efficient method due to the agglomeration of the particles before spraying [137]. On the other hand, the electrospray method provides enhanced porosity [137]. In addition, Sassin et al. [127] investigated the important factors influencing the ultrasonic coating method and reported the porosity decrease for thicker CLs while the pore size distribution is maintained. Upon coating the CL onto the PEM directly, Yang et al. [138] reported robust contact between PEM and CLs with minimal interfacial resistances as well as minimum cracks due to the formation of hydrophilic channels.

By combining the benefits reported for CCM and ultrasonic deposition method, the anode and cathode CLs are deposited on top of the Nafion® membrane directly via a layer-by-layer method by an automated ultrasonic coating device in this research. The amount

of Pt-loading per layer is evaluated before the preparation of CCMs, and the number of layers is adjusted to reach the desired Pt-loading. The spray bench is composed of a moving nuzzle, vacuum hot plate, and syringe pump purchased from the New Era. The nozzle properties including speed, distance from the substrate, trajectory, stall point, and duration are adjusted from the bench software. To create a well-defined deposition path, the distance between the membrane and nozzle tip is tuned as 20 mm while the use of an acrylic mask with 1 mm offset from each side ensures homogeneous coating on the edges. In addition, the pressure delivered to the pinpoint spray nozzle is adjusted to 1.2 bar ensuring a uniform deposition. The nozzle velocity and flow rate are fixed at 100 mm/min and 0.08 mL/min with a spiral spraying pattern. The nozzle stall duration is adjusted as 40 s for the front side, cathode in this study, and it is 80 s for the back side, anode, avoiding the membrane wrinkling upon removal of the backing film. Due to the variation of the membrane weight through the coating process, the membranes are kept at the temperature of 55°C during the coating procedure and 30 minutes before it, accompanied by 15 minutes of cooling down at room temperature. In addition, the weighing process is repeated 5 times after and before deposition to minimize coating errors for different membranes.

4.2.4 Membrane Electrode Assembly

After preparing all the components, hot-pressing is commonly used to make the cell components a union. Proper assembly techniques are crucial for achieving the desired performance. Improper cell assembly such as excessive compression, causes alteration in pore structure while insufficient compression leads to high ohmic resistances. Various studies investigated the impact of different parameters controlled during hot-pressing including pressure, temperature, and processing time, the most important parameter being the temperature. [139][140]. The appropriate hot-pressing conditions cause the forming of a conductive layer and facilitate embedding the CL into the PEM [140]. Within the results provided in previous studies [140], the MEAs in this work are produced by preheating the coated membrane, fibrous gaskets, and GDLs for 10 min at 134°C, followed by applying 0.5 MPa for another 5 min. The schematic of MEA preparation is shown in

Figure 4.2.

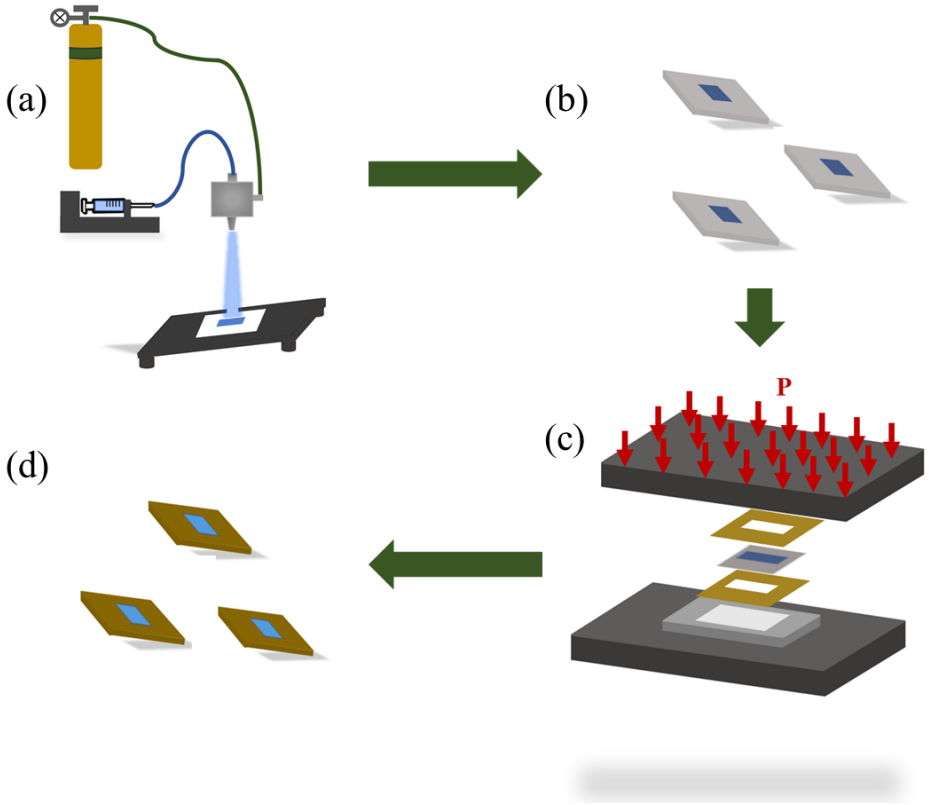

Figure 4.2: The MEA preparation steps, (a) Coating procedure using an automated ultrasonic coating device, (b) The resulting Nafion® membrane after coating, (c) The hot-pressing process, (d) The prepared MEAs

4.3 Electrochemical Characterization Methods

Every MEA mentioned in Table 4.1 is subjected to a thorough in-situ characterization including a performance test, impedance measurement, and cyclic voltammetry.

4.3.1 Linear Sweep Voltammetry (LSV)

The reactants transfer from one electrode to the other through PEM, known as reactants crossover, adversely affect the cell performance and durability, especially the fuel crossover [141]. It reduces the open circuit voltage and fuel efficiency. Moreover, fuel

crossover accelerates the PEM degradation and pinhole formation [142][141]. The rate of fuel crossover is determined by the permeability of the reactants through the PEM, which is influenced by PEM composition, thickness, and operating conditions [143]. The permeability is controlled by diffusivity and solubility and increases with operating temperature.

The linear sweep voltammetry (LSV) is reported to capture the fuel crossover as an in-situ characterization [143]. The potential of the working electrode is varied with a linear potential scan, reaching potentials at which any present hydrogen gas oxidizes. The generated current density reaches limiting values of hundreds of mV and then is related to the hydrogen flux through,

$$J_{H_2} = \frac{i_{lim}}{nF} \tag{4.1}$$

where i_{lim} is the limiting current density in A/cm^2 and J_{H_2} is the hydrogen flux through the PEM with units of mol/cm^2 s.

The fuel crossover is examined at 30°C, ambient pressure, and 100% relative humidity supplying hydrogen and nitrogen at the anode and cathode with the flow rates of 0.05 L/min for both electrodes. The voltage is scanned from 0.04 to 0.8 V with a scan rate of 10 mV/s. The limiting current densities obtained are in the range of 0.6-1.5 mA/cm^2, which is the accepted range of below 2 mA/cm^2 at room temperature.

4.3.2 Cyclic Voltammetry (CV)

Cyclic voltammetry (CV) involves cycling the electrochemical system within two limiting voltages using a triangular potential sweep while recording the current. This technique provides insights into the kinetic and thermodynamic characteristics of electrochemical systems, and the observed peaks during CV relate to specific oxidation and reduction reactions. The in-situ and ex-situ techniques are utilized in three-electrode and two-electrode configurations, respectively. The in-situ method is utilized in this work, in which the anode serves as both counter and reference electrode while the cathode is the working electrode. This test starts with a positive potential scan during which the hydrogen is oxidized on the surface of Pt particles, referred to as the hydrogen desorption peak. This is followed by the reduction of protons through the backward potential sweep which

refers to the hydrogen adsorption region in CV.

In this work, ECSA is determined through the integration of the hydrogen adsorption region area as demonstrated in Figure 4.3 in an H_2/N_2 environment avoiding the complications associated with the CO-stripping method. Previous research has highlighted concerns about CV artifacts, particularly the concentration cell effect originating from the hydrogen evolution reaction (HER), which introduces faradic current at low potentials (below 0.1 V) [144][64]. However, ECSA values merely serve as indicators for quantifying the available Pt surface area and are obtained in similar conditions for all MEAs, ensuring a proper basis for comparison in this study. Moreover, Prass et al. [144] recently outlined the efficiency of this method for ECSA determination in the presence of pure Pt/C catalysts.

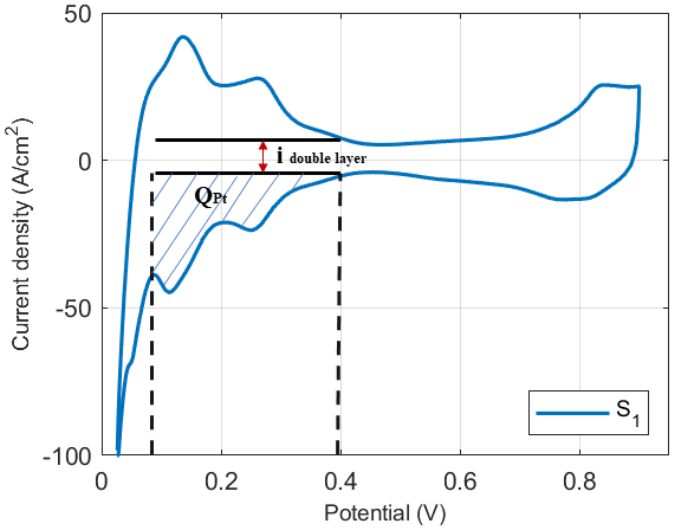

Figure 4.3: The shaded charge density region used for ECSA calculation for S_1

In this research, the relative performance loss is evaluated in-situ at 30°C, ambient pressure, and 100% relative humidity supplying hydrogen and nitrogen at the anode and cathode with the flow rate of 0.125 and 0.05 L/min, respectively. The cell is cycled 40 times within 0.025 and 0.9 V at a scan rate of 400 mV/s, before which the voltage is cycled 60 times for stabilization. The choice of a high scan rate enhances the distinction of electrochemical processes for low pt-loaded cells [144]. Moreover, due to the shorter dwell period at high potentials (above 0.85 V), high scan rates hinder the carbon corrosion of the catalyst support [144]. The ECSA is determined by the integration of H-adsorption charge within 0.08-0.4 V considering the required specific charge for the reduction of a

monolayer of protons on the Pt surface while excluding the charge transfer related to the double layer charging [144]. The overall equation for deriving the ECSA is,

$$ECSA\left(\frac{m^2}{g}\right) = \frac{Q}{\theta\, L_{Pt}} \tag{4.2}$$

where Q is the integrated charge obtained from CV in mC/cm^2, θ is the charge associated with the hydrogen coverage on the Pt surface with the value of 210 μC/cm^2, and L_{Pt} is the Pt loading within the cathode electrode. The capacitive current for charging and discharging of the electrical double layer and the hydrogen crossover current should be extracted to avoid overestimating the catalytic activity. This current is demonstrated as $i_{\text{double layer}}$ in Figure 4.3, and is dependent on the scan rate and the specific capacitance of the electrode double layer, which is determined based on platinum and carbon support specific capacitance.

4.3.3 Polarization Curve

The polarization curve is introduced in section 1.2.2.2. Fuel cell performance tests are performed using a Scribner Series 850e. The cell current is measured at distinctive points within open circuit voltage (OCV) and 0.3 V supplying air and hydrogen from the cathode and anode with 0.125 and 0.5 L/min, averaging each point for 60 s. Each performance test is performed 5 times, and the error bars represent the deviation of the tests. Before the performance test, each MEA is conditioned by voltage cycling with a square wave between 0.3 and 0.7 V each for 60 seconds continuing for a total duration of 20 h, ensuring a stable current density measurement. Before the performance evaluation, a cathode recovery is implemented keeping the cell at 40°C and 100% relative humidity in the H_2/air environment for an hour to recover reversible losses.

4.3.4 Electrochemical Impedance Spectroscopy (EIS)

Electrochemical impedance spectroscopy (EIS) is a commonly employed technique for in-situ characterization of PEMFCs. It offers the capability to separate and analyze

the various electrochemical processes occurring within the fuel cell. The processes are associated with distinct characteristic time constants, and EIS allows individual examination of the processes [11]. Different electrochemical processes occur within various frequency domains. For instance, the interfacial resistance of cell components and ionic resistances are measured through the high-frequency intercept in the Nyquist plot [11]. The charge transfer resistance is obtained from the small frequencies, while the lowest frequencies represent the mass transfer resistances. The results obtained are then analyzed considering different circuit elements [11].

Impedance spectra are collected at 0.7 V supplying hydrogen and air from the anode and cathode at the flow rate of 0.125 L/min. Each EIS spectrum is captured for the interval of 10000-0.1 Hz with 10 frequencies per decade, while the amplitude of AC perturbation is kept at 5% of the DC load. Before data acquisition, the cell is kept at 0.7 V potential for 10 min for stabilizing the system.

The data fitting process was performed using ZView® software, provided by Scribner Associates, USA. EIS spectra are analyzed by fitting the results to a Randle cell as shown in Figure 4.4, which comprises an ohmic resistance (R_{ohm}) in series with a constant phase element (CPE). In parallel, it includes a charge transfer resistance (R_{CT}) [145]. Since the EIS spectra are obtained at ohmic polarization, the effect of mass transport resistance is neglected. The constant phase element is fitted as,

$$Z_{CPE} = \frac{1}{(j\omega)^n Q} \tag{4.3}$$

where n and Q are the fitting parameters, and n varies between 0.7 and 1 with values closer to 1 representing an ideal capacitor [11].

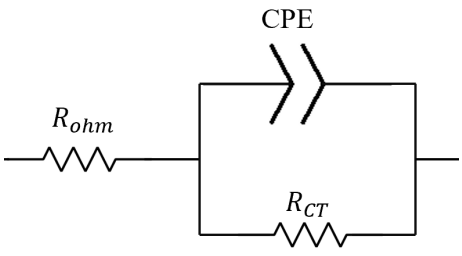

Figure 4.4: The circuit model used for EIS fitting

4.4 Results

In this section, the primary aim is to evaluate the impact of CL morphology and operating conditions on cell performance. Recently, many studies evaluated the effect of CL thickness and Pt loading [5][66]. To realize the same CL thickness for low Pt-loaded MEAs, the use of a lower Pt/C weight ratio coupled with the addition of bare carbon particles is necessary, which results in higher carbon loading and enhances the CL thickness [5][77][64]. However, it remains unclear whether the lower Pt/C ratio or the amount of Pt-loading is the predominant factor contributing to the reported increased transport resistances in low Pt-loaded CLs. To understand the impact of different catalyst morphological properties, CL characteristics including the amount of Pt loading, Pt/C weight percentage, and the bare carbon loading in the cathode CL are analyzed separately in this work. In addition, this study is complemented by the preparation of a catalyst containing Pt nanoparticles on a hybrid support comprising carbon black (CB) and reduced graphene oxide (rGO), which allows exploring the effect of support material. While readers are referred to Ref. [114] for detailed information on the synthesis of the electrocatalyst using a microwave-assisted reduction procedure, the optimal ratio of 75 CB/ 25 rGo is considered here based on the findings of Kaplan et al. [114].

The LSV test is conducted to ensure the proper cell assembly and determine the fuel flux through the PEM before in-situ characterizations. The LSV results for S_1 and S_6 samples with different Pt-loadings and maximum thickness deviation are shown in Figure 4.5. The current usually stabilizes with either a constant or linearly increasing slope as the electrode potential increases. A constant current, independent of electrode potential, suggests a fuel cell with infinite electrical resistance, while a linearly increasing current indicates finite resistance due to internal short-circuiting. The electrical resistance of the cell can be approximated by calculating the slope of the voltage against the current plot. As shown in Figure 4.5, the current against voltage represents infinite electrical resistance without any short circuit issues. The values of limiting current obtained are 0.489 and 1.52 mA/cm^2, providing the fuel crossover flux of 2.4×10^{-9} and 7.6×10^{-9} mol/cm^2 s using equation 4.1, which represents the hydrogen crossover characteristics of high-quality pristine MEAs.

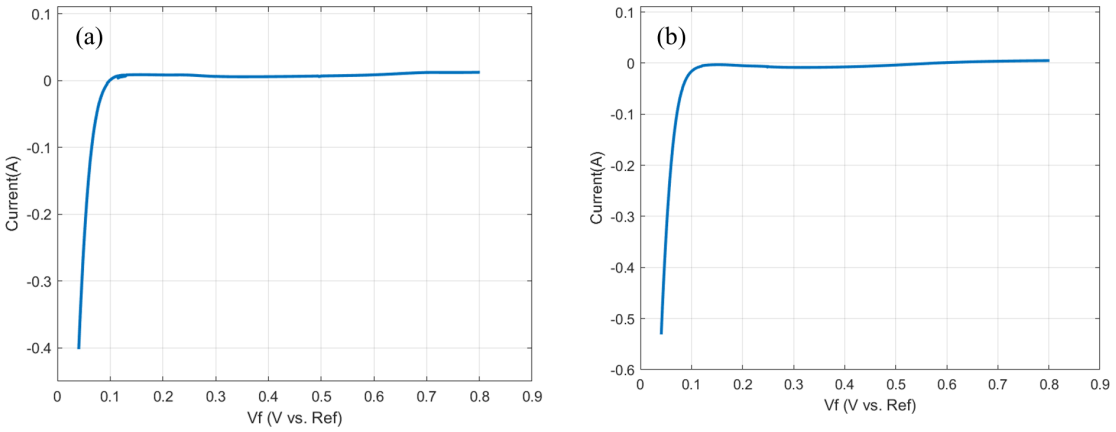

Figure 4.5: The Linear sweep voltammogram for evaluating the rate of fuel crossover for (a) S_1, (b) S_6

The CL thickness, as determined through model results for all samples, is documented in Table 4.1. In addition, scanning electron microscopy (SEM) is used to evaluate the actual CL thickness in different Pt-loaded samples, the result of which is shown in Figure 4.6. For SEM imaging of MEAs, an SEM-FEG Zeiss Leo Supra 35VP was utilized with two electron high tension (EHT) voltages including 3 kV for secondary electron imaging and 10 kV for backscatter electron imaging. The 8 mm working distance was optimized for focus and depth of field. MEAs were cross-sectionally cut after immersion in liquid nitrogen to facilitate a controlled breakdown at the midpoint, enabling a detailed examination of MEA surface morphology, membrane, and catalyst thicknesses.

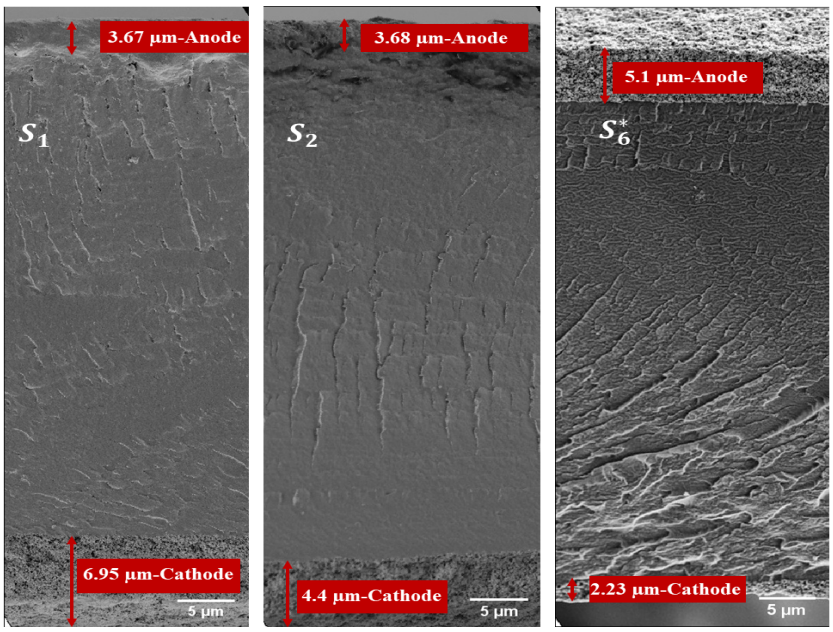

Figure 4.6: The SEM pictures of CL cross-section and the measured thickness for (a) S_1, (b) S_2, and (c) S_6^*

In Figure 4.6, the orientation is such that the bottom of all samples corresponds to the cathode side, while the upper electrode represents the anode. To assess the CL thickness, new samples are created, and cross-sections are examined using SEM imaging. Given the adjusted Pt-loading of 0.1 mg/cm^2 for the anode, the CL thickness is expected to exhibit similar values. Specifically, the anode CL thickness is approximately 3.6 µm for S_1 and S_2, while it reaches 5.1 µm in S_6^*. Notably, S_6^* deviates slightly from S_6 due to a different anode Pt-loading of 0.15 mg/cm^2, and it is denoted with a star. Despite this deviation, a comparison between Table 4.1 and Figure 4.6 reveals good agreement between the CL thickness evaluated by the model and that measured from SEM images.

For samples sharing the same Pt-loading of 0.1 mg/cm^2 but differing in CL characteristics, Figure 4.7 illustrates the CL thickness. The highest CL thickness is observed in the diluted sample S_4. An almost consistent CL thickness was noted for the anode electrode, where the Pt-loading is 0.1 mg/cm^2.

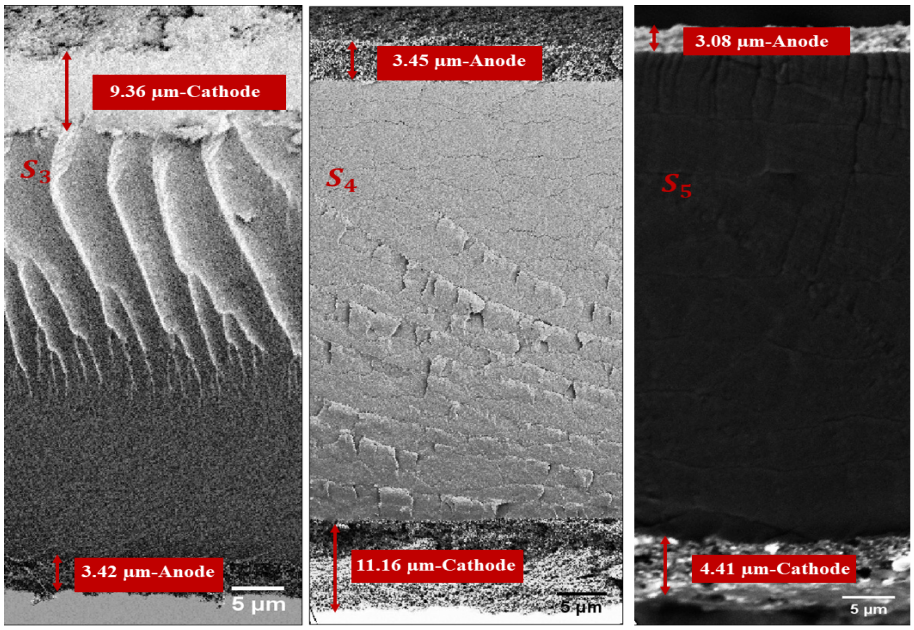

Figure 4.7: The SEM pictures of CL cross-section and the measured thickness for (a) S_3, (b) S_4, and (c) S_5

4.4.1 Operating Conditions

The impact of operating conditions is studied based on the evaluation of polarization curves, which are compared across different relative humidity ratios and temperatures

and demonstrated for S_2 in Figure 4.8. The SEM image represented for S_5 is taken in backscatter electron imaging mode.

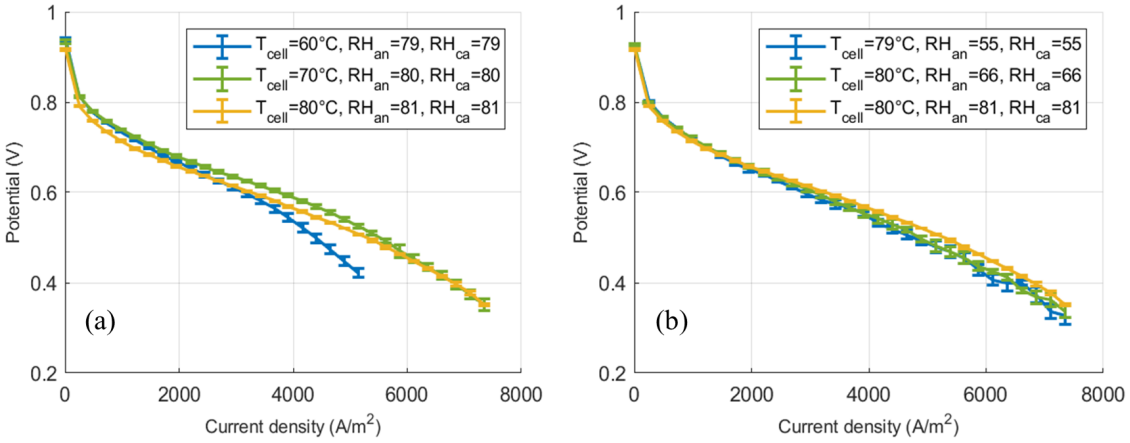

Figure 4.8: The S_2 sample performance comparison for (a) various operating temperatures, (b) different relative humidity ratios

Suitable cell performance is achieved using a relative humidity of 80% for an operating temperature of 80ºC. Noteworthy, the higher RH values are intentionally avoided to control water generation, especially for high Pt-loaded samples following modeling results explained in chapter 2. In addition, the performance for different operating temperatures slightly differs, considering a consistent relative humidity. Increasing the temperature enhances the activity losses and cathodic overpotential, which in turn causes OCV reduction. However, enhanced temperatures effectively prevent liquid water generation and enhance performance in the limiting current density region. Therefore, the suitable overall beginning-of-life (BOL) performance is attained at a cell temperature of 70°C, with a relative humidity of 80%. The small variations in RH values, mainly attributed to slight fluctuations in cell temperature, are neglected due to their minimal effect. The temperature and relative humidity comparison are further demonstrated for S_6 in Figure 4.9.

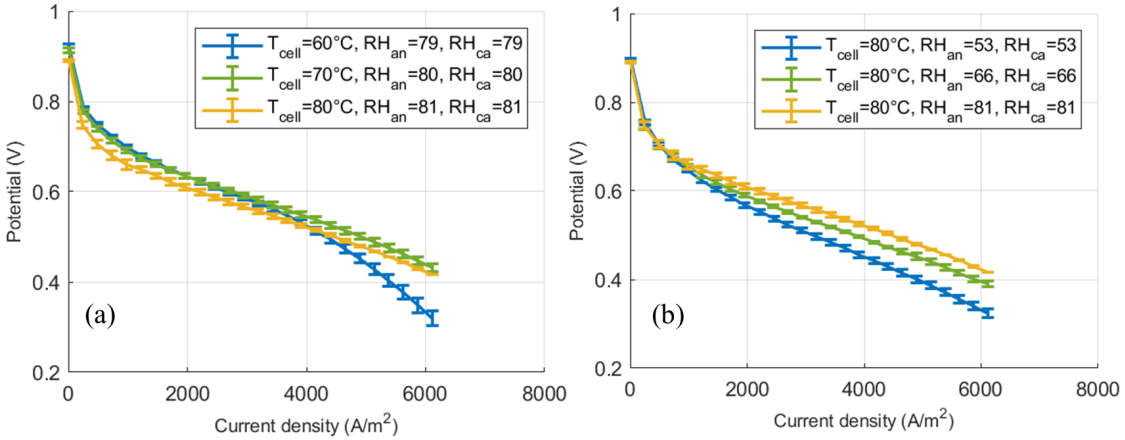

Figure 4.9: The S_6 sample performance comparison for (a) various operating temperatures, (b) different relative humidity ratios

Comparing the results obtained for different Pt-loadings, the effect of operating temperature is consistent within different Pt-loaded samples as demonstrated in Figures 4.8 and 4.9. Comparing these two figures for different relative humidity ratios, however, the effect of relative humidity is more intense for low Pt-loaded sample, S_6. Since low Pt-loaded samples comprise thinner CL, a higher humidity content is required at the inlet to ensure sufficient proton conductivity of the membrane for the thinner CL due to lower water content in the membrane and ionomer phases following the results of Ref. [10].

High operating pressures ensure elevated performance as demonstrated in Figure 4.10 for S_2 with an operating temperature of 80°C and 80% relative humidity; however, the pressure regulation is managed by the Scribner backpressure unit and is not stable for long-term operation in our study. The enhanced performance upon pressure increase was previously observed in section 2.3.3.

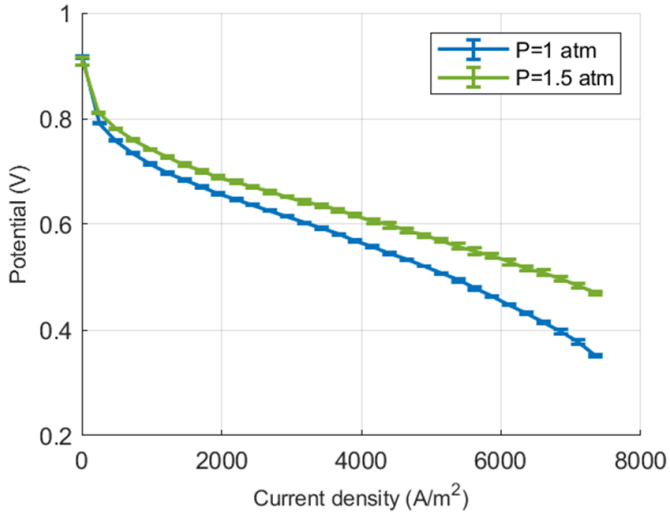

Figure 4.10: The S_6 sample performance comparison for various operating pressures

As a result, the temperature of 70ºC, relative humidity of 80% for both cathode and anode electrodes, and atmospheric pressure are selected for continuing the performance evaluations of samples with different CL characteristics.

4.4.2 Catalyst Layer Characteristics

It is imperative to first evaluate the experimental methods used in this thesis in terms of repeatability. To this end, a series of tests are conducted by preparing two samples with identical characteristics and subsequently comparing their cell performance under the same operating conditions. Cell performance for various samples, which are prepared using separate catalyst inks, is presented in Figure 4.11. Notably, the slight performance discrepancy observed between two sets of samples, all featuring identical CL characteristics, serves as a robust validation of the repeatability inherent in both the CCM and catalyst ink fabrication processes. Moreover, the observed deviation in cell performances, as illustrated in Figure 4.11, could be attributed to the weighing error either in Pt-loading during the CCM process or materials amount in catalyst ink preparation.

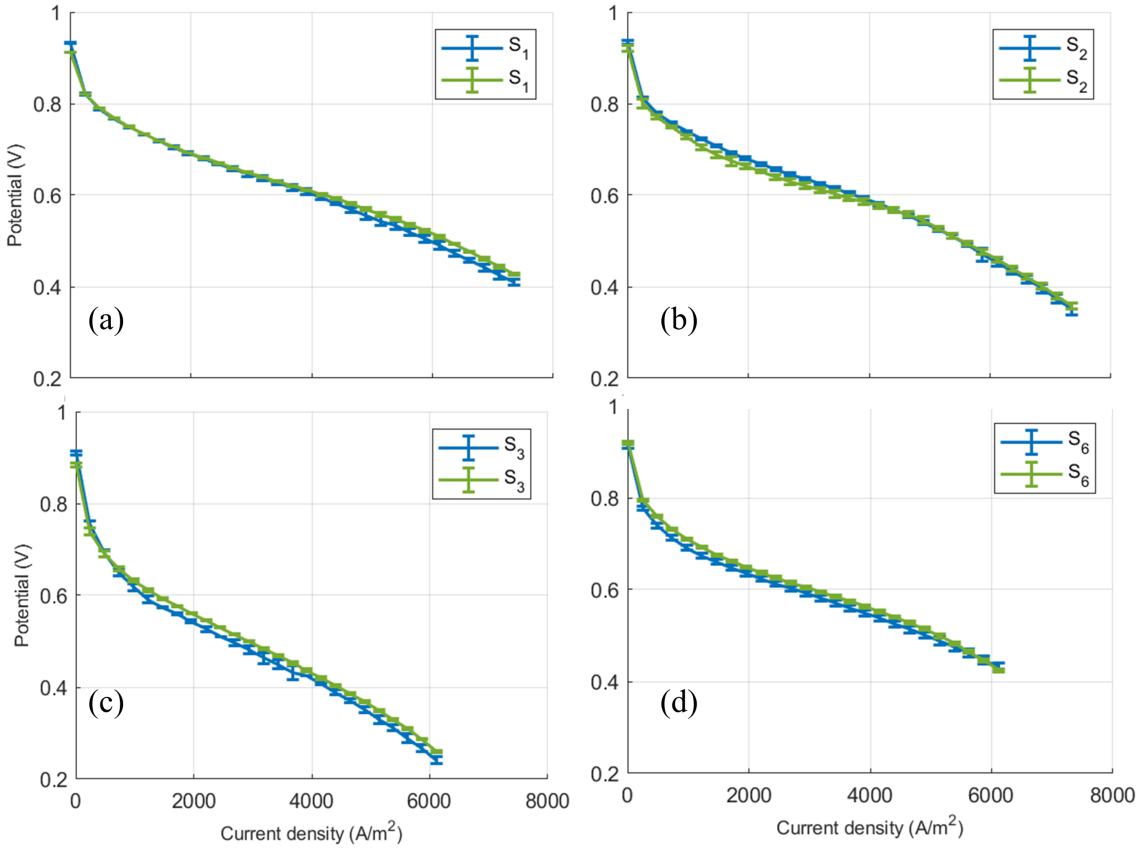

Figure 4.11: The cell performance comparison for two samples of the same CL features, (a) S_1 and (b) S_2, (c) S_3, (d) S_6

Figure 4.12 demonstrates the cell performance of samples with varying Pt-loadings. As depicted, cell performance exhibits improvements with increasing Pt-loading. Notably, a significant performance enhancement is observed between S_2 and S_6 with Pt-loadings of 0.1 and 0.05 mg/cm^2, respectively. However, exceeding the Pt-loading of 0.1 mg/cm^2 yields only marginal performance gains. Consequently, cell performance of S_2 and S_1 correlates closely with more distinct differences in the limiting current density region, which originated from heightened oxygen transport resistances in low Pt-loaded samples [77]. While there is a recognized positive trend with increasing the cathodic loading, an intermediate loading has been verified to strike a balance among transport resistances, catalytic activity, and electronic potential losses [25][77]. In this study, this medium Pt-loading is identified as 0.1 mg/cm^2, selected for further CL morphology analysis.

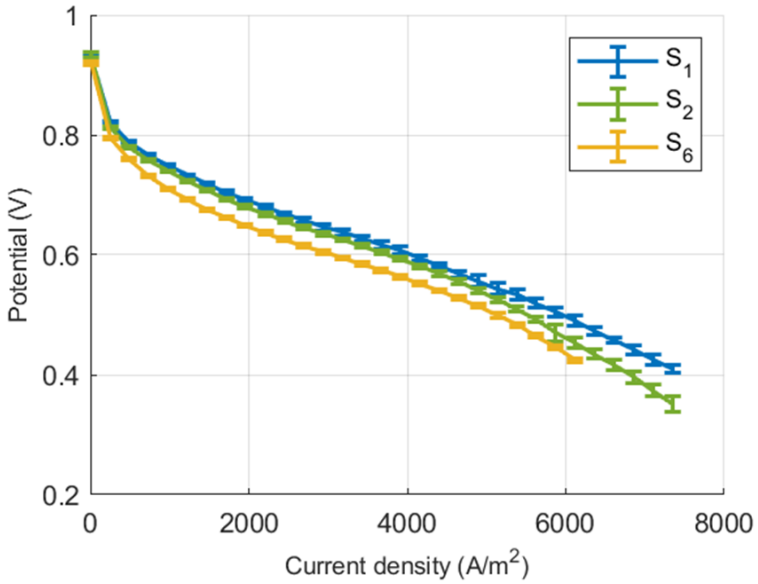

Figure 4.12: The cell performance comparison for different Pt-loaded samples of the same CL features, S_1, S_2, and S_6

In Figure 4.13, the cell performance for CLs featuring various characteristics but a constant Pt-loading of 0.1 mg/cm^2 is presented, allowing the individual examination of CL features. While previous studies have discussed increased oxygen transport resistances and subsequent reduction in cell performance resulting from the addition of bare carbon particles into the CL [5][25][77], the independent effect of adding bare carbon particles has not been investigated. Modifications in Pt/C ratio and bare carbon mass fractions were usually simultaneous [5][25], which has obscured a clear understanding of CL morphology. Besides the different methods for diluting the catalyst, the simple approach used in this work provides insights into the impact of each parameter separately. Interestingly, the overall performance of the diluted sample, S_4, is improved compared to the S_2. The same catalytic activity is observed across a range of low to intermediate current densities, signifying equivalent cathodic loading in both samples. However, the improved cell performance is evident for the limiting current density region, primarily influenced by transport resistances. In this context, Wang et al. [66] previously detailed heightened catalyst dispersion upon CL doping with bare carbon particles, accompanied by increased CL porosity quantified through SEM imaging. This improved catalyst dispersion correlates with a notable 12% increase in ECSA for S_4 compared to S_2. This increment effectively counters the elevated electronic resistances caused by the increased CL thickness, leading to enhanced Pt utilization, and consequently elevated cell perfor-

mance.

A decreasing trend is identified for the remaining two samples, S_5 and S_3, with Pt/C ratios of 30 and 20%, respectively. The hybrid sample, S_5, exhibits higher transport resistances, resulting in lower limiting current densities. Conversely, the commercial catalyst with a 20% Pt/C ratio displays a similar polarization trend with S_2 but with reduced catalyst activity. The reason behind the decreased cell performance of S_3 may lie in the elevated carbon loading and proportionally increased ionomer loading in the CL, which impedes oxygen transfer. Additionally, the formation of a thick ionomer layer and suppressed electronic conductivity, particularly in S_5, further compromise performance. Furthermore, the increased CL thickness resulting from the use of lower Pt/C ratios amplifies the electronic potential losses.

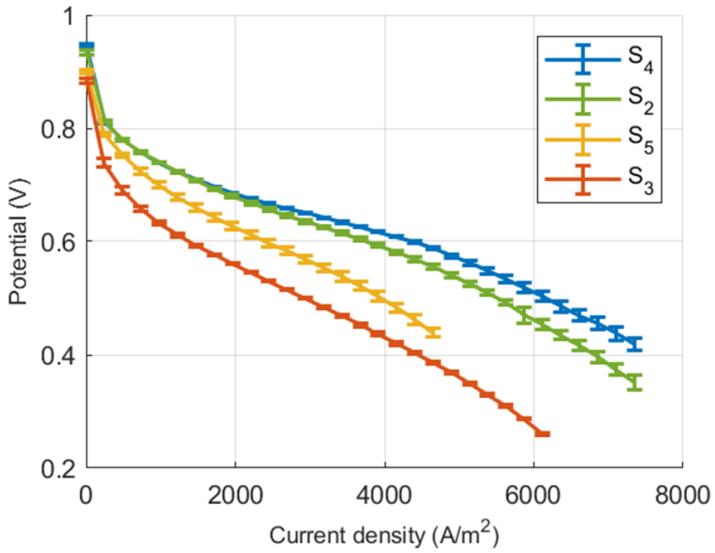

Figure 4.13: The cell performance comparison for same Pt-loading and different CL features samples, S_2, S_3, S_4, and S_5

The CV comparison for different Pt-loadings which is depicted in Figure 4.14 manifests a significant increase in electrode current density with increasing Pt-loading. The ECSA values of 25.54, 33.53, and 37.9 m^2/g are derived for three distinct Pt-loaded samples, S_1, S_2, and S_6, respectively. However, the ECSA values are higher for low-loaded cathodes, resulting in greater Pt utilization for low CL loadings. Consistent with this study, Wang et al. [66] associated higher ECSA values with low-loaded samples, while Harzer et al. [64] attributed the higher observed ECSA values in their study to the use of lower Pt/C weight ratios. The authors reported a more homogeneous dispersion of Pt nanoparticles on the carbon support surface upon the use of smaller Pt/C ratios from the

same supplier, as confirmed by Transmission Electron Microscopy (TEM) images [64]. However, consistent Pt/C ratios are utilized for developing different Pt-loaded samples for which cyclic voltammograms are demonstrated in Figure 4.14. The employed layer-by-layer approach in preparing the CCMs in this work, leads to a lower degree of Pt agglomeration in low pt-loaded samples, resulting in a lower average particle size, and eventually higher ECSA values.

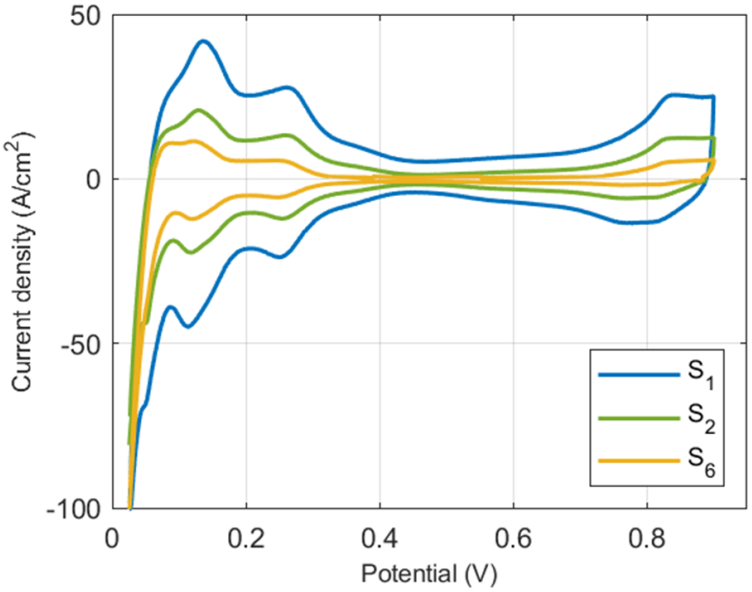

Figure 4.14: The cathode CV comparison for different loaded samples, S_1, S_2, and S_6

Figure 4.15a provides a comparison of the BOL Nyquist curves for various Pt-loaded samples. The ohmic resistances for both S_2 and S_6 are measured at 10 mΩ, while the ohmic resistance for S_1 is slightly higher at 17 mΩ. This slight increase in the ohmic resistance could be attributed to the different CL thicknesses in these samples, with S_1 having the thicker catalyst. Furthermore, the evolution of charge transfer resistance with Pt-loading confirms the higher transport resistance observed in low Pt-loaded samples, which originates from the limited availability of active species in the CL. Specifically, the charge transfer resistances increased for S_2 and S_6 with values of 14.3 and 15.5 mΩ in comparison to S_1 with a value of 9.9 mΩ, showing the charge transfer increase of 44% and 56% for S_2 and S_6, respectively. This reflects the challenges associated with charge transfer and electrochemical reactions in low Pt-loaded CLs.

The BOL EIS comparisons for samples with different CL compositions having the same Pt-loading are demonstrated in Figure 4.15b. The observed trend in this figure agrees

well with the performance results shown in Figure 4.13, where S_4 represents superior performance and S_3 exhibits the worst one. Furthermore, the ohmic resistances of S_2 and S_4 indicate similar values with slight variations. However, S_5 shows a 63% increase with a value of 16.3 mΩ, and S_3 shows a 28% increase with a value of 12.8 mΩ in ohmic resistance, highlighting the effect of carbon support material and carbon loading on the ohmic resistances and its dependence on the Pt/C ratio. This may stem from the increased oxygen transport resistance associated with thicker ionomer film since higher carbon loading in the CL is proportionally related to the ionomer loading. On the other hand, the charge transfer resistance is strongly dependent on the CL features. The diluted sample, S_4, represents a 39% decrease in comparison to the base sample, S_2, showing the decreased oxygen transport resistances despite the increased CL thickness of this sample. In contrast, S_5 and S_3 exhibit charge transfer resistance with the values of 20.5 and 30.1 mΩ, respectively, demonstrating the significant impact of Pt/C ratio on charge transfer resistance and, consequently, the overall electrochemical performance.

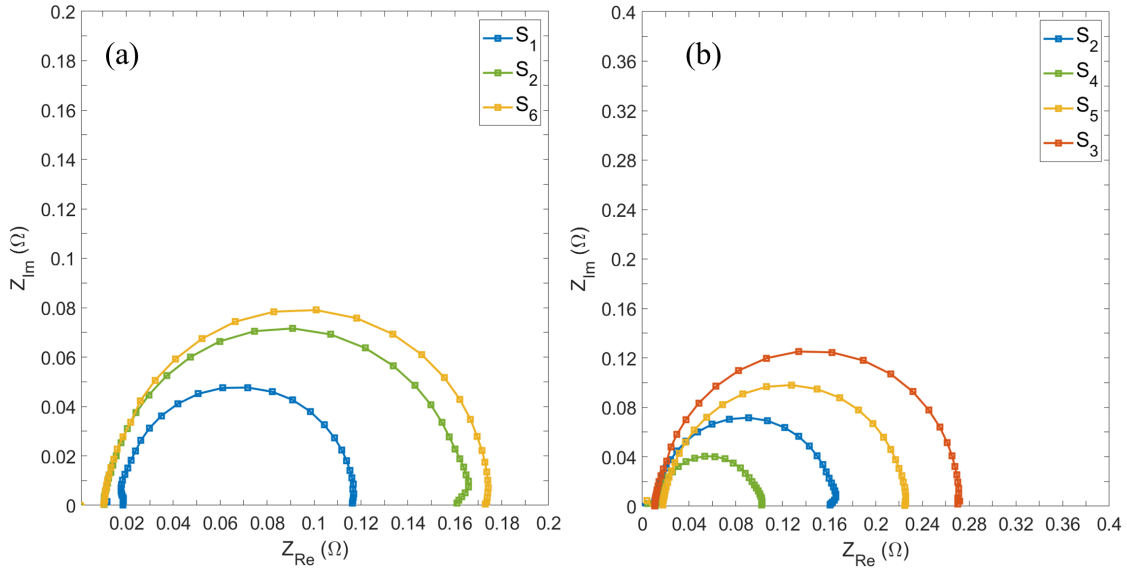

Figure 4.15: BOL Nyquist curves for (a) Different Pt-loaded samples, (b) Samples with different CL features and a constant Pt-loading

4.5 Summary and Conclusion

Determining the effect of CL characteristics, as the most critical component of PEMFCs, is imperative to thoroughly understand the transport resistances and optimize the cell performance under a variety of operating conditions. To this end, different MEAs with various CL characteristics including CL thickness, Pt-loading, bare carbon content, Pt/C ratio, and carbon support materials are fabricated. To minimize the interfacial resistance between cell components, the catalyst is directly deposited on the surface of the membrane using the ultrasonic coating method aligned with the hot plate surface. The direct deposition of CL on PEM causes membrane swelling and the formation of cracks in the PEM, however, the ultrasonic coating method ensures a homogeneous Pt coating, and optimizes flow rate and the stall duration, which assists the better drying during the coating process. In addition, the use of an ultrasonic nozzle hinders the formation of particle agglomeration before coating which increases the ECSA values and Pt utilization. The samples are electrochemically characterized and the following main conclusions are obtained.

- Comparing the cell performance for different operating conditions, higher operating temperature increases the catalytic activity, while moderate values are considered for relative humidity to ensure appropriate proton conductivity. The impact of operating temperature is consistent for various samples with different Pt-loadings and CL characteristics, with 70°C representing the best performance in comparison to 80 and 60°C.

- The effect of relative humidity is more intense for low Pt-loaded samples primarily due to the reduced CL thickness and lower water adsorption capability of these samples within the electrolyte phase. To mitigate the losses due to higher ionic resistance, higher relative humidity values are preferable for low Pt-loaded samples.

- The repeatability of the CCM fabrication method is evaluated by preparing samples of the same components with a time difference, during which all the processes need to be repeated. The results obtained from all samples ensure the repeatability of the ultrasonic coating method due to minor variations of the polarization curve for

various cases.

- The enhanced cathodic Pt-loading increases the cell performance, however, the performance slightly deviates between Pt-loading of 0.2 and 0.1 mg/cm^2. The increased CL thickness of higher Pt-loaded samples causes increased ohmic resistances which counteracts the effect of higher catalytic activity. Moreover, higher ECSA values are observed for the low Pt-loaded samples representing lower levels of agglomeration in these samples. The layer-by-layer deposition method utilized in this work avoids the agglomeration of nanoparticles, especially for low Pt-loaded samples with thin CL.

- The lower Pt/C ratios cause a performance decrease, while the addition of bare carbon content enhances the catalyst utilization and eventually increases the cell performance. The use of a hybrid catalyst with 30% Pt/C ratio shows superior performance against the commercial 20% catalyst, However, the cell suffers from the increased mass transport losses in the limiting current density region.

- The carbon diluted sample represents superior performance for the same Pt-loading and even for the higher Pt-loading of 0.2 mg/cm^2, which stems from the lower ohmic resistances and increased proton conductivity in the CL. The bare carbon used in this sample facilitates adhering the Pt particles and ionomer content, thus providing more activated reaction sites.

Chapter 5

DURABILITY EVALUATION OF LOW PLATINUM LOADED PEM FUEL CELLS

5.1 Introduction

Achieving improved durability levels is required for automotive proton exchange membrane fuel cells (PEMFCs) as a viable alternative for transportation and internal combustion engines. The U.S. Department of Energy (DOE) provides durability targets for automotive PEMFCs ensuring long-term performance and stability. The current target is achieving a durability of 8,000 hours of operation time, meaning 15000 miles of driving, with less than 10% performance degradation [60]. Meeting the specified durability targets is challenging since automotive PEMFCs operate under real-world operating conditions, which include dynamic load cycles, frequent start-stop operations, exposure to road vibrations and shocks, and operation in a wide range of weather conditions, from hot and dry environments to sub-freezing temperatures. Enhancing the durability of automotive fuel cell systems without sacrificing performance and cost presents a significant challenge, which originally stems from the inherent trade-off relationships among these factors.

While the impact of electrode degradation and carbon corrosion (CC) on the catalyst layer (CL) microstructure has been extensively studied in the literature, there is a need for further investigation into the reverse relationship. The CL is a complex, heterogeneous structure composed of multiple components with different functionalities, and the electrochemical reaction takes place at the interfaces of the components. Therefore, an experimental framework is required to systematically analyze the influence of these design

variables on CL degradation.

In this thesis research, the focus is to evaluate the impact of CL morphology on electrode degradation using porous, low Pt-loaded PEM fuel cells fabricated with the CCM approach and an ultrasonic spray deposition device. The MEAs are fabricated to have uniform Pt distribution and controlled CL thickness and vary in terms of several CL features, including Pt/C ratio, Pt-loading, CL thickness, bare carbon content, and the type of carbon support material as described in the chapter 4. This allows a systematic examination of each CL characteristic influence on electrode degradation. To assess electrode degradation, two distinct accelerated stress tests (ASTs) are employed to simulate the Pt-dissolution and carbon corrosion degradation mechanisms. The extent of performance loss is evaluated using methods such as polarization curves, electrochemical surface area (ECSA) calculations, and electrochemical impedance spectroscopy (EIS) measurements. This comprehensive experimental framework provides valuable insights into the factors affecting electrode degradation in low Pt-loaded PEMFCs.

The rest of this chapter is organized as follows. First, an introduction section provides an overview of electrode degradation, along with a literature review on the subject. The subsequent section presents experimental findings, including performance data, ECSA analysis, and the evolution of EIS results. The results obtained are further explored and analyzed through a modeling study in section 5.2.2.2. This section outlines the modeling domain and validates numerical results using experimental data. Section 5.3 introduces the topic of corrosion and details the results of the investigations, while the summary of the notable conclusion of this section is provided in section 5.4.

5.2 Electrode Durability

The commercialization of fuel cells faces many challenges in terms of cost and durability. PEMFCs, although primarily tested under ideal conditions with high Pt loadings, have shown durability subjected to more challenging conditions such as long-term operation, extreme weather conditions, and high fuel utilization. However, it is important to note that the durability of these devices is notably influenced by the catalyst Pt content.

The PEMFC degradation is classified into three main mechanisms including mechanical, chemical, and electrochemical mechanisms, and is quantified by the voltage loss per hour of cell operation. Through the mechanical degradation, the creation of local stresses caused by intense operating conditions leads to pinhole formation and membrane deformations, which accelerates the fuel crossover and degrades the cell performance [146]. Moreover, membrane dehydration occurs upon exposure to high operating temperatures and is categorized as thermal degradation, a subcategory for mechanical degradation [146]. Chemical degradation is the main degradation mechanism for PEM and stems from the alternation of reaction between carbon, fluorine, and oxygen during fuel cell operation [147]. The intense degradation experienced by PEMFCs relates to electrochemical degradation concerning the CL, mainly CCL due to the existence of the oxidant and high potentials, which is quantified by the loss of electrocatalyst [148].

under PEMFC operating conditions, the Pt nanoparticles undergo continuous potential fluctuations leading to structural transitions between metallic and oxidized states. These alterations cause two primary degradation mechanisms including the coarsening and oxidation of particles [148]. Through the coarsening mechanism, the Pt nanoparticles either migrate through the carbon support and agglomerate with neighbor particles or dissolve under high potentials, greater than 0.85 V, followed by precipitation onto other Pt particles and formation of larger Pt particles. Since tiny Pt particles are unstable under such voltages, the Pt^{+2} ions diffuse through the PEM resulting in the formation of the Pt-band far from the CL. Dissolved metal cations are replaced with protons in PEM resulting in a significant ionic resistance [149] as well as a reduction in the oxygen diffusivity near the catalyst surfaces, due to physicochemical modifications of the cathode ionomer [150]. The Ostwald ripening includes the same processes including Pt dissolution and redepositing to larger Pt particles, all of which result in catalyst surface area decrease over time [151]. The literature review points towards the potential coexistence of multiple particle growth mechanisms in PEMFCs, which is influenced by various factors such as the crystal size of the fresh Pt/C particles, utilized electrode potential [64][152], temperature, humidity [70], presence of oxygen, and the extent of graphitization of the carbon support [149].

The CL microstructure modifications due to Pt-dissolution have been widely investigated in the literature. Researchers often conduct accelerated stress tests (AST) following

the protocols set by the U.S. Department of Energy (DOE), allowing the investigation of material durability within a relatively short period. Zhang et al. [153] identified Pt agglomeration as the main growth mechanism conducting experiments with different acceleration conditions, varying the voltage scanning range. Moreover, Rinaldo et al. [154] conducted theoretical studies on electrochemical and chemical Pt dissolution and quantified three different regions of potential region contributors. During high-potential region which includes severe ECSA loss, the oxides are the abundant species [154]. Furthermore, Bi et al. [155] studied Pt solubility detailing the linear relationship between operating temperature and accelerated Pt dissolution.

The effect of Pt-loading on the performance of PEMFCs is investigated through experimental and numerical studies [5][4][25]. However, a better understanding of the performance losses during aging processes is necessary to optimize the CL for long-term operation. In this regard, Harzer et al. [64] exposed two different Pt-loaded samples to different potential cycling profiles. The authors reported higher ECSA loss for low Pt-loaded samples, the origin of which could be either the low Pt content or small Pt/C ratio [64]. Moreover, Sgarbi et al. [156] investigated the impact of Pt-loading on the degradation behavior of the cell, producing CLs with different Pt-loadings and thus CL thicknesses. The authors reported rapid performance loss during the first 48 hours of operation for lower Pt-loaded samples (0.05 mg/cm^2), while the ECSA and performance loss decelerate during the rest of the operation [156]. Moreover, the authors reported quite the same overall ECSA loss for all the samples [156]. On the other hand, higher CL thickness is reported to contribute to desirable cell durability by elevated water adsorption and lower ionic resistance [10]. Furthermore, Schneider et al. [25] investigated the impact of CL thickness by varying the Pt and bare carbon loading as well as the Pt/C ratio. Authors reported elevated ECSA degradation during 10000 hours of AST for a low Pt-loaded sample (0.1 mg/cm^2), while proposing a relative dependency of CL thickness on the Pt mass loss into the membrane, with a trend of higher relative Pt mass loss for thin electrodes [25]. However, the same Pt relative loss of 10 % is observed for samples of different Pt loadings and a forced CL thickness of around 17 μm.

The literature offers conflicting results regarding the effects of Pt-loading, Pt/C ratio, and CL thickness on the Pt-dissolution mechanism. For instance, Wang et al. [66] suggested the positive impact of dilution ratio on cell durability, whereas Schneider et al.

[25] reported accelerated ECSA loss for diluted samples compared to undiluted ones of the same Pt-loadings. Moreover, Harzer et al. [64] observed lower durability for low Pt-loaded samples (0.1 mg/cm^2) while using lower Pt/C ratios for these samples, which could impact the validity of their conclusion. Given these discrepancies in the current research, there is a compelling need for further investigation to provide clarity on the influence of these parameters on electrode degradation. .

5.2.1 Methods

5.2.1.1 Experimental Methods

The development of low Pt-loaded samples, the experimental methods, electrochemical characterization techniques, and the beginning-of-life (BOL) performance of the samples are provided in chapter 4, while the focus of the current chapter is to investigate the durability of low Pt-loaded samples described in Table 4.1.

Two different ASTs are performed to evaluate the pt-dissolution and carbon corrosion degradation mechanisms. For Pt-dissolution a total of 10000 cycles are conducted cycling the voltage between 0.6-1 V at a scan rate of 40 mV/s, using the cell temperature of 70°C and 80% relative humidity. The anode and cathode are supplied with hydrogen and air with flow rates of 0.125 and 0.25 L/min, respectively. While one has the choice of using either nitrogen or air at the cathode during Pt-dissolution ASTs, the use of air provides more realistic results taking into account the generation of water and heat [67]. In addition, the relative humidity significantly affects the performance loss during Pt-dissolution AST, with values above 80% having severe contribution [70]. The polarization curves, EIS, and CVs are collected before the AST as well as at specified intervals including 1000, 3000, 5000, and 10000 cycles.

5.2.1.2 Numerical Methods

The modeling domain is projected on a single surface including the serpentine channels for both cathode and anode electrodes with channel and rib widths of 1 mm, as

demonstrated in Figure 5.1. The complete list of governing equations is presented in section 2.2.2.

Figure 5.1: The modeling domain of interest for validations against experimental data presented in this thesis

The numerical model is implemented in the commercial finite element software COMSOL Multiphysics. A quadrangular mesh is employed to discretize the governing equations over the channels and the ribs with 3268 linear elements and 60k DOF. The solution is obtained using a fully coupled solver with Newton iterations and a direct PARDISO solver to solve the linear system of equations.

5.2.2 Results

The results obtained during the experimental investigation of CL characteristics are presented in the section. Moreover, the degradation of MEAs is further confirmed through the P3D model described in section 5.2.1.

5.2.2.1 Experimental Results

Electrochemically Active Surface Area (ECSA) Evolution: The degradation of the Pt surface area throughout the AST protocol is assessed by recording the CVs after each ag-

ing stage. This degradation is illustrated for S_1 in Figure 5.2, highlighting the ECSA fade with the increasing number of voltage cycles. As demonstrated in Figure 5a, there is a notable difference between BOL and end-of-life (EOL) plots, while cyclic voltammograms remain closely related for intermediary stages.

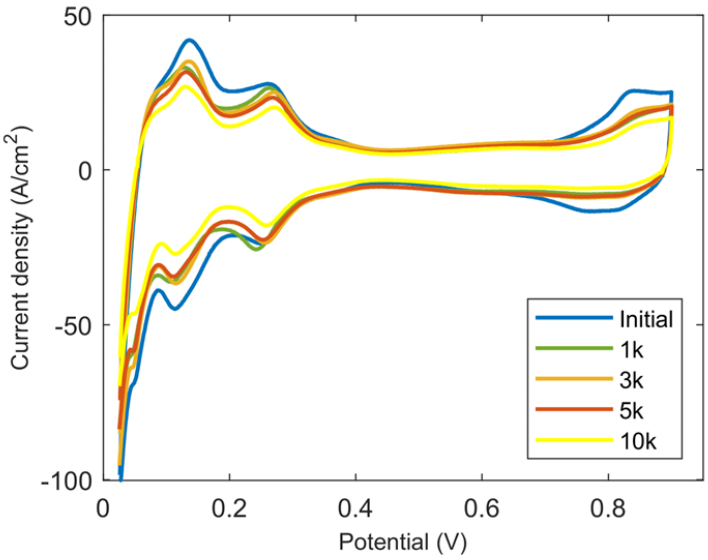

Figure 5.2: Cathode cyclic voltammograms during Pt-dissolution AST demonstrated for S_1

The continuous voltage fluctuations within the applied AST protocol result in recurring surface alternations between metallic and oxidized states. This transition promotes the Ostwald ripening, coalescence of Pt nanoparticles, and their migration into the ionomer phase. Moreover, this mechanism triggers electrochemical degradation through the local re-deposition of modest Pt nanoparticles into the bigger ones. Consequently, the catalyst surface area diminishes throughout the AST, simulating the long-term operation of the fuel cell system. This degradation mechanism is more dominant for smaller Pt nanoparticles, due to the lower stability attributed to the large atomic ratio of low-coordination Pt atoms [151].

To assess the degradation of different Pt-loaded samples, the normalized ECSA evolution during the voltage cycling AST is shown in Figure 5.3a for S_1, S_2, and S_6. Consistent ECSA decay trends are observed for different cathodic Pt-loadings. Initially, the AST leads to rapid ECSA loss within the first 3000 voltage cycles which is more pronounced for S_6 with Pt-loading of 0.05 mg/cm^2. Subsequently, a moderate ECSA loss occurs, followed by a gradual stabilization for the remaining voltage cycles. This results

in a total loss of 17, 29, and 54% of the initial ECSA after 10000 voltage cycles in the H_2/air environment, providing valuable insights for real-time fuel cell operation. The AST protocol promotes the Pt-dissolution from smaller particles at high potentials and their redeposition to the larger ones at low potentials while some Pt^{2+} ions diffuse through the ionomer phase [151][25]. The latter results in the formation of a Pt-band far from the electrode, primarily dependent on the diffusion length defined as the distance to the membrane interface. Since only the Pt nanoparticles at the CL-membrane interface migrate through the membrane, the size of the Pt-band remains independent of the Pt loading and is solely determined by the interface area. Acknowledging the independence of the Pt depletion zone from Pt-loading and CL thickness, Schneider et al. [25] observed higher Pt mass loss relative to the BOL loading for low Pt-loaded samples, where the depletion zone constitutes a larger fraction of the overall CL thickness.

The effect of studied CL characteristics on the ECSA evolution during the AST is elucidated in Figure 5.3b. These samples exhibit distinct CL features while sharing the same Pt-loading, as outlined in Table 4.1, with S_2 serving as the baseline for ECSA fade comparison. As illustrated in this figure, the diluted sample with an additional bare carbon mass fraction, S_4, outperforms all the samples with a Pt-loading of 0.1 mg/cm^2, demonstrating an 11% decrease of the initial ECSA over time. The increased CL thickness in the diluted sample leads to a lower relative Pt loss to the membrane, resulting in a significant reduction in ECSA fade. This finding agrees with the results reported by Schneider et al. [25], who observed decreased relative Pt loss with increasing CL thickness, ultimately resulting in less Pt relative loss for the diluted sample with the forced higher CL thickness. Moreover, Schneider et al. [25] quantified smaller particle growth in diluted samples, with a trend of lower EOL particle size with increasing the dilution rate, indicating a reduced contribution to local re-deposition to larger particles. These observations are consistent with the observed enhanced ECSA evolution for thicker low Pt-loaded samples and introduce a hypothesis of a higher anchoring effect within TPB particles upon the addition of bare carbon particles.

The second place among 0.1 mg/cm^2 samples belongs to the hybrid sample, experiencing a 25% reduction of the initial ECSA. Due to the thermodynamic instability of the commercial carbon support (carbon black) under fuel cell operating conditions, replacing this support material with stable oxides gained significant attention [151]. Moreover, im-

proving the anchoring between the carbon support and Pt nanoparticles is critical at high potentials to prevent Pt coalescence.

The poorest performing sample is S_3, fabricated with a 20% Pt/C weight ratio. Although S_3 exhibits a similar ECSA degradation trend to S_2, it experiences a more substantial degradation, with a 35% loss of the initial ECSA compared to a 29% reduction observed in S_2. This discrepancy may stem from the use of smaller Pt nanoparticles in lower Pt/C weight ratios, leading to pronounced Ostwald ripening and reduced stability against dissolution. In this case, the instability of smaller Pt nanoparticles offsets the benefits of the higher CL thickness, ultimately resulting in the decreased stability of S_3 compared to S_2.

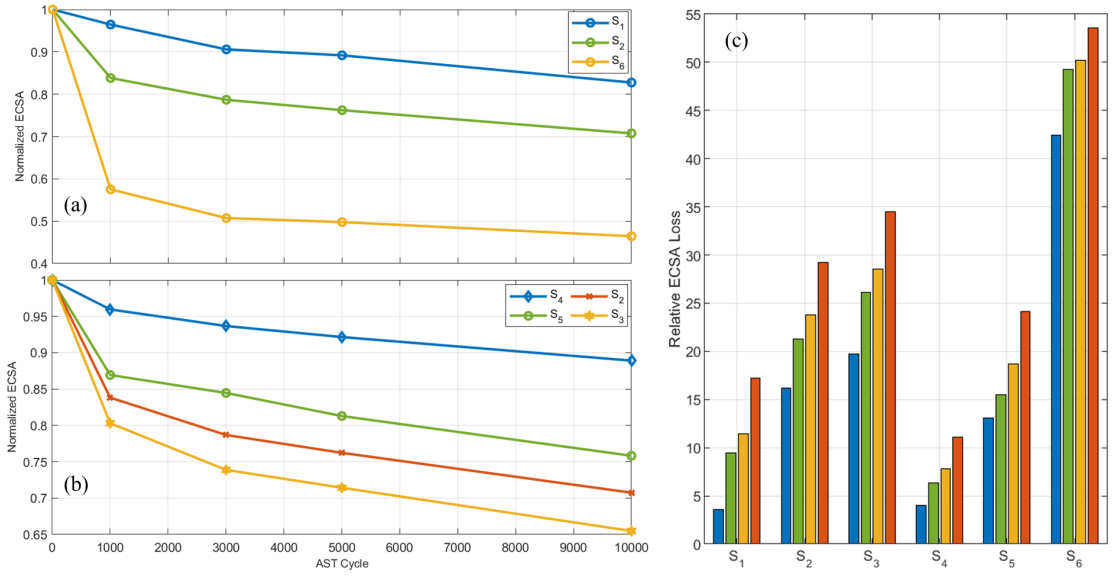

Figure 5.3: ECSA evolution for (a) different Pt-loaded CLs, (b) samples with different CL characteristics and same Pt-loading, and (c) relative ECSA loss for all the studied MEAs

The relative ECSA loss during AST voltage cycles for all the fabricated MEAs is illustrated in Figure 5.3c, showcasing the S_4 and S_6 as the most and least stable samples against degradation. Among the same Pt-loaded samples, however, the S_3 shows the worst stability. For all the samples except S_1 and S_4, the first 1000 voltage cycles account for more than half of the ECSA loss while this number is 17 and 36% for S_1 and S_4, respectively.

Performance Loss: The impact of CL morphology on the BOL and EOL performance, as well as stability against the applied AST at different stages for all fabricated samples are represented in Figure 5.4 while the BOL performance of all these samples is compared

in Figures 4.12 and 4.13. Comparing the results of Figure 5.4, the impact of Pt-loading on electrode degradation is evaluated. During the initial 1000 voltage cycles, rapid performance degradation is observed for S_2 and S_6 in comparison to S_1, a trend previously observed by the relative ECSA losses depicted in Figure 5.3c. The gradual stabilization of ECSA loss after 3000 voltage cycles is discernible in the performance curves. Monitoring the potential loss at a current density of 300 mA/cm^2, the overall potential loss of 0.054, 0.056, and 0.07 V is determined for S_1, S_2, and S_6, respectively, which aligns well with the ECSA fade and loss of catalytic activity. In addition, an increased overpotential is identified after 10000 voltage cycles for all samples, particularly S_6 with the smallest Pt-loading. The Pt-dissolution AST is performed in an H_2/air environment, and variations in performance through the limiting current density region partially resulted from the generation of liquid water and increased oxygen diffusion resistances, proportionally related to the Pt-loading through Faraday's law.

The comparison of the performance degradation among samples with varying CL features but a constant Pt-loading of 0.1 mg/cm^2 is presented in Figure 5.4. During the first 1000 voltage cycles, S_3 undergoes severe performance degradation, consistent with the 20% relative ECSA loss observed in this range and shown in Figure 5.3c. S_3 is prepared with a 20% commercial Pt/C ratio, which is known to yield smaller mean particle sizes compared to the base case prepared with a 40% Pt/C ratio [75][64]. The Pt-dissolution mechanism predominantly affects small initial Pt nanoparticle size, while Pt coalescence is evident across all samples, with its prevalence increasing as particle size decreases [157]. Moreover, the dominant degradation mechanism, Pt-dissolution, accounts for the majority of ECSA losses [157]. Consistently, Darab et al. [75] described the independence of electrode degradation operating with pure oxygen, while significant carbon loading impact was observed performing in diluted oxygen, leading to enhanced degradation for smaller Pt/C ratios. Therefore, the accelerated performance degradation of S_3 compared to S_2 lies in the differences in the materials and the respective nanoparticle sizes. Furthermore, as shown in Figure 5.4, the most unstable samples, S_3 and S_6, represent higher voltage variations in the limiting current density region, as indicated by the extended error bars.

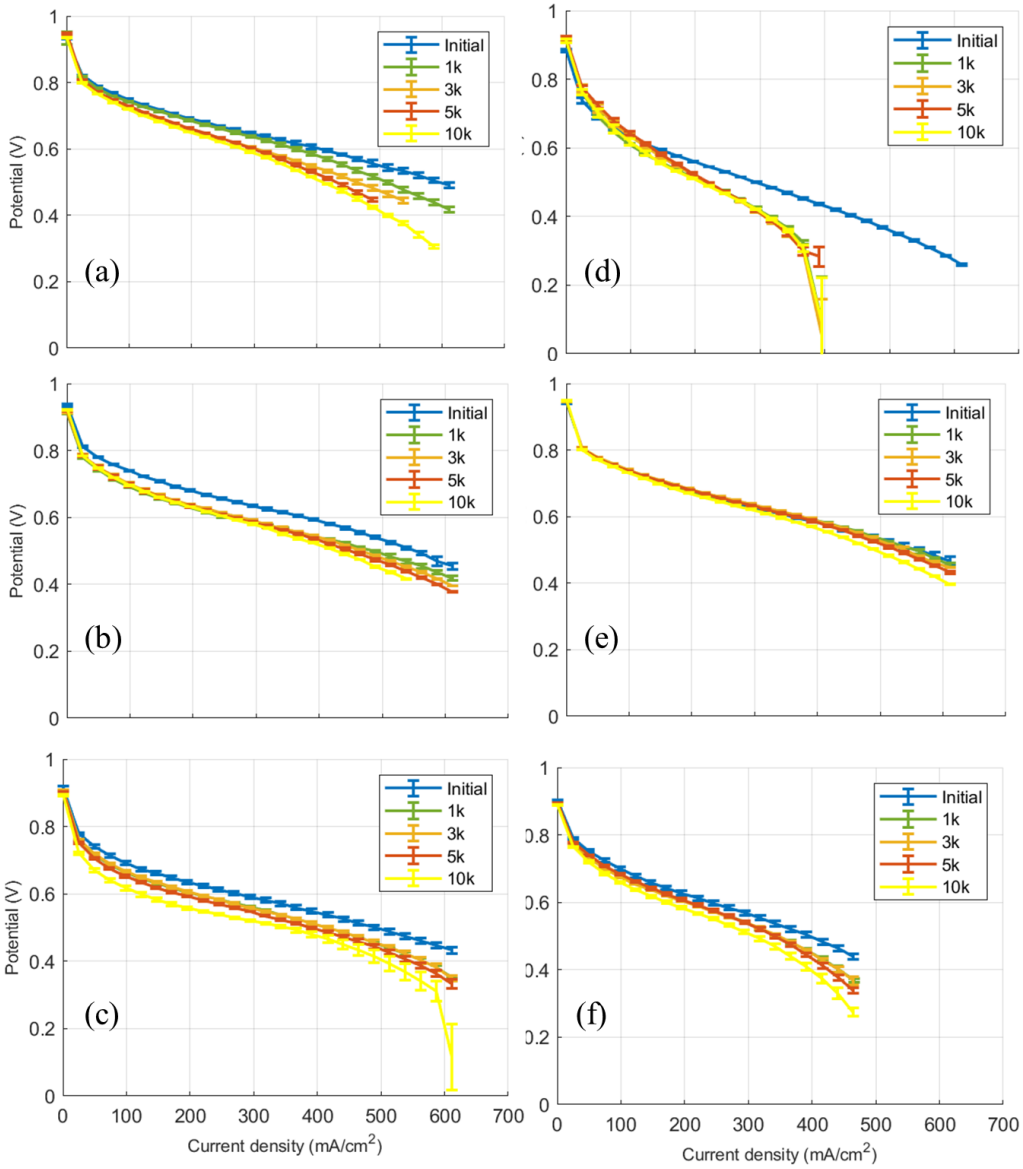

Figure 5.4: The performance curves at all stages during the Pt-dissolution AST for (a) S_1, (b) S_2, (c) S_6, (d) S_3, (e) S_4, (f) S_5

The diluted sample, which initially displayed superior performance, exhibits only marginal degradation through the course of AST voltage cycling. The ECSA fade during the AST is measured as 11%, surpassing even that of the high Pt-loaded sample, S_1. Two plausible hypotheses rationalize the observed stability of this sample throughout the voltage cycling. Firstly, the addition of bare carbon particles enhances the anchoring effect between the Pt nanoparticles and the carbon support, thereby suppressing Pt migration and the formation of a Pt-band within the ionomer phase. Schneider et al. [25] reported smaller relative Pt loss for diluted samples, mirroring the Pt loss observed in high Pt-loaded samples with 0.4 mg/cm^2. Moreover, the authors observed lower Pt concentration

in the membrane depletion zone. Secondly, the diluted sample contains a higher amount of carbon and subsequently ionomer loading. The increase in ionomer loading is proportional to the carbon loading, using a consistent I/C ratio of 1, which results in a thicker CL. A relative dependence of Pt mass loss into the membrane on the CL thickness is previously established, with thinner CL layers causing higher relative Pt loss [25].

As demonstrated in Figure 5.4e, the hybrid sample, S_5, exhibits improved stability subjected to the AST protocol, despite demonstrating decreased BOL performance as shown in Figure 4.13. The use of graphene oxide in this sample leads to better Pt nanoparticle attachment to the carbon support. However, it increases the electronic potential losses as observed in Figure 4.15 and eventually reduces BOL performance. Comparing the polarization curves of S_2 and S_5, the enhanced stability of the hybrid catalyst during the initial 1000 voltage cycles of the AST is evident through a smaller voltage deviation, which is attributed to decreased ECSA loss. The same trend of rapid performance loss across 1000 voltage cycles is discernible in this sample with smaller overall percentages.

Impedance Evolution: Figure 5.5 demonstrates the EIS results of S_6 at different stages of the applied Pt-dissolution mechanism, collected at a potential of 0.7 V. Although the ohmic resistances (low-frequency resistance) slightly modify through the AST voltage cycling with a value changing from 10 to 12.8 mΩ for the BOL and EOL EIS, there are significant fluctuations in the charge transfer resistance (high-frequency resistance). As expected, the charge transfer resistance initially increases by 71% within the first 1000 voltage cycles and continues to rise by 87%, 125%, and 141% in subsequent cycles. This increase in charge transfer resistance directly correlates with the performance deviation observed in Figure 5.4. The AST promotes Pt coalescence, the formation of larger Pt particles, and the loss of active species, all of which contribute to elevated charge transfer resistances and the resulting performance decline in the final state. Importantly, the lack of an increase in ohmic resistance, which is often associated with a decrease in CL porosity [158], suggests that the applied AST primarily affects Pt-related phenomena rather than carbon corrosion, which would accelerate CL morphological alterations.

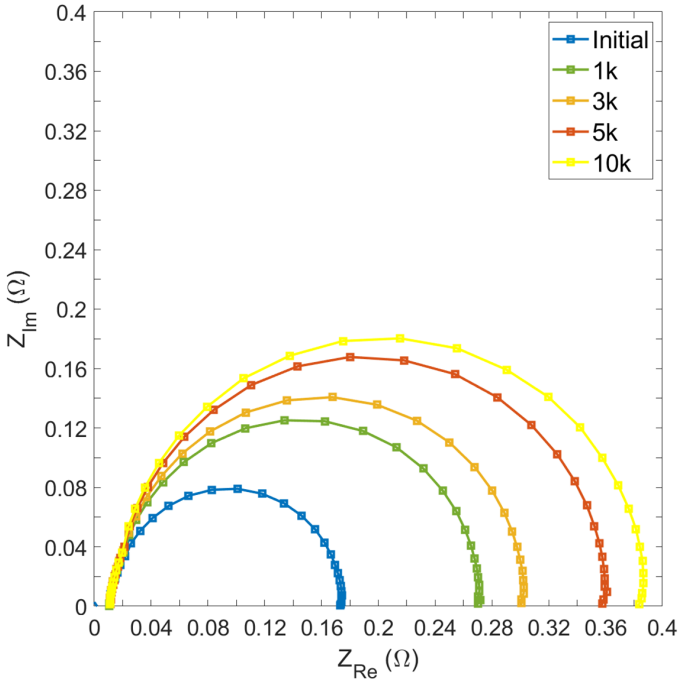

Figure 5.5: Nyquist curves during Pt-dissolution AST demonstrated for S_6

5.2.2.2 Numerical Results

The numerical model is first evaluated for the experimental results provided in chapter 4 for all the studied samples. The CL parameters are adjusted with the CL characteristics of the samples and are provided in Table 5.1. In addition, the ECSA values associated with each sample, derived through cyclic voltammetry provided in section 5.2.2.1, are utilized. A comparison of model results and experiments for the BOL performance of all samples is presented in Figure 5.6. As demonstrated in this figure, the molding results show good agreement with the experimental findings. However, the diluted sample, S_4, represents increased catalytic activity and superior performance in the activation region which is not captured by the model.

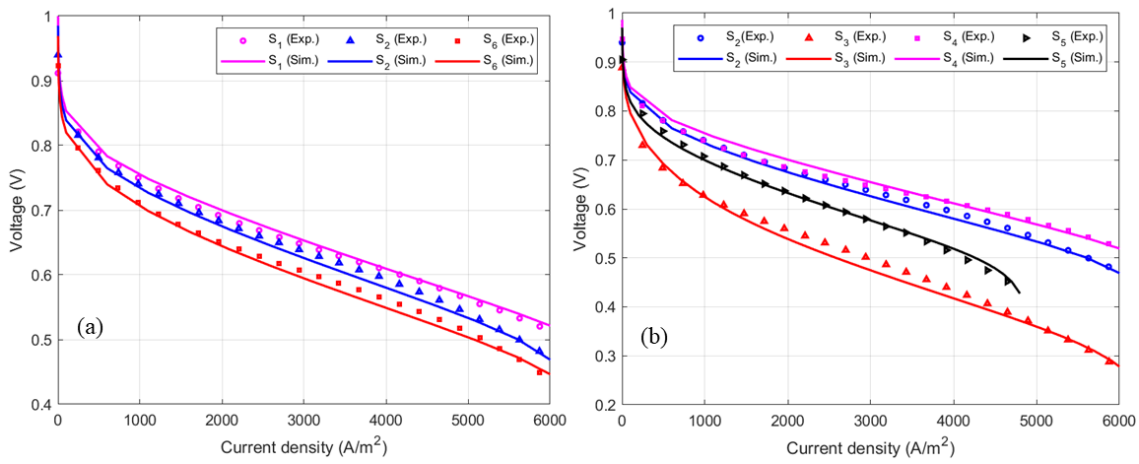

Figure 5.6: The BOL performance comparison of the model results with the presented experimental data for (a) different Pt-loaded samples, (b) samples with the same Pt-loading of 0.1 mg/cm^2 and different CL characteristics

Through the use of ECSA values at the EOL condition of the cell, the EOL performance of all samples is compared considering a 30% loss of Pt-loading. Upon voltage excursions, the Pt nanoparticles usually migrate through the CL and create a Pt-band in the membrane close to the interface of the CL-membrane. Since the Pt-band is observed in the physical characterization of this work (not shown) and previous studies concerning the degradation [25], the Pt-loading loss approach is utilized for further studying the EOL performance of the samples. The results obtained are provided in Figure 5.7.

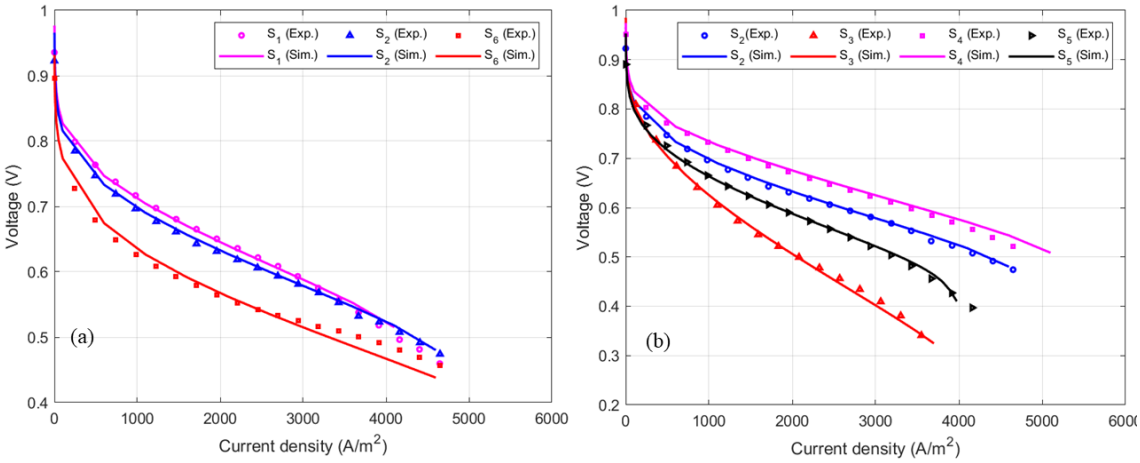

Figure 5.7: The EOL performance comparison of the model results with the presented experimental data for (a) different Pt-loaded samples, (b) samples with the same Pt-loading of 0.1 mg/cm^2 and different CL characteristics

The parameter values presented in Table 5.1 indicate that the loss of ECSA and Pt-loading alone is insufficient to replicate the EOL experimental data. In this context, the

values of parameters k_1 and k_2 are adjusted to 12, 15, accounting for the increased oxygen transport resistances in degraded cells. Numerous studies have extensively examined the impact of electrode degradation on various transport resistances, including protonic conductivity, ionic resistances, and reaction kinetics, as referenced in previous works [159][160]. During the Pt-dissolution AST, moreover, small Pt nanoparticles tend to agglomerate into larger particles or precipitate onto larger Pt particles. This phenomenon introduces uncertainty regarding the use of the BOL CL parameters, as various CL parameters, such as Pt radii, carbon radii, and kinetic parameters, can change during AST. The model results demonstrate that modifications to the CL parameters are necessary to accurately represent the EOL performance.

Table 5.1: CL parameters used for comparing the model results and presented experimental data

Samples	**S_1**	**S_2**	**S_3**	**S_4**	**S_5**	**S_6**
BOL-ECSA	26	35	66	38	27	40
EOL-ECSA	22	25	43	34	20	18
α_{ca}	0.745	0.745	0.645	0.745	0.7	0.745
BOL-r_C (nm)	46	46	46	35	46	35
EOL-r_C (nm)	56	56	56	52	60	50

5.3 Carbon Corrosion

Carbon-based materials have been widely utilized in various fuel cell components including the catalyst supports for the electrode, microporous layers (MPLs), and gas diffusion layers (GDLs). The cathode catalysts are particularly susceptible to degradation in the oxidizing conditions of the fuel cell cathode [158], where water serves as the primary oxidant. The electrocatalyst corrosion of the cathodic carbon black support materials during startup/shutdown potential cycling causes severe performance loss due to loss of ECSA, decreased electrical conductivity of the support [28], and increased mass transport losses through substantial alterations of pore morphology [62][161]. The carbon oxidation becomes pronounced under specific conditions, such as local fuel starvation or flooding of the anode CL, for which the reverse-current decay mechanism was initially

proposed for better understanding [62]. Upon resuming typical fuel cell operation after a shutdown period and exposing the anode to hydrogen, an H_2/air interface develops, which propagates through the anode and replaces the existing gases. The coexistence of gases with different equilibrium potentials at the front section of the same electrode leads to local reverse current, causing the interfacial potential difference at the cathode electrode to substantially exceed 1 V, with theoretical estimations ranging from 1.4 V to 1.6 V [62]. The elevated potential promotes detachment and agglomeration of the Pt nanoparticles, further reducing ECSA [161].

Carbon support corrosion is found to significantly affect fuel cell degradation [65][162], and is linked to an increase in ohmic resistance, a decrease in ECSA, and alterations of CL morphology, including thinning, cavities, and reduced porosity [163]. Reiser et al. [62] proposed the H_2/air interface at the anode causes high potentials at the cathode resulting in carbon corrosion and Pt particle agglomeration. Furthermore, the thinning of CL is observed upon carbon corrosion alongside the ECSA reduction, which is more pronounced under fuel starvation conditions [164]. Young et al. [164] characterized structural degradation in the CL caused by carbon corrosion, leading to thinner cathode catalyst layers and reduced effective platinum surface area. The impact of inlet relative humidity ratios on the carbon corrosion mechanism is investigated by Xiao et al. [165], while Lim et al. [14] detailed the severe dependence of corrosion on relative humidity investigating the combined effect of operating temperature and RH ratio on degradation.

There is a notable absence of research on the effect of CL features on the carbon corrosion mechanism. Therefore, the durability of samples explained in Table 4.1 against carbon corrosion AST are presented in this section.

5.3.1 Experimental Methods

Carbon corrosion AST is adopted from a protocol proposed by the DOE, where the cell is operated for 5000 cycles within 1 and 1.5 V with a scan rate of 500 mV/s. The cell is in a driven mode using an external potentiostat, in the H_2/N_2 atmosphere. The cell temperature is adjusted at 70°C with 80% relative humidity and flow rates of 0.125 and 0.25 L/min for the anode and cathode, respectively. The polarization curves and CVs are

collected at the beginning and end of life (BOL and EOL).

5.3.2 Results

The performance degradation of the MEAs exposed to the carbon corrosion AST is presented in Figure 5.8 alongside their respective BOL polarization curves. Considering previous results concerning the Pt-dissolution AST, the hybrid sample is omitted from this analysis due to poor BOL performance. The impact of Pt-loading on the carbon corrosion mechanism is examined by comparing the degradation of S_1, S_2, and S_6 presented in Figure 5.8. In addition, the potential loss resulting from the applied AST is displayed in Figure 5.8e for all samples, while a comparison of the BOL performance was previously provided in Figures 4.12 and 4.13. Since carbon is unstable under typical cathode potentials in the presence of Pt particles and water, carbon corrosion degradation is plausible across the full potential range of cathode operation [28]. Moreover, the rate of carbon loss and CO_2 evolution are influenced by Pt content and particle size distribution [161], with higher Pt-loading accelerating the corrosion mechanism. Comparing the results of this study, S_6 with Pt-loading of 0.05 mg/cm^2, exhibits the best performance against carbon corrosion, followed by S_2 and S_1, respectively. Moreover, the voltage loss is measured as 0.13, 0.12, and 0.09 V at a current density of 300 mA/cm^2 for these samples, demonstrating the reverse relationship between cell durability against carbon corrosion and Pt-loading. Furthermore, the carbon corrosion mechanism is a two-step reaction, where Pt determines the reaction rate and accelerates the reaction kinetics.

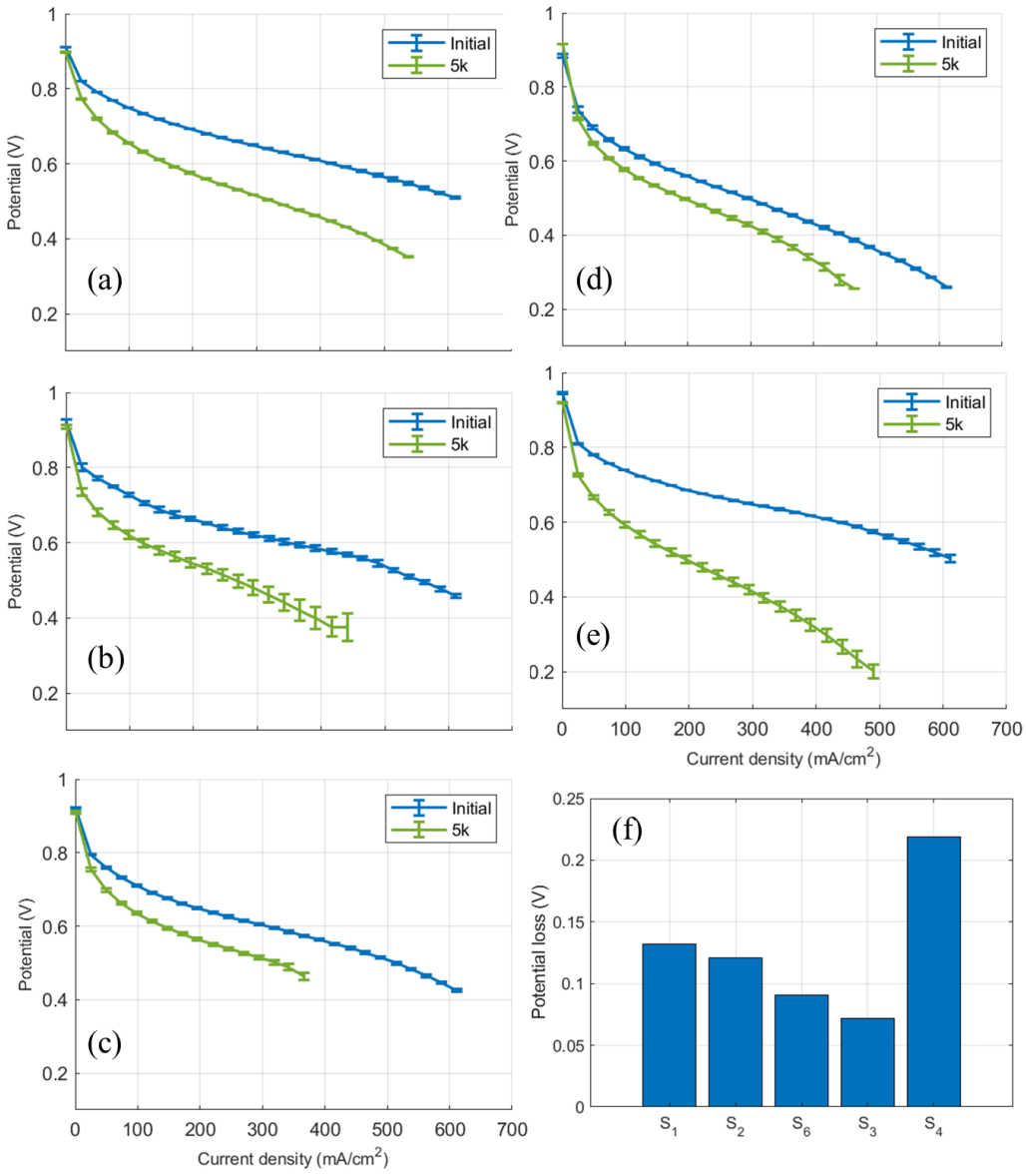

Figure 5.8: The BOL and EOL performance curves during the carbon corrosion AST for (a) S_1, (b) S_2, (c) S_6, (d) S_3, (e) S_4, (f) Voltage variations of the corroded samples

The performance degradation of S_3, developed with a 20% Pt/C ratio catalyst, is demonstrated in Figure 5.8d. Comparing the results of this sample with S_2 of the same Pt-loading but different CL features, it becomes evident that S_3 exhibits superior, EOL performance, with a potential loss of only 0.07 V at a current density of 300 mA/cm^2. Although the dependence of carbon corrosion is observed by comparing the samples with various Pt-loadings, S_3 demonstrated better stability than S_6 with lower Pt-loading. One possible explanation is the inverse relationship between carbon corrosion and the CL thickness, which aligns well with increased CL thickness and high cell stability observed in S_3. To elucidate the effect of CL thickness, furthermore, the performance degradation

of S_4 during carbon corrosion AST is depicted in Figure 5.8e. Although the addition of bare carbon particles enhances the catalytic activity and exhibits superior performance during Pt-dissolution voltage cycling, significant performance fade is observed during startup-shutdown cycling. The potential loss of 0.219 V is observed in S_4, representing a 141%, and 314% increase compared to S_2 and S_3, respectively, balancing out the impact of Pt-loading. Since carbon corrosion leads to alterations in CL morphology, including electrode thinning and loss of porosity, the presence of more carbon particles in the corroded sample could contribute to increased mass transport resistances. Furthermore, the performance reduction continues to increase towards the end of the polarization curve, meaning higher current densities, due to the increased ohmic resistances.

It has been concluded that the corrosion mechanism is independent of the CL thickness. This conclusion is supported by the contrasting results obtained for S_4 and S_3, both of which have higher CL thicknesses but a consistent Pt-loading of 0.1 mg/cm^2, indicating opposing outcomes in terms of EOL performance. This finding is consistent with the results reported by Darab et al. [75], who detailed no significant correlation between carbon corrosion and CL thickness while evaluating various Pt/C ratios. Moreover, the catalytic activity of the samples plays a significant role in determining the rate of carbon corrosion. Specifically, S_4, which exhibits the best BOL performance, demonstrates higher corrosion rates, while S_3, with reduced BOL performance, displays better stability against carbon corrosion. This observation aligns with the effect of Pt-loading, as higher Pt-loaded samples exhibit a lower degree of stability against corrosion.

5.4 Summary and Conclusion

The impact of catalyst characteristics on electrode degradation is investigated through in-situ characterization. A total of 6 MEAs with varying Pt-loading, Pt/C ratio, CL thickness, and carbon support material are prepared. A comprehensive in-situ characterization is performed including impedance spectroscopy, polarization curves, and cyclic voltammetry employing two different ASTs that simulate the Pt-dissolution and carbon corrosion mechanisms. The important conclusions of this work are as follows.

- During the Pt-dissolution AST, a relative ECSA loss is observed across all the MEAs ranging from 11% to 53%, with a trend of higher ECSA loss for low Pt-loaded samples.

- The diluted sample with the same Pt-loading and additional bare carbon particles represents suppressed degradation compared to a sample of the same loading of 0.1 mg/cm^2. Both the enhanced CL thickness and the bonding effect between bare carbon particles and Pt nanoparticles may explain this observation. The relative Pt-loading loss of the CL, which composes a small fraction of the CL near the interface of Membrane-CL, is smaller for this sample compared to the original one.

- The sample with lower Pt/C ratio (20 wt.%) and Pt-loading of 0.1 mg/cm^2 represents the worst stability against the Pt-dissolution mechanism. This observation declines the positive effect of CL thickness on cell durability since this sample includes higher CL thickness than the original sample with 0.1 mg/cm^2. Moreover, commercial catalysts are prepared with smaller Pt nanoparticles for decreased Pt/C ratios, which increases the ECSA loss through the Ostwald ripening mechanism.

- The hybrid support sample exhibits a decreased dissolution rate compared to the original sample of the same loading, which may be attributed to the anchoring effect within the Pt nanoparticles and the support material.

- Higher Pt-loadings lead to increased corrosion rate across all MEAs. Since Pt is the catalyst of carbon corrosion reaction, higher Pt-loadings increase the rate of this reaction. In addition, liquid water enhances the carbon corrosion mechanism, and higher water content is generated for higher Pt-loaded samples due to the increased current generated in these samples.

- The addition of bare carbon particles accelerated the corrosion rate, due to the higher amount of carbon particles although it causes higher durability against the Pt-dissolution mechanism.

- The MEA with lower Pt/C ratios represents enhanced durability against corrosion due to its higher thickness compared to the original sample with 0.1 mg/cm^2 loading.

- The carbon corrosion mechanism is independent of the CL thickness, however, it is severely dependent on the catalytic activity, with a trend of increased catalytic activity representing deteriorated durability. This is consistent with the observed results for different Pt-loadings since higher Pt content increases the catalyst activation.

- The smaller Pt nanoparticles accelerate the Pt-dissolution mechanism. Moreover, the higher CL thickness contributes to higher durability against the Pt-dissolution mechanism, with the diluted sample with forced increased CL thickness representing the highest durability against Pt-dissolution.

- The numerical validation performed for all the samples demonstrates that the loss of ECSA and Pt-loading could not explain the performance loss in the Pt-dissolution mechanism. The rest of the performance loss could be attributed to modification in transport resistances and CL morphology.

Chapter 6

CONCLUSION

The focus of the current research thesis is to evaluate the impact of catalyst morphology including Pt-loading, Pt/C ratio, ionomer loading, dilution ratio, and carbon support material on the performance and durability of low Pt-loaded PEM fuel cells. The decrease in the cell performance due to the increased oxygen transport resistances for low Pt-loaded samples is widely reported in the literature [5][4], while the origins of such deviations are not understood thoroughly. To this end, a pseudo-three-dimensional (P3D) model is utilized with detailed mathematical sub-models for electrochemical reaction kinetics and two-phase flow. This full-cell model provides sufficient information about the distribution of the reactants, flow field considerations, operating conditions, as well as the microstructure of the layers. The model is utilized for investigation regarding the impact of CL characteristics and operating conditions on the steady-state and transient response of low Pt-loaded samples. Based on the modeling results obtained, systematic experiments consisting of 6 different samples of specific characteristics are developed. To create high-performance low Pt-loaded samples, moreover, catalyst-coated membranes (CCMs) are fabricated using the ultrasonic deposition method. The CCM approach suppresses contact resistances and provides better attachment between the CL and membrane, enhancing the transport of ions, and the ultrasonic nozzle provides uniform Pt distribution and CL thickness. The impact of different CL characteristics on the performance of low Pt-loaded samples is evaluated through comprehensive in-situ electrochemical characterizations. Moreover, the durability of all 6 samples with different CL compositions is evaluated against two different accelerated stress tests (ASTs) simulating the Pt-dissolution and carbon corrosion mechanisms.

6.1 Thesis Summary

6.1.1 PEM Fuel Cell Modeling

In chapter 2, the P3D model developed for a cell portion with straight channels at the anode and cathode electrodes is improved to include microstructural characteristics of different porous layers. To capture the sluggish kinetics of the oxygen reduction reaction, a detailed electrochemical kinetics model is incorporated into the P3D model. This model accounts for the microstructural characteristics of CCL, considering the diffusional and interfacial resistances for oxygen transport from CL pores to the surface of active Pt nanoparticles available for the electrochemical reaction [38].

The P3D model is further enhanced by incorporating the mixed wettability pore size distribution model to relate the morphological features of different porous layers including GDL, MPL, and CL to the two-phase flow model. The transport properties of porous layers including the gas and liquid permeability, saturation, liquid-gas interfacial contact area, and Knudsen radii are evaluated based on their pore size distribution characteristics and PTFE content, and included in the P3D model. The conservation equations including mass, momentum, energy, charge, species distribution, liquid water, and dissolved water are solved simultaneously. The P3D model is validated by comparing the model results with systematic experimental data available in the literature under various operating conditions for MEAs of different CL characteristics [5].

The detailed P3D model is improved to a transient one in chapter 3, considering the time-dependent governing equations including mass, momentum, species distribution, energy, liquid water, and dissolved membrane water content. The transient P3D model is validated with the available experimental data [121] concerning different current density steps using the Galvano-dynamic approach.

6.1.2 PEM Fuel Cell Durability

The development of low Pt-loaded samples of different CL characteristics is presented in chapter 4. The impact of all these characteristics including the CL thickness,

Pt-loading, and Pt/C ratio is first studied using the P3D model in chapter 2 based on experiments of Owejan et al. [5]. Based on the modeling results, 6 different samples are designed and fabricated, which despite previous experiments develop the basis for studying the impact of CL features individually. Since the ink substrate is proven to significantly affect the interfacial resistances, the catalyst-coated-membrane (CCM) approach is utilized alongside the ultrasonic deposition method. The parameters associated with the ultrasonic coating device including the distance, the temperature of the substrate, flow rate, and ink composition are optimized. The beginning-of-life (BOL) performance of the samples is evaluated under different operating conditions to capture the suitable operating conditions for the MEAs. Moreover, two samples of the same CL characteristics are developed to compare the performance of these samples and evaluate the repeatability of the coating and fabrication methods. Furthermore, scanning electron microscopy (SEM) is utilized to evaluate the CL thickness for all samples.

Two different accelerated stress tests are used to evaluate the durability of the samples. The first one concerns the Pt-dissolution mechanism, for which voltage cycling is performed within 1 and 0.6 V at a scan rate of 40 mV/s for a duration of 10000 cycles in the H_2/air environment which resembles the working environment of PEM fuel cells. The performance of samples in terms of polarization curves, ECSA loss, charge transfer and ohmic resistances is evaluated. Developing pristine samples of the same characteristics, another AST is used with voltage cycling between 1 and 1.5 V with a scan rate of 500 mV/s in the H_2/N_2 environment to provide the condition of start-up and shut down processes, evaluating the performance loss of the samples.

6.2 Outlook

The model results indicate that decreasing Pt content in the fuel cell negatively affects cell performance due to increased cathodic overpotential, primarily caused by oxygen transport resistances. However, there is a threshold for increasing the Pt-loading and enhancing the cell performance, above which the trade-off between the thickness and loading results in negligible positive impact of Pt-loading. Moreover, higher Pt-loadings

benefit the dynamics of cell behavior by decreasing the voltage undershoots from transient model results. The experimental results are in close accordance with the modeling results, showing the positive impact of Pt-loading between the three different Pt-loadings of 0.2, 0.1, and 0.05 mg/cm^2. While the performance deviation is more intense in the ohmic and activation polarization between 0.05 and 0.1 mg/cm^2, the performance deteriorates for the sample with 0.2 mg/cm^2 in the limiting current density region. The performance decrease is associated with the increased CL thickness and pore blockage for the high Pt-loaded sample, which increases the mass transport resistances in limiting the current density region. Moreover, a higher electrochemically active area is determined for low Pt-loaded samples, demonstrating the higher Pt utilization, resulting from lower agglomeration levels. Therefore, careful considerations are necessary for understanding the trade-off within the Pt-loading, CL thickness, and cost. The impact of Pt-loading on the durability of the samples is evaluated, and higher ECSA relative loss and performance decrement are observed for low Pt-loaded samples under the Pt-dissolution AST. Since the layer-by-layer deposition method is utilized for fabricating the CCMs, the Pt distribution is more uniform for low Pt-loaded samples due to the smaller number of deposited layers. The combination of lower agglomeration level and enhanced Ostwald ripening for smaller particles may explain the enhanced Pt-dissolution mechanism observed in low Pt-loaded samples. On the other hand, the low Pt-loaded sample is more durable against the carbon corrosion AST, since the Pt particles catalyze carbon oxidation reaction.

The impact of additional bare carbon particles is studied both in combination with Pt/C ratios and I/C ratios, ensuring a constant CL thickness using the P3D model. Under both conditions, the impact of bare carbon particles is more intense in the concentration region of the polarization curve. The inclusion of bare carbon particles increases the CL tortuosity and ionic resistance. Thus, there is a trade-off between increasing the I/C ratio which elevates the proton conductivity, and the addition of bare carbon particles which increases ionic resistance. In addition, the impact of the dilution ratio on the oxygen transport resistances is more intense for values of y_{Bare} greater than 0.6. Moreover, the addition of bare carbon particles increases the voltage undershoot due to the increased oxygen transport resistance, while the dynamics of cell behavior barely deviate upon the addition of bare carbon particles varying the CL thickness for a constant CL porosity. The obtained experimental results concerning the addition of bare carbon particles in this

thesis, however, represent a completely different conclusion. The diluted sample exhibits superior performance throughout the entire polarization curve except for the activation region. Moreover, the inclusion of bare carbon particles increases the active sites and ECSA. The increased cell performance in the ohmic region of the polarization curve may result from the higher electronic conductivity of the sample with bare carbon particles. In addition, the experimental results show that the diluted sample performs similarly to the sample of higher Pt-loading (0.2 mg/cm^2), which shows higher Pt utilization and bond between ionomer, Pt particles, and carbon particles in the diluted sample. However, the enhanced performance of the diluted sample is dependent on the deposition method as well. It should be noted that Owejan et al. [5] reported the decreased performance of the diluted samples, however, they employed samples of the same CL thickness using higher Pt/C ratios for diluted samples. The experimental evaluation of the diluted sample in this work suggests that the addition of bare carbon particles enhances the durability of the sample against the Pt-dissolution mechanism. This could be attributed either to the increased CL thickness or the enhanced bonding effect between the Pt particles and the carbon substrate upon the addition of more bare carbon particles. The durability of this sample against carbon corrosion AST confirms the higher Pt utilization, which is in agreement with elevated ECSA values observed for the diluted sample, and results in an increased corrosion rate.

The modeling results concerning the impact of the Pt/C ratio are combined with the I/C ratio and bare carbon particles. These results show the minimal impact of the Pt/C ratio on the activation region of the polarization curve. In addition, there is no direct impact of the Pt/C ratio on the ionic and oxygen transport resistances. However, the Pt/C ratio affects the total amount of carbon particles in the CL and modifies the CL pore structure, while its effects are not studied individually in the modeling part of this work. In the experimental part of this thesis, I developed and tested an MEA with a 20% Pt/C ratio to capture the sole impact of this parameter. Lower Pt/C ratios cause an increase in the BOL ECSA value while adversely affecting cell performance. Smaller Pt nanoparticle sizes are previously reported for lower Pt/C ratio samples in literature [75][64]. While the size of Pt particles is not evaluated in this work, the increased ECSA values could reveal the smaller Pt particles used in commercial samples of lower Pt/C ratios. In addition, to achieve 0.1 mg/cm^2 Pt-loading in this sample, more deposition layers are required due

to the lower Pt content of the sample. This causes increased CL thickness, reducing the performance in the ohmic region of the polarization curve. The modeling results also suggest that the CL porosity decreases by 30% from the sample prepared with a 40% Pt/C ratio to the one prepared with a 20% Pt/C ratio. The decreased CL porosity increases the mass transport resistances and reduces cell performance in the concentration region of the polarization curve. Comparing the durability of 40 and 20% Pt/C ratio MEAs prepared in this thesis suggests that the reduction of Pt weight percentage results in lower durability against the Pt-dissolution, while it enhances the carbon corrosion durability. It is concluded that the cell durability against carbon corrosion is independent of the CL thickness while it is more dependent on the catalyst activity, and the durability against Pt-dissolution is mostly affected by the Pt nanoparticles radii.

The effect of carbon support material is investigated in the experimental part of this research. Lower catalytic activity and ECSA values are determined for the hybrid sample with the reduced graphene oxide and carbon black support material reported by Kaplan et al. [114]. This sample includes a 30% Pt/C ratio, and a lower Pt/C ratio compared to the base sample of 40% Pt/C ratio contributes to its poor performance, primarily due to the enhanced ohmic resistances as evidenced by EIS results. Evaluating the durability of this sample against the Pt-dissolution mechanism, a lower dissolution rate is observed for this sample showing the positive impact of the 2D structure of the graphene on suppressing the Ostwald ripening.

In the modeling part of this thesis, the influence of the I/C ratio on cell performance, oxygen transport resistances, and ionic potential losses is studied in combination with the Pt/C ratio and bare carbon mass fractions. Small I/C ratios cause increased CL ionic resistances, reducing the performance in the ohmic polarization region. On the other hand, higher ionomer loading in the CL enhances the proton conductivity of the CCL while decreasing the CL porosity. Furthermore, higher cell power density is achieved when operating the cell with 60% relative humidity for high I/C ratios. This highlights the need for further investigation into ionomer conductivity, especially alongside relative humidity and water content. Since the impact of ionomer content is not explored experimentally in this work, additional analysis is necessary to conclude about its effects on performance and cell durability.

The model results suggest that operating at higher temperatures can improve fuel cell

performance due to increased catalytic activity. However, there is a trade-off between temperature and proton conductivity, as very high temperatures can negatively impact conductivity. Experiments confirm this by showing that increasing temperature enhances cell performance under constant relative humidity conditions, but excessive temperature elevation leads to higher ohmic resistances. Moreover, I found that higher relative humidity ratios decrease protonic conductivity while causing higher voltage undershoots. Experimental results support the positive impact of relative humidity ratios. However, the modeling results indicate that using ratios greater than 80% requires caution to avoid cathode layer flooding. Additionally, both modeling and experimental findings show that higher operating pressures result in improved cell performance. In addition to the steady-state mode results, the transient model suggests a significant reduction in voltage undershoot when using higher stoichiometric ratios. Lastly, it is concluded that low Pt-loaded samples are more sensitive to the change in operating conditions.

6.3 Future Work

While this research thesis has made progress in addressing Pt reduction, enhancing cell durability, and reducing costs in PEM fuel cells, some challenges remain for their commercialization. Future work can build upon the results obtained in this study to shed more light on these issues and provide a better understanding of CCL structure.

- In this thesis research, all the CCL characteristics are individually examined for low Pt-loaded samples, except for the I/C ratio. Given the strong correlation between the I/C ratio and relative humidity, it is essential to investigate the impact of the I/C ratio on fuel cell durability using various ASTs conducted under varying relative humidity conditions. Additionally, this research reveals that low Pt-loaded samples have reduced water adsorption capability, making an investigation into the I/C ratio crucial for such samples.

- Enhancing the detailed electrochemical model to include the impact of water film on the oxygen transport resistances as well as pore structure. Although the current model includes the effect of both, the results demonstrate a slight dependence of

the model on pore volume.

- Since the degradation observations propose the morphological changes in the CL, the proper investigation of CL structural properties through physical characterizations and imaging techniques is necessary to provide enhanced degradation models.
- The introduction of a degradation model into the P3D model highlights the need for further exploration of the influence of CL flooding, especially in the case of low Pt-loaded samples with smaller CL thickness, on cell degradation.

REFERENCES

[1] Y. Wang, K. S. Chen, J. Mishler, S. C. Cho, and X. C. Adroher, "A review of polymer electrolyte membrane fuel cells: Technology, applications, and needs on fundamental research," *Applied Energy*, vol. 88, no. 4, pp. 981–1007, 2011.

[2] Y. Wang, H. Yuan, A. Martinez, P. Hong, H. Xu, and F. R. Bockmiller, "Polymer electrolyte membrane fuel cell and hydrogen station networks for automobiles: Status, technology, and perspectives," *Advances in Applied Energy*, vol. 2, p. 100 011, 2021.

[3] O. Gröger, H. A. Gasteiger, and J.-P. Suchsland, "Review—electromobility: Batteries or fuel cells?" *Journal of The Electrochemical Society*, vol. 162, no. 14, A2605–A2622, 2015.

[4] T. A. Greszler, D. Caulk, and P. Sinha, "The impact of platinum loading on oxygen transport resistance," *Journal of The Electrochemical Society*, vol. 159, no. 12, F831–F840, 2012.

[5] J. P. Owejan, J. E. Owejan, and W. Gu, "Impact of platinum loading and catalyst layer structure on PEMFC performance," *Journal of The Electrochemical Society*, vol. 160, no. 8, F824–F833, 2013.

[6] A. Z. Weber, R. L. Borup, R. M. Darling, *et al.*, "A critical review of modeling transport phenomena in polymer-electrolyte fuel cells," *Journal of The Electrochemical Society*, vol. 161, no. 12, F1254–F1299, 2014.

[7] A. Kusoglu and A. Z. Weber, "New insights into perfluorinated sulfonic-acid ionomers," *Chemical Reviews*, vol. 117, no. 3, pp. 987–1104, 2017.

[8] K. A. Page, A. Kusoglu, C. M. Stafford, S. Kim, R. J. Kline, and A. Z. Weber, "Confinement-driven increase in ionomer thin-film modulus," *Nano Letters*, vol. 14, no. 5, pp. 2299–2304, 2014.

[9] B. Kim, D. Cha, and Y. Kim, "The effects of air stoichiometry and air excess ratio on the transient response of a PEMFC under load change conditions," *Applied Energy*, vol. 138, pp. 143–149, 2015.

[10] A. Goshtasbi, P. García-Salaberri, J. Chen, K. Talukdar, D. G. Sanchez, and T. Ersal, "Through-the-membrane transient phenomena in PEM fuel cells: A modeling study," *Journal of The Electrochemical Society*, vol. 166, no. 7, F3154–F3179, 2019.

[11] Q. Meyer, Y. Zeng, and C. Zhao, "Electrochemical impedance spectroscopy of catalyst and carbon degradations in proton exchange membrane fuel cells," *Journal of Power Sources*, vol. 437, p. 226 922, 2019.

[12] A. Z. Weber, "Gas-crossover and membrane-pinhole effects in polymer-electrolyte fuel cells," *Journal of The Electrochemical Society*, vol. 155, no. 6, B521, 2008.

[13] M. Inaba, "Chemical degradation of perfluorinated sulfonic acid membranes," in *Polymer Electrolyte Fuel Cell Durability*, Springer New York, pp. 57–69.

[14] C. Lim, L. Ghassemzadeh, F. V. Hove, *et al.*, "Membrane degradation during combined chemical and mechanical accelerated stress testing of polymer electrolyte fuel cells," *Journal of Power Sources*, vol. 257, pp. 102–110, 2014.

[15] A. Kusoglu and A. Z. Weber, "A mechanistic model for pinhole growth in fuel-cell membranes during cyclic loads," *Journal of The Electrochemical Society*, vol. 161, no. 8, E3311–E3322, 2014.

[16] M. N. Silberstein and M. C. Boyce, "Constitutive modeling of the rate, temperature, and hydration dependent deformation response of nafion to monotonic and cyclic loading," *Journal of Power Sources*, vol. 195, no. 17, pp. 5692–5706, 2010.

[17] J. Zhou, S. Shukla, A. Putz, and M. Secanell, "Analysis of the role of the microporous layer in improving polymer electrolyte fuel cell performance," *Electrochimica Acta*, vol. 268, pp. 366–382, 2018.

[18] A. El-kharouf and B. G. Pollet, "Gas diffusion media and their degradation," in *Polymer Electrolyte Fuel Cell Degradation*, Elsevier, 2012, pp. 215–247.

[19] X. Gao, J. Chen, R. Xu, *et al.*, "Research progress and prospect of the materials of bipolar plates for proton exchange membrane fuel cells (PEMFCs)," *International Journal of Hydrogen Energy*, 2023.

[20] J. Wang, "Theory and practice of flow field designs for fuel cell scaling-up: A critical review," *Applied Energy*, vol. 157, pp. 640–663, 2015.

[21] H.-C. Chiu, J.-H. Jang, W.-M. Yan, H.-Y. Li, and C.-C. Liao, "A three-dimensional modeling of transport phenomena of proton exchange membrane fuel cells with various flow fields," *Applied Energy*, vol. 96, pp. 359–370, 2012.

[22] D. Singdeo, T. Dey, S. Gaikwad, S. J. Andreasen, and P. C. Ghosh, "A new modified-serpentine flow field for application in high temperature polymer electrolyte fuel cell," *Applied Energy*, vol. 195, pp. 13–22, 2017.

[23] O. B. Rizvandi, M. G. Eskin, and S. Yesilyurt, "Numerical modeling of anode-bleeding PEM fuel cells: Effects of operating conditions and flow field design," *International Journal of Hydrogen Energy*, vol. 46, no. 5, pp. 4378–4398, 2021.

[24] P.-C. Sui, X. Zhu, and N. Djilali, "Modeling of PEM fuel cell catalyst layers: Status and outlook," *Electrochemical Energy Reviews*, vol. 2, no. 3, pp. 428–466, 2019.

[25] P. Schneider, M. Batool, A. O. Godoy, *et al.*, "Impact of platinum loading and layer thickness on cathode catalyst degradation in PEM fuel cells," *Journal of The Electrochemical Society*, vol. 170, no. 2, p. 024 506, 2023.

[26] T. V. Cleve, S. Khandavalli, A. Chowdhury, *et al.*, "Dictating pt-based electrocatalyst performance in polymer electrolyte fuel cells, from formulation to application," *ACS Applied Materials &amp Interfaces*, vol. 11, no. 50, pp. 46 953–46 964, 2019.

[27] K.-H. Kim, K.-Y. Lee, H.-J. Kim, *et al.*, "The effects of nafion® ionomer content in PEMFC MEAs prepared by a catalyst-coated membrane (CCM) spraying method," *International Journal of Hydrogen Energy*, vol. 35, no. 5, pp. 2119–2126, 2010.

[28] N. Macauley, D. D. Papadias, J. Fairweather, *et al.*, "Carbon corrosion in PEM fuel cells and the development of accelerated stress tests," *Journal of The Electrochemical Society*, vol. 165, no. 6, F3148–F3160, 2018.

[29] T. E. Springer, T. A. Zawodzinski, and S. Gottesfeld, "Polymer electrolyte fuel cell model," *Journal of The Electrochemical Society*, vol. 138, no. 8, pp. 2334–2342, 1991.

[30] P. Choi and R. Datta, "Sorption in proton-exchange membranes," *Journal of The Electrochemical Society*, vol. 150, no. 12, E601, 2003.

[31] C. W. Monroe, T. Romero, W. Mérida, and M. Eikerling, "A vaporization-exchange model for water sorption and flux in nafion," *Journal of Membrane Science*, vol. 324, no. 1-2, pp. 1–6, 2008.

[32] R. Anderson, L. Zhang, Y. Ding, M. Blanco, X. Bi, and D. P. Wilkinson, "A critical review of two-phase flow in gas flow channels of proton exchange membrane fuel cells," *Journal of Power Sources*, vol. 195, no. 15, pp. 4531–4553, 2010.

[33] S. G. Kandlikar, E. J. See, and R. Banerjee, "Modeling two-phase pressure drop along PEM fuel cell reactant channels," *Journal of The Electrochemical Society*, vol. 162, no. 7, F772–F782, 2015.

[34] A. Z. Weber, R. M. Darling, and J. Newman, "Modeling two-phase behavior in PEFCs," *Journal of The Electrochemical Society*, vol. 151, no. 10, A1715, 2004.

[35] A. Z. Weber, "Improved modeling and understanding of diffusion-media wettability on polymer-electrolyte-fuel-cell performance," *Journal of Power Sources*, vol. 195, no. 16, pp. 5292–5304, 2010.

[36] J. Liu and M. Eikerling, "Model of cathode catalyst layers for polymer electrolyte fuel cells: The role of porous structure and water accumulation," *Electrochimica Acta*, vol. 53, no. 13, pp. 4435–4446, 2008.

[37] T. Mashio, H. Iden, A. Ohma, and T. Tokumasu, "Modeling of local gas transport in catalyst layers of PEM fuel cells," *Journal of Electroanalytical Chemistry*, vol. 790, pp. 27–39, 2017.

[38] L. Hao, K. Moriyama, W. Gu, and C.-Y. Wang, "Modeling and experimental validation of pt loading and electrode composition effects in PEM fuel cells," *Journal of The Electrochemical Society*, vol. 162, no. 8, F854–F867, 2015.

[39] H. Gasteiger, J. Panels, and S. Yan, "Dependence of PEM fuel cell performance on catalyst loading," *Journal of Power Sources*, vol. 127, no. 1-2, pp. 162–171, 2004.

[40] J. X. Wang, T. E. Springer, and R. R. Adzic, "Dual-pathway kinetic equation for the hydrogen oxidation reaction on pt electrodes," *Journal of The Electrochemical Society*, vol. 153, no. 9, A1732, 2006.

[41] J. X. Wang, J. Zhang, and R. R. Adzic, "Double-trap kinetic equation for the oxygen reduction reaction on pt(111) in acidic media," *The Journal of Physical Chemistry A*, vol. 111, no. 49, pp. 12 702–12 710, 2007.

[42] S. Yesilyurt, J. B. Siegel, and A. G. Stefanopoulou, "Modeling and experiments of voltage transients of polymer electrolyte membrane fuel cells with the dead-ended anode," *Journal of Fuel Cell Science and Technology*, vol. 9, no. 2, 2012.

[43] U. Pasaogullari and C. Y. Wang, "Liquid water transport in gas diffusion layer of polymer electrolyte fuel cells," *Journal of The Electrochemical Society*, vol. 151, no. 3, A399, 2004.

[44] T. F. Fuller and J. Newman, "Water and thermal management in solid-polymer-electrolyte fuel cells," *Journal of The Electrochemical Society*, vol. 140, no. 5, pp. 1218–1225, 1993.

[45] L. Rostami, P. M. G. Nejad, and A. Vatani, "A numerical investigation of serpentine flow channel with different bend sizes in polymer electrolyte membrane fuel cells," *Energy*, vol. 97, pp. 400–410, 2016.

[46] Q. Ye and T. V. Nguyen, "Three-dimensional simulation of liquid water distribution in a PEMFC with experimentally measured capillary functions," *Journal of The Electrochemical Society*, vol. 154, no. 12, B1242, 2007.

[47] T. Berning and N. Djilali, "A 3d, multiphase, multicomponent model of the cathode and anode of a PEM fuel cell," *Journal of The Electrochemical Society*, vol. 150, no. 12, A1589, 2003.

[48] A. Iranzo, M. Muñoz, F. Rosa, and J. Pino, "Numerical model for the performance prediction of a PEM fuel cell. model results and experimental validation," *International Journal of Hydrogen Energy*, vol. 35, no. 20, pp. 11 533–11 550, 2010.

[49] F. Nandjou, J.-P. Poirot-Crouvezier, M. Chandesris, and Y. Bultel, "A pseudo-3d model to investigate heat and water transport in large area PEM fuel cells – part 1: Model development and validation," *International Journal of Hydrogen Energy*, vol. 41, no. 34, pp. 15 545–15 561, 2016.

[50] O. B. Rizvandi and S. Yesilyurt, "A pseudo three-dimensional, two-phase, non-isothermal model of proton exchange membrane fuel cell," *Electrochimica Acta*, vol. 302, pp. 180–197, 2019.

[51] P. He, Y.-T. Mu, J. W. Park, and W.-Q. Tao, "Modeling of the effects of cathode catalyst layer design parameters on performance of polymer electrolyte membrane fuel cell," *Applied Energy*, vol. 277, p. 115 555, 2020.

[52] T.-F. Cao, H. Lin, L. Chen, Y.-L. He, and W.-Q. Tao, "Numerical investigation of the coupled water and thermal management in PEM fuel cell," *Applied Energy*, vol. 112, pp. 1115–1125, 2013.

[53] T. J. Silverman, J. P. Meyers, and J. J. Beaman, "Dynamic thermal, transport and mechanical model of fuel cell membrane swelling," *Fuel Cells*, vol. 11, no. 6, pp. 875–887, 2011.

[54] A. Verma and R. Pitchumani, "Influence of membrane properties on the transient behavior of polymer electrolyte fuel cells," *Journal of Power Sources*, vol. 268, pp. 733–743, 2014.

[55] W. Yang, D. Cha, and Y. Kim, "Effects of flow direction on dynamic response and stability of nonhumidification PEM fuel cell," *Energy*, vol. 185, pp. 386–395, 2019.

[56] Y. Wang and C.-Y. Wang, "Transient analysis of polymer electrolyte fuel cells," *Electrochimica Acta*, vol. 50, no. 6, pp. 1307–1315, 2005.

[57] M. Grötsch and M. Mangold, "A two-phase PEMFC model for process control purposes," *Chemical Engineering Science*, vol. 63, no. 2, pp. 434–447, 2008.

[58] K. Promislow, P. Chang, H. Haas, and B. Wetton, "Two-phase unit cell model for slow transients in polymer electrolyte membrane fuel cells," *Journal of The Electrochemical Society*, vol. 155, no. 7, A494, 2008.

[59] S. Noorani and T. Shamim, "Transient response of a polymer electrolyte membrane fuel cell subjected to modulating cell voltage," *International Journal of Energy Research*, vol. 37, no. 6, pp. 535–546, 2011.

[60] S. Ott, A. Bauer, F. Du, *et al.*, "Impact of carbon support meso-porosity on mass transport and performance of PEMFC cathode catalyst layers," *ChemCatChem*, vol. 13, no. 22, pp. 4759–4769, 2021.

[61] L. Castanheira, W. O. Silva, F. H. Lima, A. Crisci, L. Dubau, and F. Maillard, "Carbon corrosion in proton-exchange membrane fuel cells: Effect of the carbon structure, the degradation protocol, and the gas atmosphere," *ACS Catalysis*, vol. 5, no. 4, pp. 2184–2194, 2015.

[62] C. A. Reiser, L. Bregoli, T. W. Patterson, *et al.*, "A reverse-current decay mechanism for fuel cells," *Electrochemical and Solid-State Letters*, vol. 8, no. 6, A273, 2005.

[63] P. Zihrul, I. Hartung, S. Kirsch, G. Huebner, F. Hasché, and H. A. Gasteiger, "Voltage cycling induced losses in electrochemically active surface area and in hsub2/sub/air-performance of PEM fuel cells," *Journal of The Electrochemical Society*, vol. 163, no. 6, F492–F498, 2016.

[64] G. S. Harzer, J. N. Schwämmlein, A. M. Damjanović, S. Ghosh, and H. A. Gasteiger, "Cathode loading impact on voltage cycling induced PEMFC degradation: A voltage loss analysis," *Journal of The Electrochemical Society*, vol. 165, no. 6, F3118–F3131, 2018.

[65] L. Fan, J. Zhao, X. Luo, and Z. Tu, "Comparison of the performance and degradation mechanism of PEMFC with pt/c and pt black catalyst," *International Journal of Hydrogen Energy*, vol. 47, no. 8, pp. 5418–5428, 2022.

[66] M. Wang, M. Chen, Z. Yang, *et al.*, "High-performance and durable cathode catalyst layer with hydrophobic c@PTFE particles for low-pt loading membrane assembly electrode of PEMFC," *Energy Conversion and Management*, vol. 191, pp. 132–140, 2019.

[67] M. Uchimura and S. S. Kocha, "The impact of cycle profile on PEMFC durability," *ECS Transactions*, vol. 11, no. 1, pp. 1215–1226, 2007.

[68] C. A. Rice, P. Urchaga, A. O. Pistono, B. W. McFerrin, B. T. McComb, and J. Hu, "Platinum dissolution in fuel cell electrodes: Enhanced degradation from surface area assessment in automotive accelerated stress tests," *Journal of The Electrochemical Society*, vol. 162, no. 10, F1175–F1180, 2015.

[69] M. S. Wilson, F. H. Garzon, K. E. Sickafus, and S. Gottesfeld, "Surface area loss of supported platinum in polymer electrolyte fuel cells," *Journal of The Electrochemical Society*, vol. 140, no. 10, pp. 2872–2877, 1993.

[70] M. Uchimura, S. Sugawara, Y. Suzuki, J. Zhang, and S. S. Kocha, "Electrocatalyst durability under simulated automotive drive cycles," *ECS Transactions*, vol. 16, no. 2, pp. 225–234, 2008.

[71] P. Urchaga, T. Kadyk, S. G. Rinaldo, *et al.*, "Catalyst degradation in fuel cell electrodes: Accelerated stress tests and model-based analysis," *Electrochimica Acta*, vol. 176, pp. 1500–1510, 2015.

[72] S. Cherevko, G. P. Keeley, S. Geiger, *et al.*, "Dissolution of platinum in the operational range of fuel cells," *ChemElectroChem*, vol. 2, no. 10, pp. 1471–1478, 2015.

[73] A. Kneer, J. Jankovic, D. Susac, *et al.*, "Correlation of changes in electrochemical and structural parameters due to voltage cycling induced degradation in PEM fuel cells," *Journal of The Electrochemical Society*, vol. 165, no. 6, F3241–F3250, 2018.

[74] F. Hegge, J. Sharman, R. Moroni, *et al.*, "Impact of carbon support corrosion on performance losses in polymer electrolyte membrane fuel cells," *Journal of The Electrochemical Society*, vol. 166, no. 13, F956–F962, 2019.

[75] M. Darab, A. O. Barnett, G. Lindbergh, M. S. Thomassen, and S. Sunde, "The influence of catalyst layer thickness on the performance and degradation of PEM fuel cell cathodes with constant catalyst loading," *Electrochimica Acta*, vol. 232, pp. 505–516, 2017.

[76] Y. Li, Z. Zheng, X. Chen, *et al.*, "Carbon corrosion behaviors and the mechanical properties of proton exchange membrane fuel cell cathode catalyst layer," *International Journal of Hydrogen Energy*, vol. 45, no. 43, pp. 23 519–23 525, 2020.

[77] A. Saeidfar and S. Yesilyurt, "Numerical investigation of the effects of catalyst layer composition and channel to rib width ratios for low platinum loaded PEMFCs," *Applied Energy*, vol. 339, p. 121 040, 2023.

[78] S. Ge, X. Li, B. Yi, and I.-M. Hsing, "Absorption, desorption, and transport of water in polymer electrolyte membranes for fuel cells," *Journal of The Electrochemical Society*, vol. 152, no. 6, A1149, 2005.

[79] J. T. Gostick, M. A. Ioannidis, M. W. Fowler, and M. D. Pritzker, "Wettability and capillary behavior of fibrous gas diffusion media for polymer electrolyte membrane fuel cells," *Journal of Power Sources*, vol. 194, no. 1, pp. 433–444, 2009.

[80] I. V. Zenyuk, D. Y. Parkinson, L. G. Connolly, and A. Z. Weber, "Gas-diffusion-layer structural properties under compression via x-ray tomography," *Journal of Power Sources*, vol. 328, pp. 364–376, 2016.

[81] T. Mashio, K. Sato, and A. Ohma, "Analysis of water adsorption and condensation in catalyst layers for polymer electrolyte fuel cells," *Electrochimica Acta*, vol. 140, pp. 238–249, 2014.

[82] N. Zamel, E. Litovsky, S. Shakhshir, X. Li, and J. Kleiman, "Measurement of in-plane thermal conductivity of carbon paper diffusion media in the temperature range of -20°c to 120°c," *Applied Energy*, vol. 88, no. 9, pp. 3042–3050, 2011.

[83] X. Yan, Z. Xu, S. Yuan, *et al.*, "Structural and transport properties of ultrathin perfluorosulfonic acid ionomer film in proton exchange membrane fuel cell catalyst layer: A review," *Journal of Power Sources*, vol. 536, p. 231 523, 2022.

[84] Z. Wang, C. Wang, and K. Chen, "Two-phase flow and transport in the air cathode of proton exchange membrane fuel cells," *Journal of Power Sources*, vol. 94, no. 1, pp. 40–50, 2001.

[85] V. Mulone and K. Karan, "Analysis of capillary flow driven model for water transport in PEFC cathode catalyst layer: Consideration of mixed wettability and pore size distribution," *International Journal of Hydrogen Energy*, vol. 38, no. 1, pp. 558–569, 2013.

[86] M. Eikerling, "Water management in cathode catalyst layers of PEM fuel cells," *Journal of The Electrochemical Society*, vol. 153, no. 3, E58, 2006.

[87] P. A. Mateo Villanueva, "A mixed wettability pore size distribution model for the analysis of water transport in pemfc materials," 2013.

[88] G. Luo, Y. Ji, C.-Y. Wang, and P. K. Sinha, "Modeling liquid water transport in gas diffusion layers by topologically equivalent pore network," *Electrochimica Acta*, vol. 55, no. 19, pp. 5332–5341, 2010.

[89] N. Burdine, "Relative permeability calculations from pore size distribution data," *Journal of Petroleum Technology*, vol. 5, no. 03, pp. 71–78, 1953.

[90] M. J. Martinez, S. Shimpalee, J. W. V. Zee, and A. V. Sakars, "Assessing methods and data for pore-size distribution of PEMFC gas-diffusion media," *Journal of The Electrochemical Society*, vol. 156, no. 5, B558, 2009.

[91] B. Lefevre, A. Saugey, J. Barrat, *et al.*, "Intrusion and extrusion of water in highly hydrophobic mesoporous materials: Effect of the pore texture," *Colloids and Surfaces A: Physicochemical and Engineering Aspects*, vol. 241, no. 1-3, pp. 265–272, 2004.

[92] Y.-T. Mu, A. Z. Weber, Z.-L. Gu, and W.-Q. Tao, "Mesoscopic modeling of transport resistances in a polymer-electrolyte fuel-cell catalyst layer: Analysis of hydrogen limiting currents," *Applied Energy*, vol. 255, p. 113 895, 2019.

[93] T. Berning, D. Lu, and N. Djilali, "Three-dimensional computational analysis of transport phenomena in a PEM fuel cell," *Journal of Power Sources*, vol. 106, no. 1-2, pp. 284–294, 2002.

[94] N. Siegel, M. Ellis, D. Nelson, and M. von Spakovsky, "Single domain PEMFC model based on agglomerate catalyst geometry," *Journal of Power Sources*, vol. 115, no. 1, pp. 81–89, 2003.

[95] Q. Wang, M. Eikerling, D. Song, and Z. Liu, "Structure and performance of different types of agglomerates in cathode catalyst layers of PEM fuel cells," *Journal of Electroanalytical Chemistry*, vol. 573, no. 1, pp. 61–69, 2004.

[96] W. Sun, B. A. Peppley, and K. Karan, "An improved two-dimensional agglomerate cathode model to study the influence of catalyst layer structural parameters," *Electrochimica Acta*, vol. 50, no. 16-17, pp. 3359–3374, 2005.

[97] H. Iden, K. Sato, A. Ohma, and K. Shinohara, "Relationship among microstructure, ionomer property and proton transport in pseudo catalyst layers," *Journal of The Electrochemical Society*, vol. 158, no. 8, B987, 2011.

[98] A. Kulikovsky, "How important is oxygen transport in agglomerates in a PEM fuel cell catalyst layer," vol. 130, pp. 826–829, 2014.

[99] T. Muzaffar, T. Kadyk, and M. Eikerling, "Tipping water balance and the pt loading effect in polymer electrolyte fuel cells: A model-based analysis," *Sustainable Energy &amp Fuels*, vol. 2, no. 6, pp. 1189–1196, 2018.

[100] H. Liu, W. K. Epting, and S. Litster, "Gas transport resistance in polymer electrolyte thin films on oxygen reduction reaction catalysts," *Langmuir*, vol. 31, no. 36, pp. 9853–9858, 2015.

[101] R. Jinnouchi, K. Kudo, N. Kitano, and Y. Morimoto, "Molecular dynamics simulations on o 2 permeation through nafion ionomer on platinum surface," *Electrochimica Acta*, vol. 188, pp. 767–776, 2016.

[102] N. Nonoyama, S. Okazaki, A. Z. Weber, Y. Ikogi, and T. Yoshida, "Analysis of oxygen-transport diffusion resistance in proton-exchange-membrane fuel cells," *Journal of The Electrochemical Society*, vol. 158, no. 4, B416, 2011.

[103] A. Ohma, T. Mashio, K. Sato, *et al.*, "Analysis of proton exchange membrane fuel cell catalyst layers for reduction of platinum loading at nissan," *Electrochimica Acta*, vol. 56, no. 28, pp. 10 832–10 841, 2011.

[104] T. Suzuki, K. Kudo, and Y. Morimoto, "Model for investigation of oxygen transport limitation in a polymer electrolyte fuel cell," *Journal of Power Sources*, vol. 222, pp. 379–389, 2013.

[105] Y. Liu, M. W. Murphy, D. R. Baker, *et al.*, "Proton conduction and oxygen reduction kinetics in PEM fuel cell cathodes: Effects of ionomer-to-carbon ratio and relative humidity," *Journal of The Electrochemical Society*, vol. 156, no. 8, B970, 2009.

[106] K. Karan, "PEFC catalyst layer: Recent advances in materials, microstructural characterization, and modeling," *Current Opinion in Electrochemistry*, vol. 5, no. 1, pp. 27–35, 2017.

[107] N. P. Subramanian, T. A. Greszler, J. Zhang, W. Gu, and R. Makharia, "Pt-oxide coverage-dependent oxygen reduction reaction (ORR) kinetics," *Journal of The Electrochemical Society*, vol. 159, no. 5, B531–B540, 2012.

[108] A. Goshtasbi, J. Chen, J. R. Waldecker, S. Hirano, and T. Ersal, "Effective parameterization of PEM fuel cell models—part i: Sensitivity analysis and parameter identifiability," *Journal of The Electrochemical Society*, vol. 167, no. 4, p. 044 504, 2020.

[109] C. Mittelsteadt and H. Liu, *Conductivity, permeability, and ohmic shorting of ionomeric membranes*. 2010.

[110] N. Wang, Z. Qu, Z. Jiang, and G. Zhang, "A unified catalyst layer design classification criterion on proton exchange membrane fuel cell performance based on a modified agglomerate model," *Chemical Engineering Journal*, vol. 447, p. 137 489, 2022.

[111] X. Sun, H. Yu, L. Zhou, *et al.*, "Influence of platinum dispersity on oxygen transport resistance and performance in PEMFC," *Electrochimica Acta*, vol. 332, p. 135 474, 2020.

[112] S. Shahgaldi, I. Alaefour, and X. Li, "Impact of manufacturing processes on proton exchange membrane fuel cell performance," *Applied Energy*, vol. 225, pp. 1022–1032, 2018.

[113] L. Xing, P. K. Das, X. Song, M. Mamlouk, and K. Scott, "Numerical analysis of the optimum membrane/ionomer water content of PEMFCs: The interaction of nafion® ionomer content and cathode relative humidity," *Applied Energy*, vol. 138, pp. 242–257, 2015.

[114] B. Y. Kaplan, N. Haghmoradi, E. Biçer, C. Merino, and S. A. Gürsel, "High performance electrocatalysts supported on graphene based hybrids for polymer electrolyte membrane fuel cells," *international journal of hydrogen energy*, vol. 43, no. 52, pp. 23 221–23 230, 2018.

[115] E. Carcadea, M. Varlam, D. B. Ingham, *et al.*, "The effects of cathode flow channel size and operating conditions on PEM fuel performance: A CFD modelling study and experimental demonstration," *International Journal of Energy Research*, vol. 42, no. 8, pp. 2789–2804, 2018.

[116] Z. Huang, J. Shen, S. H. Chan, and Z. Tu, "Transient response of performance in a proton exchange membrane fuel cell under dynamic loading," *Energy Conversion and Management*, vol. 226, p. 113 492, 2020.

[117] Q. Yan, H. Toghiani, and H. Causey, "Steady state and dynamic performance of proton exchange membrane fuel cells (PEMFCs) under various operating conditions and load changes," *Journal of Power Sources*, vol. 161, no. 1, pp. 492–502, 2006.

[118] J. Cho, H.-S. Kim, and K. Min, "Transient response of a unit proton-exchange membrane fuel cell under various operating conditions," *Journal of Power Sources*, vol. 185, no. 1, pp. 118–128, 2008.

[119] S. H. Kim, "Prediction of transient response for a 25-cm2 PEM fuel cell," *ECS Proceedings Volumes*, vol. 2002-31, no. 1, pp. 349–360, 2002.

[120] A. Saeidfar and S. Yeşilyurt, "Effect of cathode composition and pt loading on the performance of pemfcs," 2022.

[121] F. Pei and F. Chen, "Transient response research on proton exchange membrane fuel cells based on a fully validated dynamic multi-phase model," *International Journal of Energy Research*, vol. 46, no. 2, pp. 1108–1125, 2021.

[122] H. Ren, X. Meng, Y. Lin, and Z. Shao, "Microstructure formation mechanism of catalyst layer and its effect on fuel cell performance: Effect of dispersion medium composition," *Journal of Energy Chemistry*, vol. 73, pp. 588–598, 2022.

[123] R. Subbaraman, D. Strmcnik, A. P. Paulikas, V. R. Stamenkovic, and N. M. Markovic, "Oxygen reduction reaction at three-phase interfaces," *ChemPhysChem*, vol. 11, no. 13, pp. 2825–2833, 2010.

[124] S. Uemura, Y. Kameya, N. Iriguchi, T. Yoshida, K. Shinohara, and S. Hirai, "Communication—investigation of catalyst ink degradation by x-ray CT," *Journal of The Electrochemical Society*, vol. 165, no. 3, F142–F144, 2018.

[125] M. Chisaka and H. Daiguji, "Effect of organic solvents on catalyst layer structure in polymer electrolyte membrane fuel cells," *Journal of The Electrochemical Society*, vol. 156, no. 1, B22, 2009.

[126] Y. Xing, L. Liu, Z. Li, Y. Li, Z. Fu, and H. Li, "Effect of membrane deposition methods on the performance of membrane electrode assemblies," *Fuel Cells*, vol. 23, no. 2, pp. 161–169, 2023.

[127] M. B. Sassin, Y. Garsany, B. D. Gould, and K. E. Swider-Lyons, "Fabrication method for laboratory-scale high-performance membrane electrode assemblies for fuel cells," *Analytical Chemistry*, vol. 89, no. 1, pp. 511–518, 2016.

[128] X. Liang, G. Pan, L. Xu, and J. Wang, "A modified decal method for preparing the membrane electrode assembly of proton exchange membrane fuel cells," *Fuel*, vol. 139, pp. 393–400, 2015.

[129] H.-S. Park, Y.-H. Cho, Y.-H. Cho, *et al.*, "Modified decal method and its related study of microporous layer in PEM fuel cells," *Journal of The Electrochemical Society*, vol. 155, no. 5, B455, 2008.

[130] W. Wang, S. Chen, J. Li, and W. Wang, "Fabrication of catalyst coated membrane with screen printing method in a proton exchange membrane fuel cell," *International Journal of Hydrogen Energy*, vol. 40, no. 13, pp. 4649–4658, 2015.

[131] S. Shukla, D. Stanier, M. S. Saha, J. Stumper, and M. Secanell, "Analysis of inkjet printed PEFC electrodes with varying platinum loading," *Journal of The Electrochemical Society*, vol. 163, no. 7, F677–F687, 2016.

[132] R. Benítez, J. Soler, and L. Daza, "Novel method for preparation of PEMFC electrodes by the electrospray technique," *Journal of Power Sources*, vol. 151, pp. 108–113, 2005.

[133] Z. Turtayeva, F. Xu, J. Dillet, *et al.*, "Manufacturing catalyst-coated membranes by ultrasonic spray deposition for PEMFC: Identification of key parameters and their impact on PEMFC performance," *International Journal of Hydrogen Energy*, vol. 47, no. 36, pp. 16 165–16 178, 2022.

[134] S. Liu, S. Yuan, Y. Liang, *et al.*, "Engineering the catalyst layers towards enhanced local oxygen transport of low-pt proton exchange membrane fuel cells: Materials, designs, and methods," *International Journal of Hydrogen Energy*, vol. 48, no. 11, pp. 4389–4417, 2023.

[135] B. Millington, V. Whipple, and B. G. Pollet, "A novel method for preparing proton exchange membrane fuel cell electrodes by the ultrasonic-spray technique," *Journal of Power Sources*, vol. 196, no. 20, pp. 8500–8508, 2011.

[136] S. A. Mauger, J. R. Pfeilsticker, M. Wang, *et al.*, "Fabrication of high-performance gas-diffusion-electrode based membrane-electrode assemblies," *Journal of Power Sources*, vol. 450, p. 227 581, 2020.

[137] S. Martin, J. Jensen, Q. Li, P. Garcia-Ybarra, and J. Castillo, "Feasibility of ultra-low pt loading electrodes for high temperature proton exchange membrane fuel cells based in phosphoric acid-doped membrane," *International Journal of Hydrogen Energy*, vol. 44, no. 52, pp. 28 273–28 282, 2019.

[138] C. Yang, N. Han, Y. Wang, *et al.*, "A novel approach to fabricate membrane electrode assembly by directly coating the nafion ionomer on catalyst layers for proton-exchange membrane fuel cells," *ACS Sustainable Chemistry &amp Engineering*, vol. 8, no. 26, pp. 9803–9812, 2020.

[139] A. BAYRAKCEKEN, S. ERKAN, L. TURKER, and I. EROGLU, "Effects of membrane electrode assembly components on proton exchange membrane fuel cell performance," *International Journal of Hydrogen Energy*, vol. 33, no. 1, pp. 165–170, 2008.

[140] A. Therdthianwong, P. Manomayidthikarn, and S. Therdthianwong, "Investigation of membrane electrode assembly (MEA) hot-pressing parameters for proton exchange membrane fuel cell," *Energy*, vol. 32, no. 12, pp. 2401–2411, 2007.

[141] Q. Tang, B. Li, D. Yang, P. Ming, C. Zhang, and Y. Wang, "Review of hydrogen crossover through the polymer electrolyte membrane," *International Journal of Hydrogen Energy*, vol. 46, no. 42, pp. 22 040–22 061, 2021.

[142] S. S. Kocha, J. D. Yang, and J. S. Yi, "Characterization of gas crossover and its implications in PEM fuel cells," *AIChE Journal*, vol. 52, no. 5, pp. 1916–1925, 2006.

[143] K. BROKA and P. EKDUNGE, *Journal of Applied Electrochemistry*, vol. 27, no. 2, pp. 117–123, 1997.

[144] S. Prass, J. St-Pierre, M. Klingele, K. A. Friedrich, and N. Zamel, "Hydrogen oxidation artifact during platinum oxide reduction in cyclic voltammetry analysis of low-loaded PEMFC electrodes," *Electrocatalysis*, vol. 12, no. 1, pp. 45–55, 2020.

[145] "EIS equivalent circuits," in *Electrochemical Impedance Spectroscopy in PEM Fuel Cells*, Springer London, 2010, pp. 139–192.

[146] A. COLLIER, H. WANG, X. ZIYUAN, J. ZHANG, and D. WILKINSON, "Degradation of polymer electrolyte membranes," *International Journal of Hydrogen Energy*, vol. 31, no. 13, pp. 1838–1854, 2006.

[147] F. A. de Bruijn, V. A. T. Dam, and G. J. M. Janssen, "Review: Durability and degradation issues of PEM fuel cell components," *Fuel Cells*, vol. 8, no. 1, pp. 3–22, 2008.

[148] R. Borup, J. Meyers, B. Pivovar, *et al.*, "Scientific aspects of polymer electrolyte fuel cell durability and degradation," *Chemical reviews*, vol. 107, no. 10, pp. 3904–3951, 2007.

[149] E. Guilminot, A. Corcella, F. Charlot, F. Maillard, and M. Chatenet, "Detection of pt[sup z] ions and pt nanoparticles inside the membrane of a used PEMFC," *Journal of The Electrochemical Society*, vol. 154, no. 1, B96, 2007.

[150] J. P. Braaten, X. Xu, Y. Cai, A. Kongkanand, and S. Litster, "Contaminant cation effect on oxygen transport through the ionomers of polymer electrolyte membrane fuel cells," *Journal of The Electrochemical Society*, vol. 166, no. 16, F1337–F1343, 2019.

[151] K. Kodama, T. Nagai, A. Kuwaki, R. Jinnouchi, and Y. Morimoto, "Challenges in applying highly active pt-based nanostructured catalysts for oxygen reduction reactions to fuel cell vehicles," *Nature Nanotechnology*, vol. 16, no. 2, pp. 140–147, 2021.

[152] Z. Wang, E. Tada, and A. Nishikata, "In-situ monitoring of platinum dissolution under potential cycling by a channel flow double electrode," *Journal of The Electrochemical Society*, vol. 161, no. 4, F380–F385, 2014.

[153] Y. Zhang, S. Chen, Y. Wang, *et al.*, "Study of the degradation mechanisms of carbon-supported platinum fuel cells catalyst via different accelerated stress test," *Journal of Power Sources*, vol. 273, pp. 62–69, 2015.

[154] S. G. Rinaldo, J. Stumper, and M. Eikerling, "Physical theory of platinum nanoparticle dissolution in polymer electrolyte fuel cells," *The Journal of Physical Chemistry C*, vol. 114, no. 13, pp. 5773–5785, 2010.

[155] W. Bi and T. Fuller, "Temperature effects on PEM fuel cells pt/c catalyst degradation," *ECS Transactions*, vol. 11, no. 1, pp. 1235–1246, 2007.

[156] R. Sgarbi, W. A. Idir, Q. Labarde, *et al.*, "Does the platinum-loading in proton-exchange membrane fuel cell cathodes influence the durability of the membrane-electrode assembly?" *Industrial Chemistry &amp Materials*, vol. 1, no. 4, pp. 501–515, 2023.

[157] K. Yu, D. J. Groom, X. Wang, *et al.*, "Degradation mechanisms of platinum nanoparticle catalysts in proton exchange membrane fuel cells: The role of particle size," *Chemistry of Materials*, vol. 26, no. 19, pp. 5540–5548, 2014.

[158] J. Zhao, Z. Tu, and S. H. Chan, "Carbon corrosion mechanism and mitigation strategies in a proton exchange membrane fuel cell (PEMFC): A review," *Journal of Power Sources*, vol. 488, p. 229 434, 2021.

[159] J.-H. Park, S.-D. Yim, T. Kim, *et al.*, "Understanding the mechanism of membrane electrode assembly degradation by carbon corrosion by analyzing the microstructural changes in the cathode catalyst layers and polarization losses in proton exchange membrane fuel cell," *Electrochimica Acta*, vol. 83, pp. 294–304, 2012.

[160] P. Ren, P. Pei, Y. Li, Z. Wu, D. Chen, and S. Huang, "Degradation mechanisms of proton exchange membrane fuel cell under typical automotive operating conditions," *Progress in Energy and Combustion Science*, vol. 80, p. 100 859, 2020.

[161] N. Linse, L. Gubler, G. G. Scherer, and A. Wokaun, "The effect of platinum on carbon corrosion behavior in polymer electrolyte fuel cells," *Electrochimica Acta*, vol. 56, no. 22, pp. 7541–7549, 2011.

[162] M. Pawlyta, S. Smykała, B. Liszka, *et al.*, "Influence of carbon support structure on cathode catalysts durability," *Applied Surface Science*, vol. 611, p. 155 637, 2023.

[163] W. Chen, B. Chen, K. Meng, H. Zhou, and Z. Tu, "Experimental study on dynamic response characteristics and performance degradation mechanism of hydrogen-oxygen PEMFC during loading," *International Journal of Hydrogen Energy*, vol. 48, no. 12, pp. 4800–4811, 2023.

[164] A. P. Young, J. Stumper, and E. Gyenge, "Characterizing the structural degradation in a PEMFC cathode catalyst layer: Carbon corrosion," *Journal of The Electrochemical Society*, vol. 156, no. 8, B913, 2009.

[165] B. Xiao, J. Zhao, L. Fan, Y. Liu, S. H. Chan, and Z. Tu, "Effects of moisture dehumidification on the performance and degradation of a proton exchange membrane fuel cell," *Energy*, vol. 245, p. 123 298, 2022.